

University of Nottingham
UK | CHINA | MALAYSIA

Design and Modelling Techniques for Performance Improvement of Synchronous Reluctance Machines

Oğuz Korman

Thesis submitted to the University of Nottingham
for the degree of Doctor of Philosophy

Department of Electrical and Electronic Engineering
Faculty of Engineering

September 2023

Abstract

The design of electric machines constitutes a complex optimization problem subject to target application and performance requirements. State-of-the-art design routines generally start with adaption of a certain geometry followed by an optimization process. An optimization process has its own challenges as it shows sensitive behaviour to objectives and constraints. When the optimization problem is an electric machine design, challenge only becomes more sophisticated. Existence of non-linearity due to magnetic materials and performance requirements which more than often contradicts, requires proper handling of the optimization process. This is particularly a problem for more complex machine topologies such as synchronous reluctance (SynRel) and internal permanent magnet (IPM) machines.

Besides reaching the optimum geometry, optimality of the selected geometry itself is another uncertainty. This is particularly puzzling especially at the early design stages when a lot of machine parameters are still not selected (such as number of slots and poles). Assessment of the machine parameters along with the geometry then becomes a tangled and time consuming process if a fast analysis tool is missing.

This thesis puts these concerns to its center and orbits around them separately. In the beginning, focus is spent on geometric parametrization of the SynRel machine. Once this is achieved, the effecs of the objectives selection during an optimization are investigated. This is later followed by an improved geometric parametrization with the aim of increasing the degrees of freedom. Optimizations are performed to compare existing and newly proposed geometry to contribute towards a more optimal geometry. One of the designs achieved with the optimizations is manufactured and experimentally validated.

After that, geometric parametrization is put aside and topology optimization (TO) is used to widen SynRel design space. Since the only parameters with the TO are optimization settings themselves, their effect on the results are deeply examined. Viability of using TO as a design refinement tool is also analyzed by selecting an already optimized design space.

In the final part, computational burden of the design processes are addressed through building a highly accurate and fast magnetic equivalent circuit

(MEC). The description and principles of this fast analysis technique is presented and it is used to analyze three different machines, namely a SynRel machine, a surface permanent magnet (SPM) machine and a permanent magnet assisted synchronous reluctance machine (PMaSynRel). Through comparisons against finite element analysis (FEA), accuracy of the MEC is proved. As a last remark, an off-the-shelf SynRel machine is tested to obtain its electromagnetic properties and they are used to asses performance of the MEC.

Acknowledgements

I would like to thank to my supervisors Michele Degano, Mauro di Nardo and Christopher Gerada for their efforts during this four years of PhD. I specifically want to express my gratitute for Michele Degano and Mauro di Nardo, whom endlessly supported, motivated and helped me starting from the first day of this journey.

I am quite happy to have the support of my beloved family, namely my mother Ayse Sule Edes, my brother Yavuz Korman and my father Fetin Korman, through this PhD and life. I therefore thank them for being there for me and motivating me whenever the times are tough. I would also like to thank to my late grandfather Mustafa Yuksel Edes for his encouragement and support not only during my PhD but also all my academic life.

I would like thank all of my friends in the PEMC Research Group for being there for me whenever I needed. Here, a special thanks goes to my friends Yusuf Akçay and Mustafa Kaya whose presence made me feel strong and made my life easier. Their support was invaluable.

I would like to thank Jacopo Riccio for his helps and efforts during the experimental verification phases. To Amedeo Vannini for being a perfect conference companion and our time well spent on many discussions. To Valon Blakaj for our deep technical discussions and his valuable suggestions. I would also like to thank to my friend and supervisor Mukhammed Murataliyev for his supports and the time we spent discussing about electrical machines as well as fascinating new ideas.

Finally, I would like to express my sincere gratitute to Merve Aktas as she constantly supported and encouraged me during this time. I feel more than lucky to have her by my side during these years.

List of Publications

1. O. Korman, M. d. Nardo, M. Degano and C. Gerada, "Influence of Optimisation Target Functions on Synchronous Reluctance Machines Design," IECON 2020 The 46th Annual Conference of the IEEE Industrial Electronics Society, Singapore, 2020, pp. 1015-1020, doi: 10.1109/IECON43393.2020.9254529. [Chapter 2]

2. O. Korman, M. D. Nardo, M. Degano and C. Gerada, "A Novel Flux Barrier Parametrization for Synchronous Reluctance Machines," in IEEE Transactions on Energy Conversion, vol. 37, no. 1, pp. 675-684, March 2022, doi: 10.1109/TEC.2021.3099628. [Chapter 2]

3. O. Korman, M. Di Nardo, M. Degano, and C. Gerada, "On the Use of Topology Optimization for Synchronous Reluctance Machines Design," Energies, vol. 15, no. 10, p. 3719, May 2022, doi: 10.3390/en15103719. [Chapter 3]

4. O. Korman, M. Di Nardo, M. Murataliyev, M. Degano and C. Gerada, "Magnetic Equivalent Circuit Modelling of Synchronous Machines," 2023 IEEE International Electric Machines & Drives Conference (IEMDC), San Francisco, CA, USA, 2023, pp. 1-7, doi: 10.1109/IEMDC55163.2023.10238968. [Chapter 4]

5. O. Korman, M. Di Nardo, M. Degano, C. Gerada, G. Gallicchio and F. Cupertino, "On the Pole Pair Selection of Synchronous Reluctance Machines for Traction Applications," 2022 International Conference on Electrical Machines (ICEM), Valencia, Spain, 2022, pp. 2114-2120, doi:10.1109/ ICEM51905.2022.9910687.

List of Abbreviations

MEC	Magnetic Equivalent Circuit
SPM	Surface Permanent Magnet
FEA	Finite Element Analysis
MMF	Magnetomotive Force
PM	Permanent Magnet
3D	Three Dimensional
PMLSM	Permanent Magnet Linear Synchronous Motor
2D	Two Dimensional
SRM	Switched Reluctance Motor
IM	Induction Machine
GA	Genetic Algorithm
IPM	Internal Permanent Magnet
CE	Cell Element
SynRel	Synchronous Reluctance
PMaSynRel	Permanent Magnet Assisted Synchronous Reluctance
MOGA	Multi Objective Genetic Algorithm
MTPA	Maximum Torque per Ampere
MTPV	Maximum Torque per Voltage
PMSM	Permanent Magnet Synchronous Machine
SIMP	Solid Isotrophic Material with Penalisation
DM	Density Method
SLP	Sequential Linear Programming

Contents

Abstract i

Acknowledgements iii

List of Publications iv

List of Abbreviations v

1 Introduction 1

1.1 Motivation and Objectives 1

1.2 Organization of the Thesis 2

2 Synchronous Reluctance Machines Design and Parametrization of Machine Geometry 4

2.1 Introduction 4

2.2 Barrier's Shape Parametrization Based on Natural Flux Lines . . . 8

2.2.1 Formation of Fluid Shaped Barriers 10

2.2.2 Optimization Considering Different Objective Functions . . 13

2.2.2.1 Optimization Routine 15

2.2.2.2 Comparison of Optimization Results 16

2.2.2.2.1 Optimization-1 (O1) 16

2.2.2.2.2 Optimization-2 (O2) 17

2.2.2.2.3 Optimization-3 (O3) 19

2.2.2.2.4 Further Discussion on Optimization Results 20

2.3 Novel Barrier Shape with Increased Degrees of Freedom 22

2.3.1 Parametrization of the Novel Barrier Profile 23

2.3.1.1 Optimization of SynRel Rotor 26

2.3.1.1.1 Optimization Results 29
2.3.1.1.2 Analysis of the Optimal Machines . . . 30
2.3.1.1.3 Mechanical Considerations 32
2.3.2 Parametrization for PM Assistance 34
2.3.2.1 Optimization of the PMaSynRel Rotor 36
2.3.2.1.1 Optimization Results 38
2.4 Experimental Assesment 40
2.4.1 Skewing of the Rotor 40
2.4.2 Prototype Machine 41
2.4.3 Test Procedure and Setup 41
2.4.4 Results 43
2.5 Conclusion 44
2.5.1 Possible Future Work and Improvements 45

3 Topology Optimization for Synchronous Reluctance Machine Design 46

3.1 Introduction 46
3.2 Methodology 53
3.2.1 Benchmark Machine and Analysis Settings 55
3.3 Optimizations Starting from an Empty Design Space 55
3.3.1 Effect of Discretization 56
3.3.2 Effect of Initial Density 59
3.3.3 Effect of Penalization Coefficient 61
3.3.4 Effect of Torque Ripple Minimization 63
3.4 Optimization Starting from a Non-Empty Design Space 65
3.5 Conclusion 69
3.5.1 Possible Future Work and Improvements 70

4 Magnetic Equivalent Circuit Modelling 71

4.1 Introduction 71
4.2 Description of the MEC 78
4.2.1 Boundary Conditions 80

4.2.2 Discretization and Definition of Machine Geometry 82
4.2.3 Handling the Rotation 84
4.2.4 Calculation of the Reluctance Values 85
4.2.5 MMF Definitions 86
4.2.5.1 MMF due to Windings 87
4.2.5.2 MMF due to PMs 88
4.3 Solution Technique 90
4.3.1 Building the Loop Reluctance Matrix R_L 90
4.3.1.1 Applying Odd Periodic Boundary Condition . . . 92
4.3.1.2 Writing R_L in Terms of Linear and Non-linear Reluctances 93
4.3.2 Non-Linear Iteration Using Newton-Raphson Method . . . 94
4.3.3 Calculation of Electromagetic Quantities 97
4.3.4 Overall Process of the Solution 99
4.3.5 Discussion on MEC Performance 100
4.4 Analysis Using the MEC 101
4.4.1 Single Point Analysis 101
4.4.2 Analysis in the DQ Current Plane 104
4.4.3 Sensitivity Analysis with Respect to CEs 107
4.5 Experimental Verification 109
4.5.1 Test Procedure 110
4.5.2 Test Setup 114
4.5.3 Results 115
4.5.3.1 Comparison Between FEA and MEC 115
4.5.3.2 Comparison Between Test and Analysis Results . 118
4.6 Conclusion 120
4.6.1 Possible Future Work and Improvements 121
5 Conclusion **123**
5.1 Conclusive Summary 123
5.2 Main Contributions 125

List of Tables

2.1 Dimensions of the SynRel machine to be optimized. 14

2.2 Optimization variables and objective functions. 14

2.3 Sample designs and their performance from optimization results. . . 21

2.4 Optimization variables and objective functions. 28

2.5 Optimization variables and objective functions. 37

3.1 Optimization results with torque ripple objective. 65

3.2 Optimization results starting from an already optimized design space. 67

4.1 Dimensions of the SPM, SynRel and PMaSynRel machines. 102

4.2 Discretization properties of machines. 103

4.3 Single point analysis comparison of FEM and MEC 106

4.4 Specifications of the SynRel machine to be tested. 111

4.5 Discretization properties of the SynRel machine under test. 116

List of Figures

2.1 Proposed reluctance rotor as presented in [1] 5

2.2 Description of the fluid barrier concept. 10

2.3 Description of the fluid barrier shape. 11

2.4 Optimization flowchart. 16

2.5 Results of O1 with respect to k_t, $a(1)$, $a(2)$ and $a(3)$. 17

2.6 Results of O2 with respect to k_t, iron Losses, $a(1)$, $a(2)$ and $a(3)$. . 18

2.7 Results of O3 with respect to k_t, iron Losses, $a(1)$, $a(2)$ and $a(3)$. . 19

2.8 Description of spline parametrization. 24

2.9 Spline barrier profiles formed with different number of control points per barrier: a) m=6, b) m=10, c) m=20 and d) m=30. 27

2.10 Pareto fronts of the optimizations 29

2.11 Selected designs on the Pareto front 30

2.12 Selected designs on the Pareto front 31

2.13 Magnetic field distributions of selected classical and spline machines. 33

2.14 Mechanical analysis results: Von Mises stress distribution. 33

2.15 Modification of classical parametrization for PM addition. 35

2.16 PMaSynRel rotors generated using splines and randomly valued parameters. 37

2.17 Optimization results of the PMaSynRel with classical and spline parametrization: a) Pareto front, b) selected design. 38

2.18 Comparison of machine characteristics with and without PMs 39

2.19 Torque and torque ripple with respect to increasing skew angle. . . . 41

2.20 Rotor of the prototype motor. 42

2.21 Bench setup for the prototype machine. 42

2.22 Test and analysis results: a) torque contours and b) torque versus current phase angle. 43

3.1 Description of design spaces usuing On/Off method and DM. 48

3.2 SynRel rotor structure obtained by TO process as presented in [44]. 49

3.3 Shape production based on Newton Gaussian Newtork as presented in [45]. 50

3.4 Various interpolation schemes characterized by increasing values of the penalization coefficient for permeability mapping$n$. 52

3.5 Various interpolation schemes characterized by increasing values of the penalization coefficient for reluctivity mapping$n$. 54

3.6 Benchmark SynRel machine obtianed with parametric optimization. 55

3.7 Maximum and minimum mesh densities used for optimization; maximum length of: a) 0.25mm and b) 2mm. 56

3.8 Optimization results considering different mesh settings. 57

3.9 Material and flux density distributions for optimization results with increasing mesh intensity: a) 0.25mm mesh material distribution, b) 0.25mm mesh flux density distribution, c) 0.5mm mesh material distribution, d) 0.5mm mesh flux density distribution, e) 1mm mesh material distribution, f) 1mm mesh flux density distribution, g) 2mm mesh material distribution, h) 2mm mesh flux density distribution. 58

3.10 Optimization results considering different starting densities. 59

3.11 Material distributions for optimization results with increasing initial densities: a) p= 0.2, b) p=0.5, c) p=0.9 60

3.12 Results of optimizations with different penalization coefficients. . . 61

3.13 Material distributions for optimization results starting from p=0.9, with increasing n: a) n= 2, b) n=3, c) n=4, d) n=5, e)n=10, f)n=20. . 62

3.14 Results of optimizations with different penalization coefficients and initial density. 63
3.15 Material distributions for optimization results: a) n=2 p=0.2, b) n=2 p=0.5, c) n=4 p=0.5, d) $n = 4$ p=0.7, e) n=10 p=0.7 64
3.16 Results of torque ripple minimization for 1mm mesh model: a) n ==1, p=0.9, b) n=1, p=0.5, c) n=2, p=0.2, d) n=2, p=0.5 and 2mm mesh model: e) n=1, p=0.9. 66
3.17 Material distribution of optimization results starting from an already optimized geometry, low mesh: a) n=1, p=0.5 b) n=1, p=0.9, c) n=2, p=0.2 d) n=2, p=0.5; high mesh: e) n=1, p=0.9, f) n=2, p=0.5. 68

4.1 Magnetic to electric circuit anology. 72
4.2 MEC of an induction machine as presented in [60] - shaded reluctances indicate saturable elements. 73
4.3 3D MEC structure of a PMLSM as presented in [64]. 73
4.4 MEC used to model SPM motor as presented in [65]. 74
4.5 MEC used to model an IPM machine specifically focusing on local saturation as presented in [70]. 75
4.6 MEC model of an IPM machine as presented in [76]. 77
4.7 General structure of the MEC and different CEs. 79
4.8 General structure of the MEC and different CEs. 82
4.9 Simple example of geometry description. 83
4.10 Geometry description of a SynRel machine on a 28v36 MEC. 84
4.11 Simple example of rotation. 85
4.12 CE shape and reluctance dimensions. 86
4.13 Example of a winding MMF 88
4.14 Example of a winding MMF 89
4.15 Simple example of 3v3 MEC structure 92
4.16 Visualization of periodic boundaries: (a) even periodicity, (b) odd periodicity 93

4.17 MEC solution procedure 99
4.18 Geometries of analyzed machines: (a) SPM, (b) SynRel and (c) PMaSynRel 101
4.19 flux densities 104
4.20 Flux density distributions obtained with MEC and FEA for analyzed machines: (a) SPM, (b) SynRel and (c) PMaSynRel 105
4.21 Results of dq-current plane analysis for SynRel, PMaSynRel and SPM machines using FEM and MEC 107
4.22 Results of sensitivity analysis S_1 and S_2 109
4.23 Results of sensitivity analysis S_3 and S_4 110
4.24 Geometry of the SynRel machine to be tested. 111
4.25 Test setup used to measure characteristics of the SynRel motor: a) overal test setup, b) SynRel and prime mover, c) control platform and inverter. 115
4.26 Discretization of the SynRel machine to be tested. 116
4.27 Comparison of results obtained by means of FEA and MEC analysis: a) d-axis flux, b) q-axis flux, c) torque, d) torque ripple. 117
4.28 Comparison of test versus analysis results: a) d-axis flux, b) q-axis flux, c) torque. 118

Chapter 1

Introduction

In this introductory part, general information about the work done during several phases of the PhD is given. Motivation and objectives are identified and organization of the thesis is explained.

1.1 Motivation and Objectives

This thesis focus on general design and modelling improvements for electric machines with a specific focus on SynRel machines. As this kind of machine is dominantly determined by its rotor shape, throughout this work rotor design is investigated. This is done by starting from a state-of-the-art geometry parametrization to build flux barriers. With the developed template, a number of optimization studies are conducted to reveal the effect and good practices of objective functions.

Having a geometric template and trying to reach an optimal solution via optimizations then lead to the question: what if the selected geometry is not actually the optimal one? To approach this question there are mainly three ways. First one is to identify and apply a number of different geometries and compare them based on the performances. This is actually a good way to review a range of structures and identify their advantages and drawbacks. Second way is to create a guideline to increase geometric degrees of freedom thereby enlarging the design space. Lastly, the third approach is to use another design method, TO, which directly focus on the topology itself without the limitations of geometric shapes. In this thesis second and third approaches are used to investigate design possibilities.

Final focus of the thesis is to explore an alternative analysis technique.

Traditionally finite element method is the one primarily used for design processes for electromagnetic devices. It is well established, mature and accurate. However it can require high computation time if it is used in all designs stages. With the modern applications requiring specific performance at more than one operating point computational burden can be further increased. On the other hand, MECs can be fast and accurate but they were mostly employed for fixed structures with a lot of limitations. Can they be made more generic while not losing their computational advantage? The last part of this work aims to say ”yes” to this question.

1.2 Organization of the Thesis

Thesis is written in three main technical chapters each focusing on a different objective as mentioned above. Brief summary of these are as follows:

- Chapter 2: ”Synchronous Reluctance Machines Design and Parametrization of Machine Geometry”

  The first technical chapter starts with an overview focusing on evolution of SynRel machines. In the beginning, one of the commonly used flux barrier structures is selected and its geometric parametrization is accomplished. This is then followed by a number of multi-objective optimization studies to evaluate the effect of optimization settings on the rotor design of SynRel machines. Various key parameters effecting the optimization performance are investigated.

  In order to extend the limits of classical parametrization methods, a novel flux barrier structure is proposed to expand the limits of the previously used barrier structure. Two barrier profiles are compared through optimizations,focusing on their electromagnetic and mechanical performances. Introducing magnets to the new and existing barrier structure, PMaSynRel machine is studied. Two barrier structures are again assessed by conducting an optimization. Afterwards, one the designs is selected for manufacturing and experimental results are given.

- Chapter 3: ”Topology Optimization for Synchronous Reluctance Machine Design”

The second technical chapter investigates the SynRel design using TO. This is done through examining the optimization settings of the density method (DM) based TO. Effect of design space discretizaton, initial design space and material interpolation are first studied with the aim of increasing average torque. After that torque ripple minimization is added as an extra objective and results are evaluated with respect to previous optimization results. Lastly, an already optimized SynRel rotor is used as initial solution to explore if TO can be used as a design refinement tool.

- Chapter 4: ”Magnetic Equivalent Circuit Modelling”

  In the final technical chapter, a highly detailed, computationally efficient and accurate MEC is introduced which is capable of considering non-linearity and analyzing different machine topologies without changing the underlying formulations. Principles of the equivalent circuits are presented in detail showing how geometry description and excitations are defined. Later MEC is used to analyze a SynRel, SPM and a PMaSynRel machine in a wide operation range. These results are compared against FEA in terms of performance and computation time. Finally an off-the-shelf SynRel motor is tested to validate the MEC.

Chapter 2

Synchronous Reluctance Machines Design and Parametrization of Machine Geometry

This chapter focuses on SynRel machine design and optimization. After the introduction part, the barrier shape parametrization is described. After that, optimization with different objective functions are investigated and their effect on the final geometry is discussed. Finally a design study will be conducted using a novel barrier shape.

2.1 Introduction

SynRel machines date back to 1920s where one of the first examples of a specific reluctance rotor resembling today's rotors was presented in [1]. In this work, a segmented, barrier-like structure is realized in order to enhance reluctance torque of the classical salient-pole rotor.

Although conceptually it was possible to move forward with this kind of machine, the lack of an electric drive to operate the machine limited its development until 1990s. In one of the works presented between these years, some general conditions are derived for building anisotropic rotors using permeance ratio between direct (d) and quadrature (q) axes [2]. Slitted rotor structure and its guidelines are also discussed. After that, an interesting attempt has been made towards better utilizing the rotor using specifically shaped axial laminations [3]. In such configura-

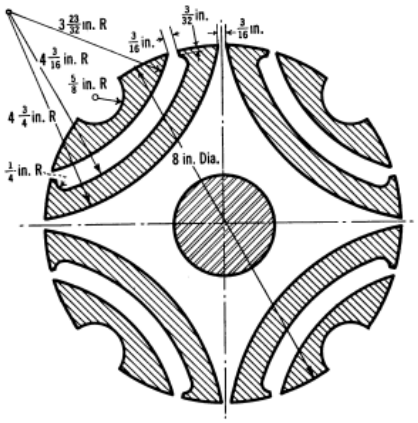


Figure 2.1: Proposed reluctance rotor as presented in [1]

tion, increasing the permeance ratio between d and q axis is easier compared to the traditional transversally laminated rotor as the iron segments are isolated magnetically. Another study [4] investigates the specific calculation of d and q-axis fluxes and inductances for a SynRel having a cut-off structure and a single barrier in the rotor.

After 1990, SynRel machines are continued to be investigated more around the design aspect. One of the initial works [5] extensively designs and compares SynRel machines with different number of flux barriers. It is shown that the single barrier SynRel machine suffers from poor saliency ratio and as a consequence low power factor, low torque and low field-weakening range. With the multi-barrier design study it is revealed that increasing the number of barriers after a certain number (in this case was 10) provides only a small increment in the performance. It is also discussed that it is possible to operate on a higher power factor by not operating at maximum torque per ampere (MTPA) condition if the torque degradation is overlooked.

A general design guideline for the design of SynRel motors is provided in [6]. For a segmented barrier structure, rotor design is discussed considering the thickness of iron and air segments. As a final remark, tangential mechanical ribs are considered for structural integrity and decrease in torque due to the existense of tangential ribs is calculated. Similarly, design considerations to improve torque and power factor are investigated in [7] based on the insulation ratio (= ratio of inductances $\frac{L_d}{L_q}$).

A chronic operational issue, the torque ripple, is deeply examined in [8]. The causes of torque ripple is given by the relation between stator and rotor gener-

ated harmonics. It is shown that the interaction of lower order harmonics originating from stator and rotor can actually be prevented by selecting an appropriate number of rotor segments and stator slots for a certain pole number. Moreover, thickness of barrier segments are calculated based on the d and q-axis magnetomotive forces (MMFs) which basically provides how flux barriers are shaped and positioned at the rotor surface. This is particularly important from design point of view as it explains the effect of rotor geometry to the torque and torque ripple. It is important to note that design equations mostly rely on the linearity of the magnetic circuit. Although they create a very strong basis for the design, local saturation effects and cross-coupling effects are not taken into account.

Considering the complexity of the design problem associated with SynRel motors and although it is possible to obtain somewhat good performing designs, clearly there is a need to conduct a wide-range analysis study especially using a high fidelity model such as finite element method (FEM). In the literature, one of the first reported works considering a specific algorithm to iteratively analyse and obtain a SynRel motor is reported in [9]. Powell's method and Quasi-Newton algorithms are used to optimize SynRel motors where a number of parameters define geometry of the stator and rotor such as stator tooth and yoke thickness as well as diameter, rotor barrier thicknesses and also current phase angle.

By the 2000s, the emerging permanent magnet (PM) technology found itself a considerable place in SynRel machines. For example in [10], permanent magnet assisted synchronous reluctance (PMaSynRel) motor is investigated by means of FEM. PMaSynRel is formed by introducing PMs of low remanent flux density (ferride PMS) to rotor flux barriers. Inductances of d and q-axis are evaluated as well discussing the effect of rotor ribs saturation. Final results suggest that torque density and power factor can be increased compared to PM free SynRel machine.

In an another study [11], PMaSynRel structure with different PM configurations and PM volume are investigated. It is experimentally shown that high efficiency and power over a wide speed range (1 to 5) is achievable by proper utilization of PMs. In a different paper [12], both SynRel and PMaSynRel machines are looked into. Starting from a SynRel machine, effect of the barrier width and location (for a single barrier) are examined and their effect on torque and torque ripple are discussed. A rotor with 3 barriers are also investigated based on the insu-

lation ratio. Electromagnetic performance degradation due to radial and tangential ribs are analyzed by a simple sensitivity analysis.

Bianchi et al. [13] presented a hybrid rotor configuration where a pole pair is composed of two differently shaped barrier structures as known as ”Machaon” configuration. The aim of using such structure is to purposely eliminate harmonics arising from different flux barriers. Authors first analytically describe the torque generation based on flux barriers then merge two structures to accomplish this.

Focusing on the SynRel machine design in [14], it is shown that multi-barrier rotor design of a SynRel machine can be achieved by using only a limited number of parameters. As shown in the previous works, air and iron distributions in the rotor and the barriers' end-point on the rotor surface plays a key role in the outcome performance. In this work, using some different number of flux barriers in the rotor, torque is directly associated with the insulation ratio and torque ripple is related to the end-point position. By introducing a cut-off structure with a parameter it is further possible to change barriers' end-point position therefore tuning torque ripple. On top of that, a new barrier shape (hereafter will be referred as ”fluid”) is proposed based on natural flux distribution in a solid rotor. This structure, by not disturbing the flow of flux lines as it would have normally flow, claimed to have higher performance than other barrier shapes.

Different barrier shapes and their parametrization by using increased number of parameters are studied in [15]. Effect of introducing more degrees of freedom to flux barrier rotor design for SynRel machine, for example end-point angle and thickness of each barrier, are investigated by means of optimization procedures. In a similar but extended work [16], circular flux barriers are used to conduct optimization with three stochastic algorithms, genetic algorithm, differential evolution and simulated annealing. Optimization results, quality of the Pareto front and time required for each algorithm are discussed. Additionally, the effect of optimization at one operating point is discussed and it is recommended to conduct optimization at higher currents then rated current. Another work focusing on optimized design [17], targets electric vehicle applications and considers different operation conditions inside the driving cycles. Robustness of the results with respect to objective functions are also considered on the Pareto designs and sensitivity of objectives are discussed.

Particular attention has been drawn to end-barrier shape and its effect on torque performances as well as mechanical robustness in [18]. Two different barrier shapes, round and sharp end barriers are optimized and investigated with further sensitivity analysis and it is concluded that sharp end barrier shape produces higher mechanical stress at the ribs part whereas when similar stress levels are considered round shaped end barriers produce higher average torque (5%).

In view of these previous works, it is obvious that design of SynRel and PMaSynRel machines constitutes a difficult design problem which often requires sophisticated approaches. Firstly, geometry of these type of machines, specifically rotor, is complex and there are a lot of geometric variables to account for. Secondly, the necessity of structural parts that need to be included in turn degrades the electromagnetic performance. Thirdly, design targets such as increasing the average torque and decreasing the torque ripple while maintaining a good efficiency are generally inversely related to each other; therefore even after an optimization there are some certain trade-offs that needs to be identified.

In the following sections, design of reluctance machines will be shown focusing mainly on the rotor design. Rotor designs with different parametrizations and different number of variables for the same parametrization will be undertaken. Effect of using different objective functions are also of interest as the convergence of any optimization is heavily dependent on the targets. In addition, a rotor barrier shape with increased degrees of freedom will be identified and PM assistance will be discussed.

2.2 Barrier's Shape Parametrization Based on Natural Flux Lines

As previously discussed, rotor design of electric machines utilizing reluctance torque plays a crucial role in the machine's performance. Average torque, torque ripple, iron losses, cross-coupling (also referred as cross-saturation) are some of the most important aspects primarily affected by the rotor design. Additionally, rotor structural integrity also has to be considered through rotor design especially in the high-speed applications. This puts forward the importance of rotor design which is mostly achieved through parametrization based on a specific barrier structure followed by a detailed optimization process.

Among the different barrier shapes, circular barriers [19], straight-segment barriers [20] [21] and fluid shaped barriers [14] comes forward. These are compared in terms of torque and torque ripple in [14] and [22] where it is revealed that fluid barriers perform slightly better. For this reason fluid barriers are adapted and used in this work.

Fluid barrier shape originated from the natural distribution of flux lines in a solid rotor. Idea is to use the naturally occurring flux lines to shape flux barriers so that flux lines in the iron segments are not distorted leading to unnatural flux paths.

The first step for parametrization is to find the flux line and the coordinates of the flux line. Each flux line can be find by using Equation (2.1). $C(r,\theta)$ corresponds to a flux line passing through a point (r,θ) in polar coordinates where r is the radius, θ is the angle and p is the number of pole pairs.

$$C(r,\theta) = \frac{sin(p\theta)[(\frac{r}{R_{shaft}})^{2p} - 1]}{(\frac{r}{R_{shaft}})^{p}} \tag{2.1}$$

Observing the Equation (2.1), it can be seen, there are infinite number of (r,θ) corresponding to a specific flux line $C(r,\theta)$. As a common practice, it is useful to first define C based on a point on the rotor surface to have the initial set of polar coordinates. If this angle is denoted as θ_1 and selected in the range $[\frac{360}{4p}\ \frac{360}{2p}]$, then since the flux lines are symmetrical due to middle line of a single pole, symmetrical angle can be written as $\theta_2 = \frac{360}{2p} - \theta_1$. After that, by creating a range of angles between $[\theta_1 ... \theta_2]$ and inserting them into Equation (2.2), r values corresponding to angles can be found with the C. Additionally, if tangential ribs are used, exact coordinates passing through the rib radius can be found by using Equation (2.3).

$$r(\theta) = R_{shaft} \cdot \sqrt[p]{\frac{C + \sqrt{C^2 + 4 \cdot sin^2(p\theta)}}{2 \cdot sin(p\theta)}} \tag{2.2}$$

$$\theta(r) = \frac{1}{p} \cdot sin^{-1}\left(\frac{C \cdot (\frac{r}{R_{shaft}})^{p}}{(\frac{r}{R_{shaft}})^{2p} - 1}\right) \tag{2.3}$$

Usage of equations to build the flux line and associated points are visualized in Figure 2.2. In the figure red line with circles show the flux line initially found by selecting $(r,\theta) = (R_{rotor}, 55^o)$ and calculating C with Equation (2.1). Then, θ_2 is calculated and coordinates of the flux line are found. Finally using Equa-

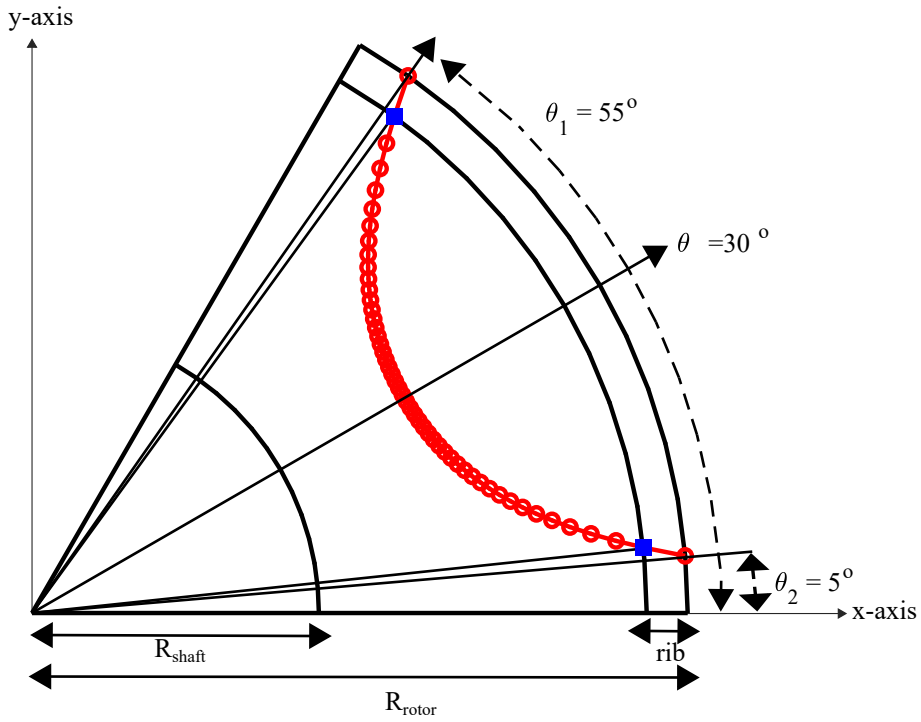


Figure 2.2: Description of the fluid barrier concept.

tion (2.3) exact coordinates of the flux line passing through the rib radius are calculated (shown with blue squares).

2.2.1 Formation of Fluid Shaped Barriers

In order to form the flux barriers, it is vital to use newly described equations. However, a systematic approach is required in order to describe each barriers end-point angle and thickness in a way that they do not overlap.

As an example, a 4 pole rotor with 3 barriers are considered as shown in Figure 2.3. Following the practical approach of defining barriers with the end-point angle, span of each barrier from start to end is denoted as a, where the end-points are shown with filled red circles in Figure 2.3. The span angles a initially act as a reference to find the flux lines (shown with dashed lines) passing through the end-points. In order to prevent overlap, it is better to select a based on some rules. To begin with, the reference angle for the first barrier (outermost barrier) can be selected in the range of $(0\ \frac{360}{2p})$. Apparently a selection near to the $\frac{360}{2p}$ strongly limits the other barriers hence it would be more convenient to select it somewhere towards the $\frac{360}{4p}$. Also, to make it more convenient a coefficient can be defined $k_{a_{(1)}}$ in the range of $(0\ 1)$ to represent $a(1)$ with $a(1) = \frac{360}{2p} \cdot k_{a_{(1)}}$. Once the value of $a(1)$

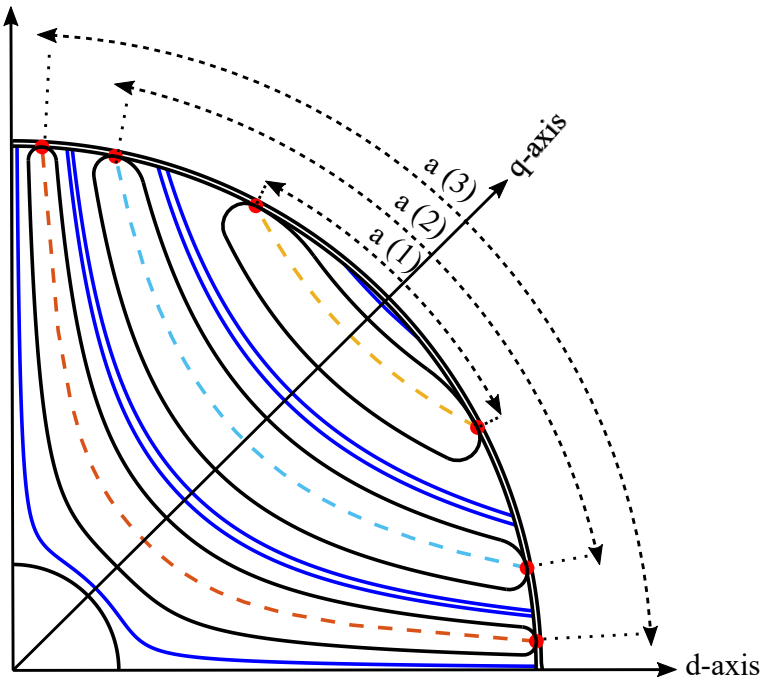


Figure 2.3: Description of the fluid barrier shape.

is found, the other barriers angles, when the total number of barriers are (>2) can be similarly defined using:

$$\text{for n= 2 to } n_l,\ a(n) = a(1) + \left(\frac{\pi}{p} - a(1)\right) \cdot \sum_{n=2}^{n_l} k_{a(n)} \tag{2.4}$$

In the Equation (2.4), n is the calculated barrier number and n_l is the total number of barriers. The limits of k_{a_n} for the barrier number 2 and higher than 2 is found by $(0\ \frac{1}{n_l - 1})$. Now, since the reference flux lines are calculated it is possible to move towards finding the barrier thicknesses.

Barrier thicknesses are depending on the distance between the reference flux lines and between reference flux lines to rotor and shaft radiuses. Consequently there is a maximum thickness available (mta) for each barrier in terms of available space on top and bottom side of the reference flux lines. These limits are shown with continuous blue lines for each barrier in the Figure 2.3.

$$\text{for n=2 to } n_l - 1,\ \ mta_{l-l}(n) = \frac{r_{mid}(n) - r_{mid}(n+1)}{2} \tag{2.5}$$

To calculate the available space between the reference lines Equation (2.5) can be used. In Equation (2.5) $r_{mid}(n)$ corresponds to n^{th} barrier's middle point which lies on the q-axis. This quantitiy can be calculated using Equation (2.2)

while setting $\theta = \frac{360^o}{4p}$. Similarly other thicknesses can be calculated considering shaft radius and rotor radius. Additional safety margins can be defined in terms of extra thicknesses. This is important because the distance between reference flux lines becomes minimum towards the end-points. After this procedure is followed, two thicknesses would be calculated for each barrier, one being on the upper side of the reference flux line and the other being on the lower side. These can be denoted as mta_u and mta_l.

$$t_l(n) = k_{tl}(n) \cdot mta_l(n) \tag{2.6}$$

$$t_u(n) = k_{tu}(n) \cdot mta_u(n) \tag{2.7}$$

$$t(n) = t_l(n) + t_u(n) \tag{2.8}$$

Barrier thicknesses can be controlled using some control coefficients to properly set a barrier's thickness. These are k_{tl} and k_{tu} in Equation (2.6). Total barrier thickness can be obtained by summing these thickness values. To create fewer variables defining barrier thickness, k_{tl} and k_{tu} can be made equal to each other and represented by k_t. Additionally, if the thickness coefficients of each barrier are made equal to each other, air to total rotor thickness ratio (insulation ratio) becomes equal to k_t. This case is applied to the barriers in Figure 2.3 where k_t=0.5 for each barrier and shown with continuous black lines.

These possibilities to express barrier thicknesses are an important choice as they determine the number of parameters describing the barriers, thus the degrees of freedom. Some of the options for increasing number of variables are as follows:

1. Total number of parameters is 2; k_a is equal for each barrier and is a variable. k_t is equal for each barrier and is a variable.

2. Total number of parameters is 2; k_a is equal for each barrier and is a constant. A shift angle on the rotor surface is introduced to change end-point of the barriers, k_t is equal for each barrier and is a variable.

3. Total number of parameter is 3; k_a is equal for each barrier and is a variable. A shift angle on the rotor surface is introduced to change end-point of the barriers. k_t is equal for each barrier and is a variable.

4. Total number of parameters is n_l +1; k_a is different for each barrier. k_t is equal for each variable and is a variable.

5. Total number of parameters is $2 \cdot n_l$; k_a and k_t are different for each variable. Each barrier is described by 2 parameters.

6. Total number of parameters is $2 \cdot n_l$; k_a and k_t are different for each variable. Additionally, for each barrier another end-point angle can be defined with in the limits of the barrier to provide more freedom for end-point.

From design point of view, although it seems that higher degrees of freedom for geometry description is favorable, it also complicates the design problem. Considering the convergence behaviour during the optimization, total number of analysis should be increased with respect to increasing number of optimization variables. Eventually there happens to be a trade-off between the increased degrees of freedom and time required to reach the convergence.

Regarding the barrier's end-shapes a circular form is adapted. When the end-point for a barrier is known, two arc segments can be calculated tangent to the end point and to the upper and lower flux lines forming a barrier. After that two arcs segments and the flux lines are all joined together to form the final barrier structure.

2.2.2 Optimization Considering Different Objective Functions

With the aim of investigating different objective functions, i.e torque, torque ripple and iron losses, 3 different optimizations are performed on a SynRel machine. Specifications of the SynRel machine are reported in Table 2.1 aimed for a light traction application. Stator of the machine incorporates single-layer distributed winding with a current density of $10\,A/mm^2$. It is desired to investigate the effect of different optimizations to the rotor design; so the whole stator is held constant throughout the optimization. Similarly, shaft and rotor radius is constant and only variables to be optimized are related to the rotor flux barrier design. Number of flux barriers are selected to be 3 for this case and they will be identified by using a total of 4 variables. Out of these 4 variables, 3 of them belong to the end-point angle of the barriers (a as in Figure 2.3) and the remaining one is k_t which determines the thickness for all barriers. As previously discussed, it can also be named

Table 2.1: Dimensions of the SynRel machine to be optimized.

General Dimensions		
Parameter	Value	Unit
Statour outer radius	123	mm
Rotor outer radius	80	mm
Air-gap length	0.7	mm
Shaft radius	35	mm
Stack length	120	mm
Rated current	82	A_{peak}
Current density	10	A_{RMS}/mm^2
Cooling flow Rate	10	L/min
Lamination material	M250-35A	
Rated Speed	2500	RPM
Maximum Speed	10000	RPM

as insulation ratio since all barriers are represented by the same variable. Ranges of the variables are given in Table 2.2. For the optimization studies, exact angular spans are preferred in order to better understand the effect of the positions to the objective functions.

Three different optimizations, namely O1, O2 and O3 are performed. Targets of these optimizations are given in Table 2.2. Starting from the simplest case O1, the objectives are the maximization of average torque and minimization of torque ripple. The latter is further supported by a constraint pushing towards designs having less than 10% torque ripple.

Table 2.2: Optimization variables and objective functions.

Flux Barrier's Variables		
Parameter	Value	Unit
$a(1)$	[14.81 37.60]	mech deg. ^{o}
$a(2)$	[40.00 50.70]	mech deg. ^{o}
$a(3)$	[52.30 58.90]	mech deg. ^{o}
k_t	[0.20 0.80]	-
O1		
$f_1 : max\ T_{avg}$ $f_2 : min\ T_{ripple}, < 10\ \%$		
O2		
$f_1 : max\ T_{avg}$ $f_2 : min\ T_{ripple}, < 10\ \%$ $f_2 : min\ P_{iron}$		
O3		
$f_1 : max\ T_{avg}, >$ **95 Nm** $f_2 : min\ T_{ripple}, < 10\ \%$ $f_2 : min\ P_{iron}$		

Second optimization O2 has the exact same targets and constraints of O1

but an additional objective function to minimize iron losses. The aim here is to distinguish between final geometries and results when core loss minimization is included. Lastly, O3 has all of the objectives of O2 but it has an additional constraint on average torque. The inclusion of constraint on average torque is mainly due to compensate the possibility of obtaining lower average torque designs caused by the minimization of iron losses.

2.2.2.1 Optimization Routine

Multi-objective genetic algorithm (MOGA) is selected for the optimization algorithm as it has a stochastic nature and performs well for multi-objective scenarios [23] [24]. A total of 4000 designs are considered for each optimization where the initial design of experiments are generated using Sobol sequences. There are other strategies to generate initial design of experiments such as using latin hypercube sampling or randomized generation however for this amount of variables Sobol sequences perform well to create a uniformly distributed designs inside variable limits.

For the FEM analysis, a 2D periodic model is used corresponding to one sixth of the whole motor model. Simulation time for each FEA corresponds to 1 slot pitch in order to capture torque ripple harmonics [19] with 10 equally spaced points. Current phase angle is used constant at 60^{o} to ensure an operation point fairly close to maximum torque per ampere (MTPA) condition. Even though it might not be the exact MTPA condition, being close to it will indirectly optimize the performance at the MTPA operation.

Optimization is performed in an automated fashion where the FEA software Ansys Maxwell is called using a MATLAB script. Using the script, Ansys Maxwell is controlled to perform pre-processing including drawing the geometry, setting up the boundary conditions and excitations with other analysis settings. After the pre-processing, analysis phase begins and results are imported back into MATLAB. Another software dedicated to perform optimizations with a range of algorithms, ModeFrontier, is used to control the optimization procedure coupled with the MATLAB script. Overall optimization flow is illustrated in Figure 2.4.

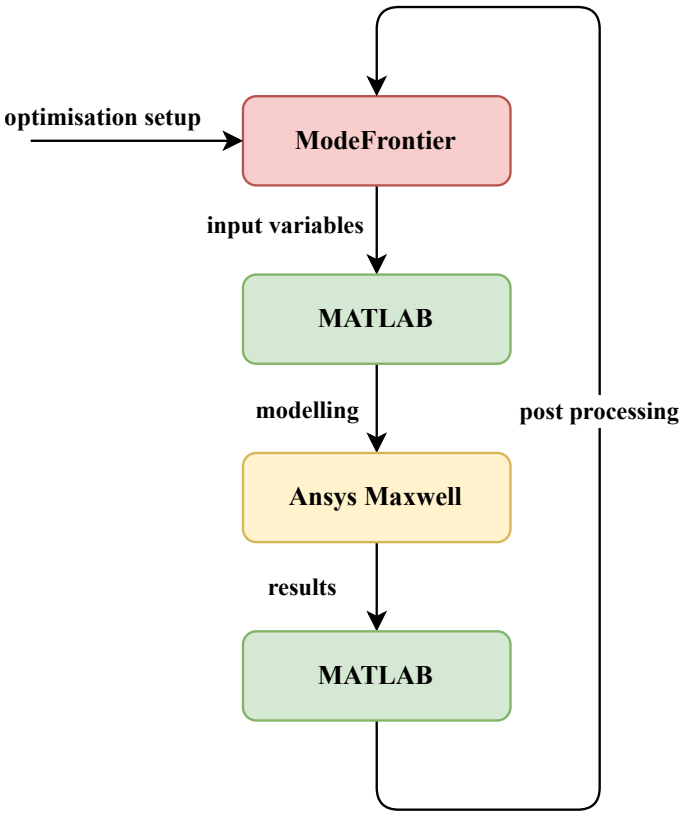


Figure 2.4: Optimization flowchart.

2.2.2.2 Comparison of Optimization Results

2.2.2.2.1 Optimization-1 (O1)

Results of O1 have been presented in Figure 2.5. Only the designs satisfying the torque ripple constraint are shown in terms of average torque and torque ripple (T_{Ripple}). Designs are shown with a color scale proportional to k_t, $a(1)$, $a(2)$ and $a(3)$. In the first plot there is a very uniform distribution of designs with respect to the insulation ratio. As expected, increasing values of the insulation ratio gives higher average torque values. In terms of barriers' span angles, it is noticeable that they are in very small ranges. In these small ranges, for different k_t values there is a combination of span angles which maximises the average torque. This is more evident when the designs are expressed in terms of $a(2)$ and $a(3)$, in which when the average torque and k_t increases span angles change. The average torque moves from 92.5 Nm to 96.5 Nm and general trends for $a(2)$ and $a(3)$ are to move towards its higher and lower limits, respectively. For the span angle of the first barrier, it is seen that in the higher torque area between 95 to 96.5Nm it is barely changing, inferring that first barrier's angle is less sensitive than the others. Moreover, it is seen

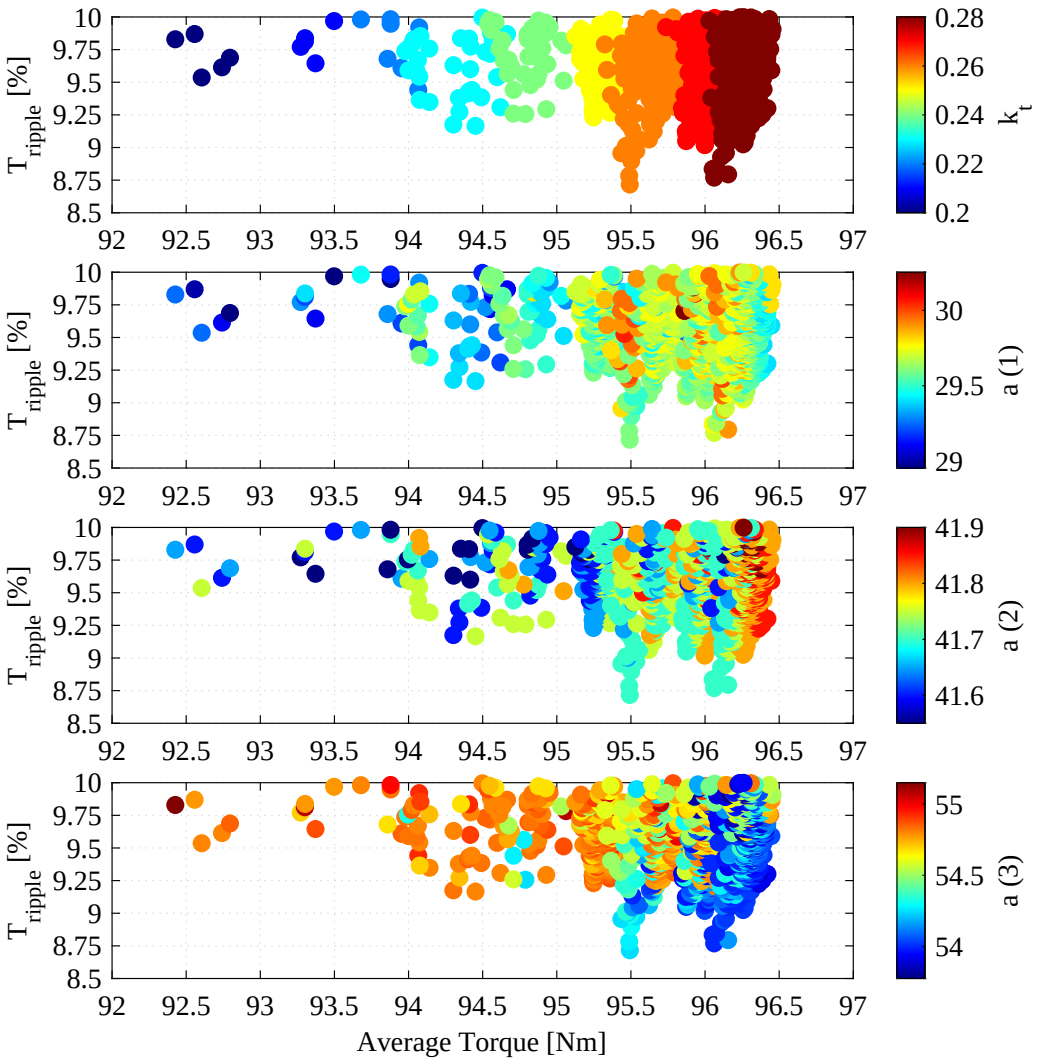


Figure 2.5: Results of O1 with respect to k_t, $a(1)$, $a(2)$ and $a(3)$.

that it is possible to obtain a certain level of torque ripple with different average torques and in this case $a(2)$ and $a(3)$ has slightly different values.

2.2.2.2.2 Optimization-2 (O2)

Results of O2 have been presented in Figure 2.6. Again, only the designs with torque ripple less than 10 % are shown. At a first glance, the most distinguishable difference between two optimizations O1 and O2 is the reduced average torque values from 92.5-96.5 Nm range to 90.5-92.5 Nm range. When compared to the results of O1 another interesting difference is the increased span angles of the barriers. This increased angle spans actually corresponds to fluid barriers being pushed towards the shaft. When the barriers move towards the shaft, the length of the flux paths increase due to the increased iron path lengths which in turn decreases the useful flux causing to a decrease in saturation. Lower saturation values lead to de-

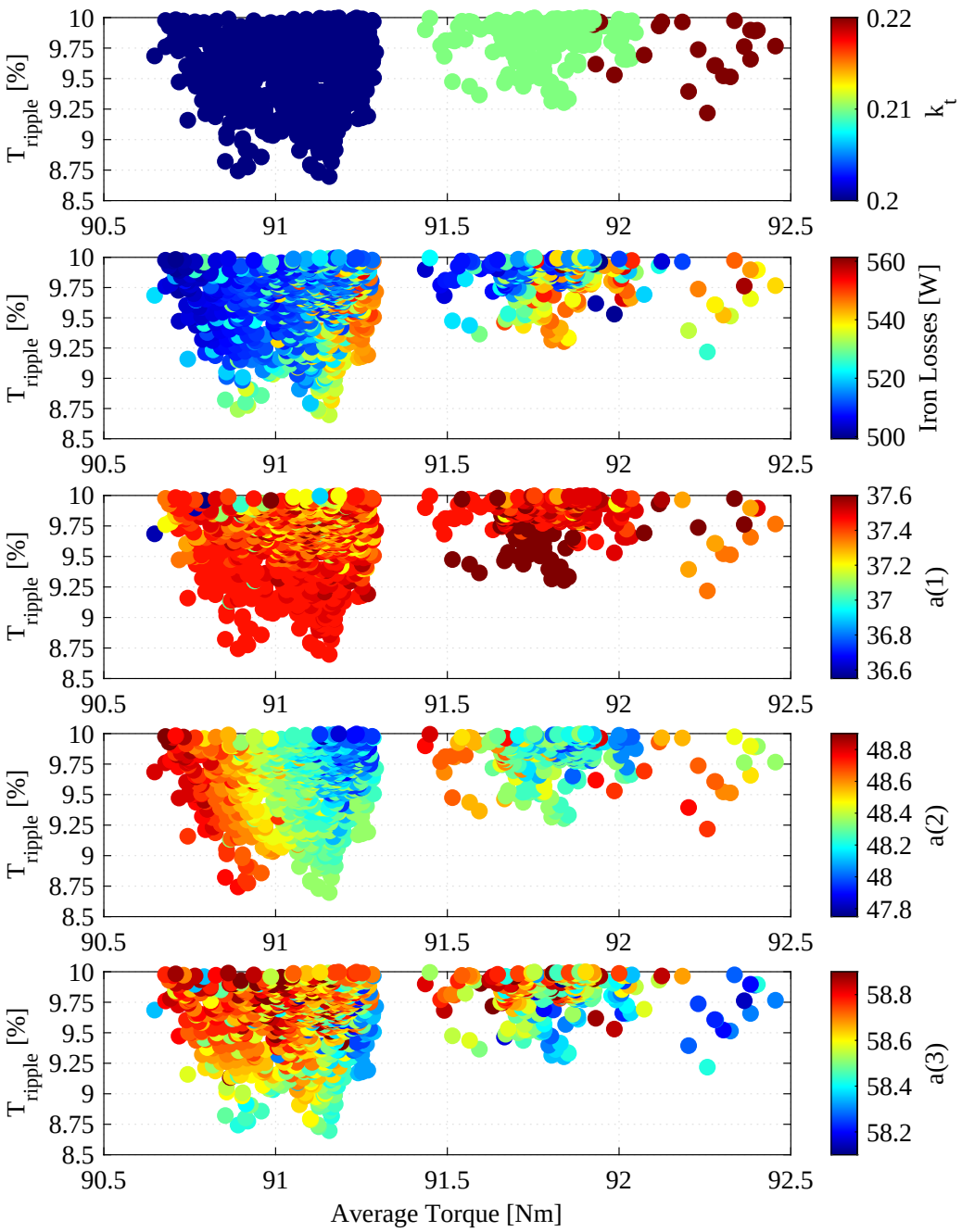


Figure 2.6: Results of O2 with respect to k_t, iron Losses, $a(1)$, $a(2)$ and $a(3)$.

creased iron loss but also degraded average torque. Additionally, k_t values decrease from O1 to O2, indicating that thickness of iron segments are increased which is another pathway towards lower saturation. In this case, again the end-point angle span of the outermost barrier seems to be almost insensitive as it mostly stays at 37.5^o for varying average torque and torque ripple. For a certain average torque, for example around 91Nm, it is clear that for decreasing torque ripple $a(2)$ stays more or less the same whereas $a(3)$ tends to decrease. This indicates that $a(3)$ is more dominantly affecting torque ripple than $a(2)$ and $a(1)$. Finally, considering the iron

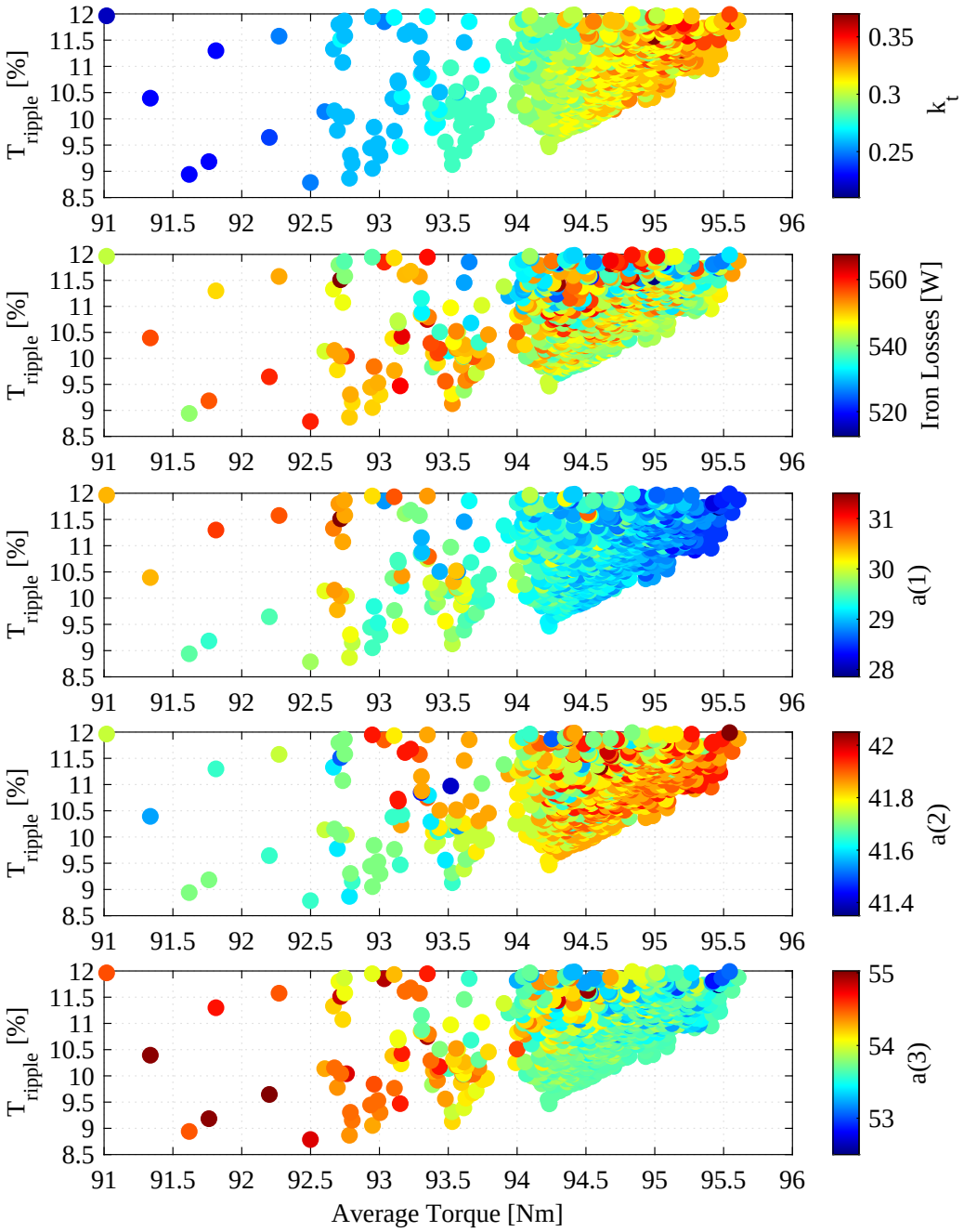


Figure 2.7: Results of O3 with respect to k_t, iron Losses, $a(1)$, $a(2)$ and $a(3)$.

losses, there is approximately 10 % difference between highest and lowest iron loss. Apart from the fact that iron losses tend to increase with increasing average torque (also k_t), interestingly for a certain average torque and decreasing torque ripple iron losses increase.

2.2.2.2.3 Optimization-3 (O3)

Based on the results obtained with O1 and O2 and considering the decreased torque levels in O2, a constraint is added on torque maximization objective

in O3 with the value of 95Nm. Results of O3 have been presented in Figure 2.7. In this case optimization actually couldn't be successful probably due to the conflicting objectives made it even more difficult with the newly added objective. As the number of designs having torque ripple lower than 10 % is low, although disobeying the torque ripple constraints designs are shown up to 12 %.

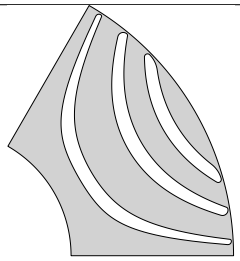
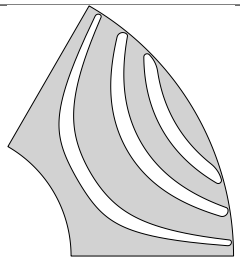
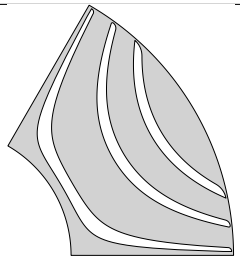
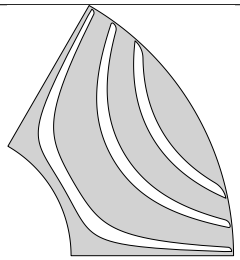
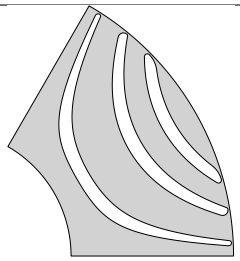
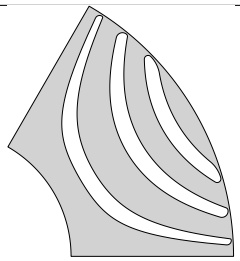
Obtained results show that torque values are increased compared to O2 and settled nearly to the values obtained with O1. To satisfy the torque conditions k_t values are also increased, becoming even higher than O1 results. Angle spans of the barriers are this time close to those obtained with O1. Individual effects of the angle span of the barriers are more straightforward than O1 and O2. With increasing average torque, decreasing, increasing and decreasing trends are obtained for $a(1)$, $a(2)$ and $a(3)$ respectively. Previously in O1 and O2 it has been observed that $a(1)$ had minor impact on average torque and torque ripple however it is not the case with O3, most probably due to different convergence behaviour with the newly added constraint pushing towards higher average torque values. Comparing the results of O1 and O3, it is seen that span angles are quite close to each other but at higher values of k_t. This suggests higher flux is flowing through the iron segments and probably another reason of first barrier's increased impact. Another important thing to notice with reference to Figure 2.7, although a general increase in the iron losses are seen compared to O2, it is possible to obtain low iron losses by fine-tuning the barrier angles.

2.2.2.2.4 Further Discussion on Optimization Results

In order to further examine the optimization results, two designs are selected for each optimization in the Pareto front solutions, one with the minimum torque ripple and other having the highest torque. For the O3, 95 Nm torque constraint is neglected during Pareto calculation. Summary of these designs are given in Table 2.3 in which rotor geometries, k_t, average torque, torque ripple and core losses are presented. Most noticeable difference, as previously mentioned, is the rotor designs obtained with O2. In this case barriers are thinner then and much more closer to the shaft. Another remark is the higher core losses with O1 designs due to lacking objective to reduce them.

In addition to those, although O3 underperformed to reach the objectives

Table 2.3: Sample designs and their performance from optimization results.

Optimization	Design	k_t	T_{avg} [Nm]	T_{rip} [%]	P_{iron} [W]
O1		0.26	92.87	8.98	552
O1		0.28	93.81	10.6	555
O2		0.2	91.15	8.69	534
O2		0.22	92.45	9.76	540
O3		0.25	92.49	8.78	559
O3		0.3	94.54	9.98	538

it is seen that the highest torque design belonging to O3 is the general best solution with the best compromise among the target functions. Obviously it is not fair to directly compare the optimizations because eventually the additional torque con-

straint imposed to O3 made possible due to O1, however it enlightens in such a way that including specific constraints to an optimization can lead to better results.

2.3 Novel Barrier Shape with Increased Degrees of Freedom

In the previous section fluid barrier shape is described and used for rotor design of a SynRel machine. This barrier shape, as defined by the Equations (2.1) (2.2) (2.3) is symmetrical with respect to both d and q-axis (see Figure 2.2 and Figure 2.3) and creating a more flexible shape, either directly in the sense of barrier shape or asymmetric structure requires modifications. This is not only the case for this type of barriers but also others, causing a limitation of shape.

Talking particularly about asymmetric barriers, unless the barriers for different poles are designed separately as in [13] and [25], a total change of defining equations would be required to define the barrier shape. Asymmetrical barriers are investigated in [26] by using polynomials to define barrier shape. In this study a large number of variables (29 to 37) are used to optimize flux barriers for a SynRel machine where the two sides of a flux barrier does not have identical end-point angles. By doing so authors managed to obtain low levels of torque ripple. Another study [27] also considers asymmetrical flux barriers with different end-point angles and widths at two ends of the rotor. It is again found that with this approach lower torque ripple values can be obtained compared to conventional fully symmetric flux barrier shapes.

Increasing degrees of freedom for barrier profile, straight, circular and hybrid barriers composed of both straight and circular barrier shapes are investigated in [28] for PMaSynRel machines. Based on the comparison between three different structures it is found that circular and hybrid barriers can perform slightly better than straight barriers. In particular, for PMaSynRel applications hybrid barriers might be preferable considering the ease of manufacturing for rectangular type magnets.

As summarized above, using more flexible shapes for flux barriers other than being limited to standardized parametrizations can prove useful. Two main philosophies can be adopted to enrich design possibilities of the SynRel flux barrier profiles. First approach is to increase degrees of freedom of a barrier shape which

can be parametrized to fully control the shape of the whole barrier. Other approach is to adopt a topology optimization where the flux barrier profile is not defined by a closed form equation. In this section, first approach will be followed, proposing an enriched parametrization providing additional degrees of freedom in order to investigate the effect of flux barrier's shape on the machine performance. The proposed parametrization makes use of cubic splines and defines barrier profile with a number of control points. Explicitly, using splines to connect control points is advantageous as the resulting shape is always unique, naturally smooth and with high degrees of freedom over the whole barrier. Both SynRel and PMaSynRel machines will be designed with the proposed barrier profile and trade-off between performances and geometric complexities are investigated from electromagnetic and mechanical point of view.

2.3.1 Parametrization of the Novel Barrier Profile

Proposed barrier shape is built on the fluid barrier shape. All the parametrization to form the fluid barriers as described in the previous section are valid and required. To form the new barrier shape (will be referred as spline parametrization and the fluid barrier shape will be referred as classical parametrization from now on), m number of control points are defined on each classical barrier shape. After the control point coordinates are known, they are connected together using natural cubic splines. Splines are selected due their smooth resultant curve and easy control within limits as they always pass through the control points.

The first step towards the spline parametrization is to have a complete classical parametrization. In the previous section, the classical parametrization has been described in detail and some choices regarding the number of parameters are discussed. Number of total variables for flux barriers will be composed of parameters describing the classical parametrization plus spline parametrization thus will lead to an increased number of variables. To limit this overgrow of number of variables, each barrier is first described by $2 \cdot n_l$ number of parameters, a and k_t for each barrier. The following steps describe the spline parametrization for a single barrier, which remains the same regardless the number of barriers:

1. In Figure 2.8 a) flux barrier profiles following the classical parametrization

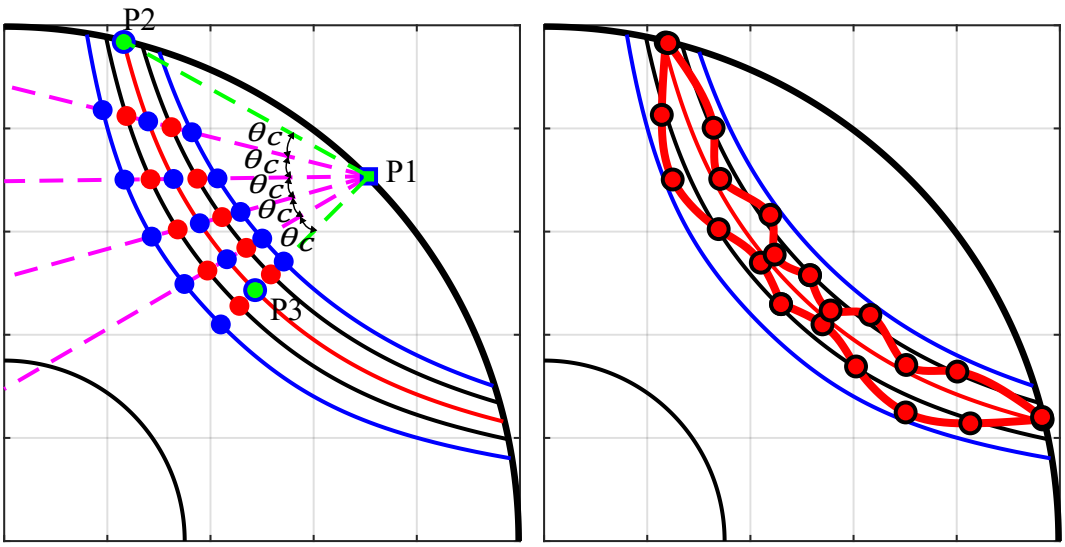


Figure 2.8: Description of spline parametrization.

steps are shown. With the defined value of k_t, barriers are shown with black lines and the blue lines show the maximum thickness limits of the barrier. Similarly P2 corresponds to the end-point calculated with a. Red line between the black lines shows the reference flux line.

2. The control points are shown with red dots in Figure 2.8 a). For each barrier two sets of control points exist, first set of points are located in the upper half region and the second set of points are located in the lower half region to form two splines making up a barrier.

3. In order to maintain convex nature of the flux barriers, the position of the control points is determined by the intersection of straight lines draw from P1 (middle point of the rotor point with an angle $\frac{360}{4p}$). These straight lines are shown with magenta colored dashed lines, and they aim to intersect reference flux line shown with red. This way to extreme points for intersection becomes end-point and P2 and the P3 in the middle.

4. For each drawn line, two control points are identified, on lower and upper black colored flux lines which are representing the barrier lines found with classical fluid parametrization. This creates $\frac{m}{2}$ pairs of control points that lay on the same straight line drawn from P1 where m is always an even number.

5. The control points shown with red dots have the flexibility to move between

adjacent blue dots that are on the blue lines (barrier limits obtained with classical parametrization).

6. ∠ P2P1P3 is known since it is related to the end-point angle,a, of the reference line and it can be written as 90^o - $\frac{a}{4}$. To form m control points, $\frac{m}{2}$ number of straight lines have to be defined starting from P1 making an angle of:

$$\theta_C = \frac{\angle P2P1P3}{m/2} = \frac{90^o - \frac{a}{4}}{m/2} \tag{2.9}$$

with each other. Straight lines can be expressed in the form of Equation (2.10) with the slope as in Equation (2.11) and its constants Equation (2.12). For the constant of the line c_i, $P1_{(x)}$ and $P1_{(y)}$ are x and y coordinates of the P1.

$$y_i(x) = m_i \cdot x + c_i \tag{2.10}$$

$$m_i = tan\big(\frac{180}{p} - \theta_C \cdot (i-1)\big) \tag{2.11}$$

$$c_i = P1_{(y)} - m_i \cdot P1_{(x)} \tag{2.12}$$

7. It was previously shown that to form a flux line Equations (2.1) (2.3) (2.2) have to be used. In order to find the intersection of a flux line and a straight line Equation (2.13) has to be solved. However there is no analytical solution to this equation, because a flux line defined by C exhibits trigonometric and exponential behaviour. To overcome this Equation (2.13) is solved using numerical methods in an iterative way.

$$C(x,y) = m_i \cdot x + c_i \tag{2.13}$$

8. Control points shown with red dots have the freedom to move between adjacent blue dots creating a straigh path on the lines characterized by Equation (2.10). The movement of the control points is parametrized based on the path they can move in between. Each control point can have a value in the range [-1 1] which decides their position on the line. Three important positions of a control point happens at the value of -1, 0 and 1. When the value is 0, it stays exactly on the black line meaning that it lays on the fluid

barrier. Otherwise when the values are -1 or 1, it becomes on the lower and upper blue dots respectively. In general, control points move towards lower and upper blue dots based on its positive or negative value.

9. After the position of control points are identified, next step is to generate piecewise cubic splines. For m control points there are $(\frac{m}{2}+1)$ points for upper and lower part of the flux barrier and the additional "+1" stands for the end-point. By using these points, two sets of piecewise cubic splines are realized for upper and lower parts of the flux barrier and they are joined together. Each set of splines have $\frac{m}{2}$ number of piecewise cubic polynomials.

An example showing the final barrier shape using a total of 10 control points are shown in Figure 2.8. Values of the control points are randomly selected for in the range [-1 1] for demonstration purposes.

With the intention of discussing the impact of different number of control points, various spline barrier profiles are generated with 6,10,20, and 30 control points per barrier. This is shown in Figure 2.9 with increasing number of control points. Barriers obtained with the classical parametrization are also shown for comparison. The values of the control points are again randomly generated and end-points of barriers are the same. It is important to notice as the number of control points increases as the complexity of the barrier profiles increase. Another point of consideration is that, increased number of control points does not have the same effect on each barrier's profile because simply high number of control points lead to somewhat disturbed shapes when the control points are located too close to each other. Therefore, it would be beneficial in terms of controlling the complexity of the barrier shapes to select the number of control points separately for each barrier. A different impact would be from the design point of view. Using increased number of variables would require an undesired effect of longer optimization time. For example although with any number of control points, spline barriers can converge to fluid barriers, the time it would take to do so would increase.

2.3.1.1 Optimization of SynRel Rotor

In this section two optimizations will be performed to design the rotor of a SynRel machine using two parametrizations, classical and spline parametrization.

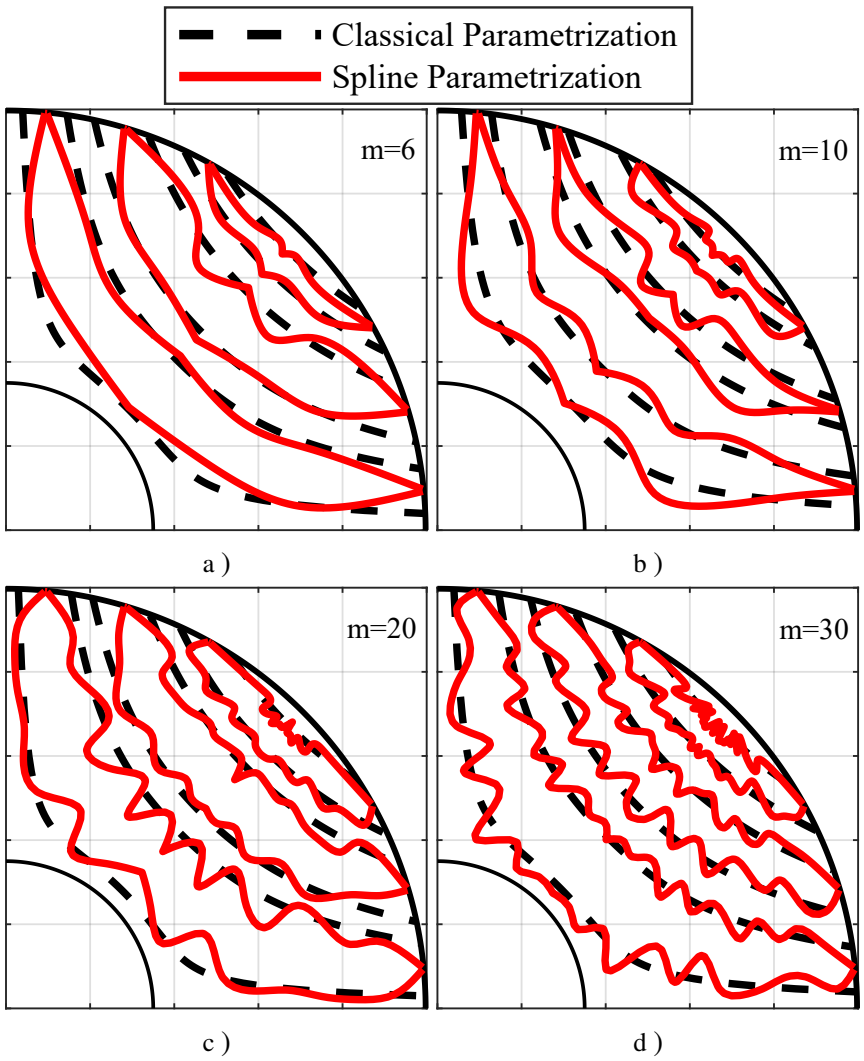


Figure 2.9: Spline barrier profiles formed with different number of control points per barrier: a) m=6, b) m=10, c) m=20 and d) m=30.

Afterwards results will be compared and selected designs will be further analyzed.

General dimensions and properties of the machine have been previously shown in Table 2.1 and they will be used in these optimization studies as well. Similarly, stator will be kept constant. Optimizations will focus on rotor design with specific targets on the torque and torque ripple. Optimization settings are summarized in Table 2.4.

For the optimization of classical fluid barrier shape, 2 variables per barrier a and k_t are used making the total number of variables 6. Compared to 4 variables used in the previous optimization (Table 2.2), using separate k_t values would effect more flexibility and possibly enhance the final results. Considering this a constraint on the average torque objective is added with a value of 98Nm.

Spline barrier's parametrization is performed with a total number of 24

Table 2.4: Optimization variables and objective functions.

Flux Barrier's Variables		
Parameter	Classical Parametrization	Spline Parametrization
$k_{a(1)}$ $k_{a(2)}$ and $k_{a(3)}$ $k_t(1)$, $k_t(2)$, $k_t(3)$ Control points	[0.3 0.8] [0.1 0.5] [0.1 0.9] -	[0.3 0.8] [0.1 0.5] [0.1 0.9] [-0.9 0.9]
Total number of parameters	6	24 (6 + 18) 4, 6, 8 parameters for control points
Objective Functions		
$f_1 : max\ T_{avg}, > 98$ Nm $f_2 : min\ T_{ripple}, < 20$ % $f_2 : min\ P_{iron}$		

varibles. Six of the variables are directly coming from the classical parametrization, a and k_t for per barrier and the rest of them are the control points. Starting from the outermost barrier 4, 6 and 8 control points are used. The number of control points is selected such that shape of the proposed barrier profile does not get over complicated to cause any problems in the mesh or lead to local optima during the optimization, given the high search space dimension.

Objective functions for both optimizations are the same as presented in Table 2.4. One of the targets is the maximization of average torque and the other one is minimization of torque ripple. Additionally, constraints are put to search towards designs having a torque value of greater than 98Nm and a torque ripple value of less than 20 %.

A 2D FEA analysis is conducted for each design during the optimization. Each of these analysis is run for one sixth of the electric period with 1^o mechanical steps. Current phase angle is kept constant for all designs at 60^o. Optimization routine is the same as previously described in Figure 2.4.

MOGA algorithm is selected for the optimization algorithm and total number of designs for optimizations are selected based on the number of parameters to be optimized. For the classical parametrization, a total of 3600 designs are considered through 60 generations having 60 designs each. Higher number of variables for the spline barriers requires higher runs to converge hence a total of 21875 designs are evaluated with 175 designs in 125 generations. Initial population for both parametrizations is generated via Sobol sequences to uniformly distribute

variables in their limits.

2.3.1.1.1 Optimization Results

The results of the optimizations are shown in Figure 2.10 in terms of Pareto designs. It is seen that two sets of results are comparable to each other in terms of average torque and torque ripple. It can be inferred that the spline parametrization can provide higher average torque meanwhile classical parametrization can provide lower torque ripple. Two designs are selected from each Pareto front and are shown in Figure 2.10 with star marks. Designs are selected to have almost the same value of torque ripple 9.8 % but with different average torques to better investigate the difference between them. Average torque of the classical design is 100.5 Nm and the spline design has 101.2 Nm.

Geometries belonging to two designs are depicted in Figure 2.11 drawn on top of each other. Noticeably, the spline design has more air than classical design. This is the main reason that spline parametrization offers better average torque as it has the capability to increase the saliency ratio, enhancing the reluctance along the q-axis, but without obstructing the d-axis iron path, as it would happen with the classical parametrization.

The end-points for both parametrizations remain very close to each other with some slight differences. Even they are minorly distant from each other, these sets of end-points give the same torque ripple. This is reasonable and justified by

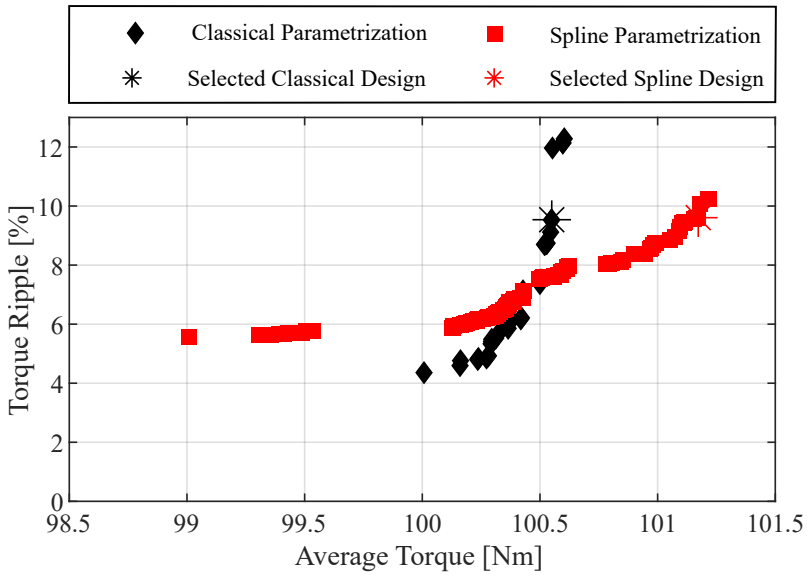


Figure 2.10: Pareto fronts of the optimizations

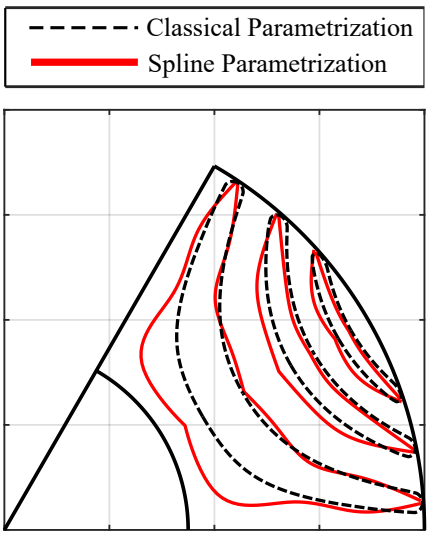


Figure 2.11: Selected designs on the Pareto front

the fact that both fluid and sharp end profiles are saturating, confirming also with [18].

2.3.1.1.2 Analysis of the Optimal Machines

Two designs shown in Figure 2.11 are further analyzed in terms of electromagnetic and mechanical performances. Electromagnetic analysis is re-performed with a finer mesh with a wider range of current amplitudes. Currents increasing from 10 to 160 A_{peak} is analyzed with 10A steps. Exact MTPA condition is searched for each current amplitude by sweeping current phase angle between 45^o to 75^o in 30 equally spaced points and the maximum torque points are calculated. For example at the rated current conditions MTPA is found to be at 57.4 ^{o}. At this point average torque values are 101.1 Nm and 101.6 Nm and torque ripple values are 10.5 % and 10.8 % for classical and spline designs, respectively.

Regarding the other electromagnetic characteristics of the selected designs, average torque, torque ripple, flux linkages, inductacnces, iron losses and power factor are shown in Figure 2.12. Each point in the curves corresponds to the performance at the exact MTPA condition for the consecutive current.

Average torque for spline barrier design is around 0.4% higher than classical barrier design at around rated current conditions. Although this is the case for nominal conditions, due to different saturation characteristics this value increases to about 1.5% at higher currents. A similar effect is also spotted for torque ripple. After the rated current towards higher current amplitudes torque ripple of the clas-

sical barrier design becomes higher than spline design. In terms of flux linkages and inductances in d and q axes, classical design exhibits higher values. Since the q axis flux is also higher, spline design is able to provide higher torque. This can be explained by the well known torque Equation 2.14.

$$T = \frac{3}{2} \cdot p \cdot \left[\lambda_d \cdot i_q - \lambda_q \cdot i_d \right] \tag{2.14}$$

Another important point of consideration is the iron losses as given in Figure 2.12

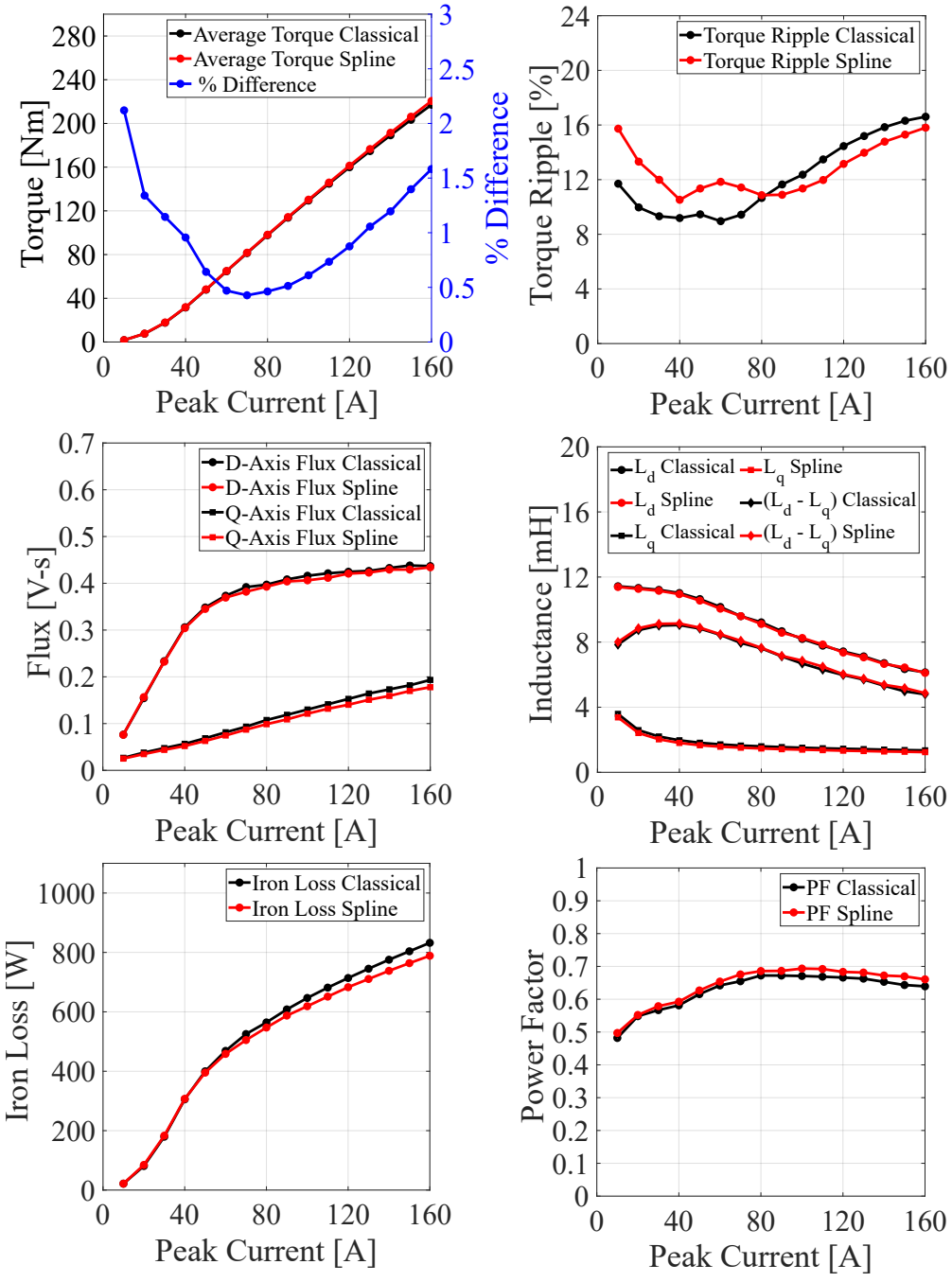


Figure 2.12: Selected designs on the Pareto front

with increasing current amplitudes. Except for low current values, classical design have higher iron losses than spline design starting from 60 A_{peak}. As a last remark, power factor values are shown and compared. Power factor of the spline design is marginally higher than classical design at all values of the currents.

Flux density distributions of two machines are shown in Figure 2.13. There are differences between two flux distributions particularly in the rotor due to the geometrical differences. Additionally effect of rotor geometries also reflected to the stator as expected. Dissimilarities between two distributions are mainly caused by two factors, first one is the shape and thickness of the iron segments and the second is the different form of the end barriers region. Former has a more general effect on the overall flux distribution and performances as the cross-section area of rotor iron segments are primarily effecting the flux. Latter has a more local effect on saturation focused on the tangential ribs. To be more specific it is effecting the value of the maximum flux densities in this area. Due to sharp ends spline design have higher maximum flux density with a difference of 0.2T. Comparing the average flux densities region by region, in the rotor it is 0.97T for the classical design and 1.21T for the spline design. Such difference happens because in general rotor of the spline design has higher flux passing through its iron segments as simple there is less iron compared to the rotor of the classical design. In contrast, average flux densities in the stator are only slightly different with the values of 1.07T and 1.11T for classical and spline design respectively. To comment on the saturation levels along with the iron losses from Figure 2.12, it is seen that saturation levels of the spline design is slightly higher than classical design nevertheless resulting iron loss is lower for the spline design. One of the possible reason for this phenomena is the amount of total iron with the classical design being higher and the other one is the less sinusoidal flux density occuring in the iron segments.

2.3.1.1.3 Mechanical Considerations

As previously stated in Table 2.1 maximum speed of the application requires reaching 10000 RPM. The aim of the optimization was to investigate the torque characteristics of the new barrier shape so any high-speed operation is not considered. However besides from the electromagnetic performance, which changes with respect to speed, mechanical properties of the machine has to be there in order

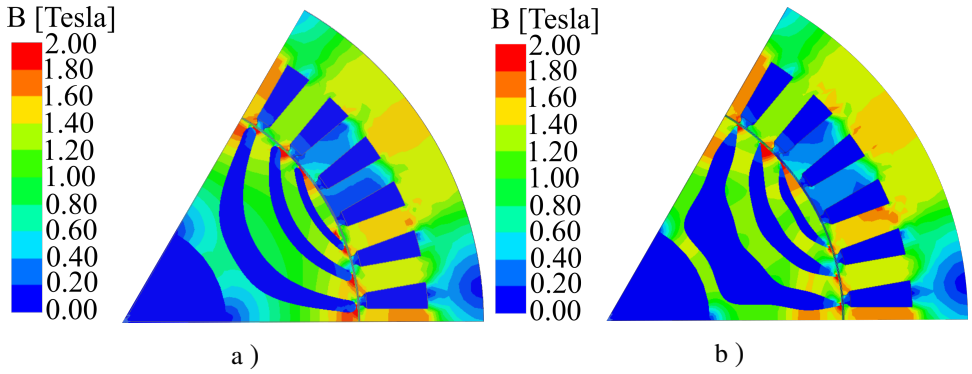


Figure 2.13: Magnetic field distributions of selected classical and spline machines.

to be operational at the maximum speed. To this extent mechanical performance of the two selected rotor designs are investigated.

During the optimization only a 0.5mm tangential rib thickness is considered but this is not adequate for staying under the material stress limits at the maximum speed of 10000RPM. Therefore additional structural ribs acting as support structures are added to the selected designs. Thicknesses of the radial ribs are initially determined as discussed in [29]. From the outermost to innermost barrier, 1, 1 and 2mm thickness of bridge structures are added to the barriers of both rotors on the q-axis. These are shown in Figure 2.14.

Validating the ribbed structure, 2D structral analysis have been carried out by means of FEA at the maximum speed. Results are shown in terms of Von Mises stress as given in Figure 2.14. Classical design has a maximum of 342 MPa stress whereas the spline design has 620MPa. Considering the 460 MPa yield stress of the laminated steel material, classical geometry satisfies this treshold with 1.33 safety factor. In constrast, spline design can not achieve the desired level with a safety

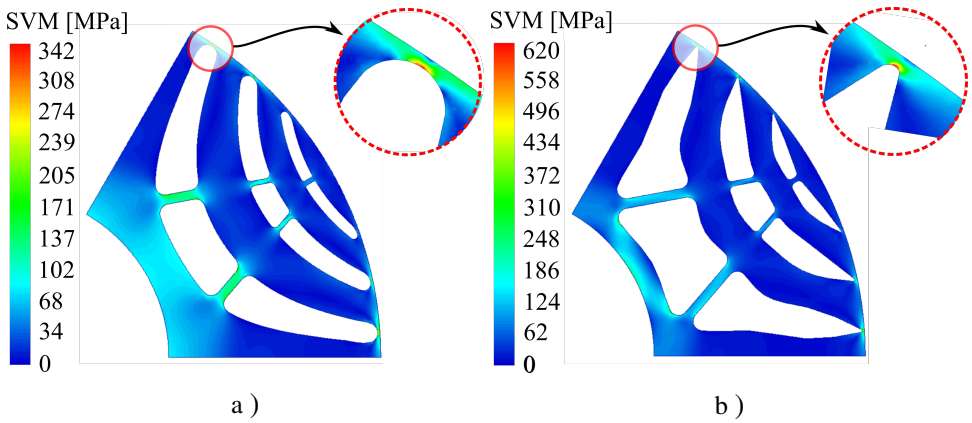


Figure 2.14: Mechanical analysis results: Von Mises stress distribution.

factor of 0.74. The difference between the maximum stress levels mainly happens because of the sharp and round end-barrier shapes which critically effects the nodal stress values. Similar conclusions were also obtained for two end-barrier shapes presented in [18].

In the end-region of the fluid barrier profile, forces acting to the end-parts are uniformly distributed due to the rounded end-shapes. The same is not valid for the spline barrier profile as almost the same forces act in a much smaller area, giving rise to the maximum stress. On the other hand, when other parts are examined such as the radial iron bridges, stress values are mainly the same. This is particularly important because although there is less iron in spline profile design, similar stress levels are obtained other than the end-regions.

In conclusion, the mechanical analysis tells that unless the end-shape is changed, a higher amount of total supporting areas are required. The end-barrier shape is not directly related to the other parts of the barrier such as the insulation ratio which is directly related to the torque production therefore it can be modified. However, in the case the rib thicknesses are increased, torque production capability will be decreased and spline barriers will loose its advantage over the classical barriers.

2.3.2 Parametrization for PM Assistance

The paremetrization explained in section 2.2 describes the general procedure for building the flux barriers. However, it is often required to add PMs in the sense of ”assistance” to the pure reluctance machine to increase performance [10] [11] [12].

The simplest way to accomplish this is to fill the existing flux barriers with PM material. By doing so, a SynRel rotor can be easily converted to a PMaSynRel rotor without any further modifications. On the other hand from practical point of view, curved magnet shapes are often not preferred due to their manufacturing process. For the classical and spline parametrizations these concerns do especially exist. That being said, straight-segmented barriers are much more suitable for introduction of PMs [30]. In this type of barriers any desired part of the barriers can be filled with PMs, although generally, middle part is used.

Another approach, also adopted in this work, is to remove a part of the curved flux barrier and replace it with a rectangular shape so that PMs can be added. The modification is shown in Figure 2.15. Initially the modification has been applied and shown for classical fluid barrier structure as eventually spline modification is built on it.

In Figure 2.15 a) black continuous lines show the flux lines that actually form the barrier and the blue continuous lines show the maximum possible thickness limits of the barrier. To begin with, first the q-axis line which passes through the middle of the barriers are realized. After that, another line parallel to the q-axis is drawn. The perpendicular distance between two lines are determined by the parameter k_{PM} which is typically in the range of [0 1] and is shown with dashed lines with magenta color. This is then followed by the intersection of the newly drawn line and the two lines forming the barrier. Two intersection points thus becomes the two corners of the rectangular magnet. Since this structure is symmetrical about q-axis, the opposite corners are also known. The only remaining process is to remove

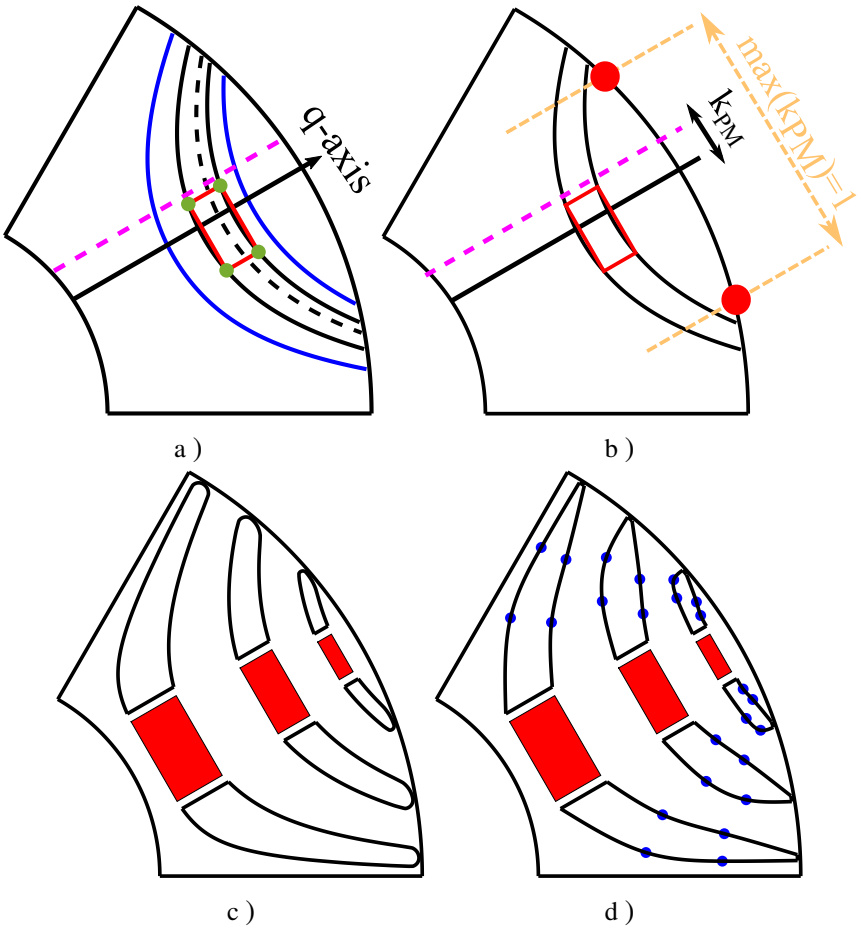


Figure 2.15: Modification of classical parametrization for PM addition.

barrier parts between two symmetrical intersection points for a flux line. With this definition, length of the magnet along the q-axis becomes equal to the barrier at the intersection points. It is further possible to adjust the thickness with an additional parameter to bring more degrees of freedom.

Additionally, if radial ribs are to be considered, initially dedicated rectangular PM area can be shrinked towards the q-axis. In that case, the thickness of the magnet would become slightly smaller than the initial thickness.

Another point of remark is the determination of the maximum value of the k_{PM}=1. End-points of the upper flux line forming the barrier can be selected as a reference, however it would be more practical to select points slightly moved towards the q-axis on the rotor surface (shown with red circles) to ensure some safe space for the flux barriers.

The final PMaSynRel structure is shown with Figure 2.15 c). Until here the methodology is described for the fluid shape parametrization however it can be extended for the spline parametrization. Based on the procedure explained in section 2.3.1, control points can be defined on the remaining part of the flux barriers and spline parametrization can be achieved. To this end, a limited number of control points would be more suitable as the flux barrier area is now considerably smaller. An example PMaSynRel structure is shown in Figure 2.15 d) where the blue dots show the control points. Different from the initial spline parametrization, end-shape of the barriers are made flat by considering a fixed length at the end-point region. Additional PMaSynRel rotor examples created by using random valued parameters are further provided in Figure 2.16 as an insight to show how utilizing splines can lead to increased degrees of freedom for the formation of flux guides.

2.3.2.1 Optimization of the PMaSynRel Rotor

As done in the section 2.3.1.1, in this section as well two optimizations are conducted to optimize the rotor for a PMaSynRel machine. Two optimizations utilizing the classical and spline parametrizations are carried out with magnets to analyse and understand the effect of modifying the barrier shapes in case of a PMaSynRel machine. A low grade, ferrite PM of Y30 is used as PM material. Specifications of the machine has been previously presented in Table 2.1 and the other analysis settings are also the same as the previous one. Same radial and

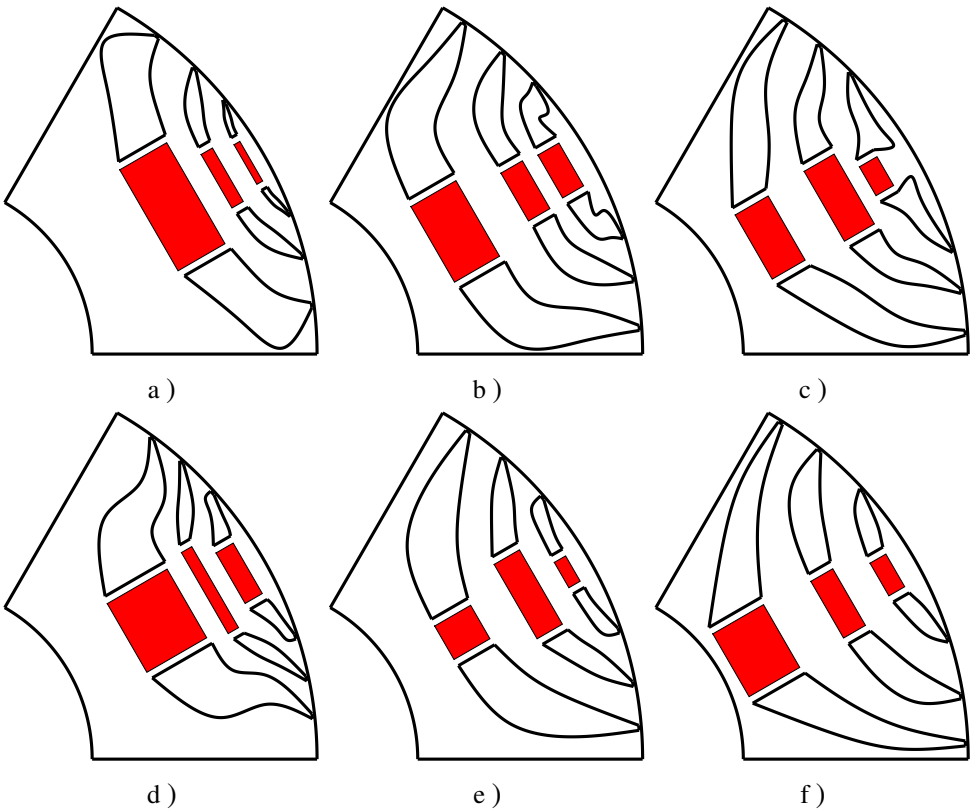


Figure 2.16: PMaSynRel rotors generated using splines and randomly valued parameters.

tangential rib thicknesses previously discussed in section 2.3.1.1.3 are used as predefined values.

Optimization settings are also mostly preserved compared to the previous one presented in Table 2.4. With the addition of PMs each barrier has now one additional parameter k_{PM} therefore total parameters for the classical parametrization is 9. For the spline parametrization number of control points are selected to be 2,

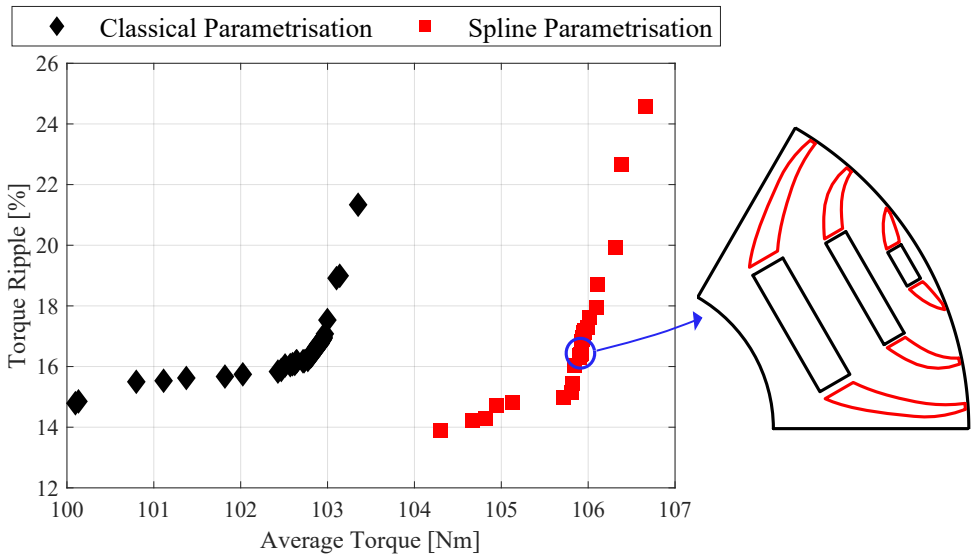
Table 2.5: Optimization variables and objective functions.

PMaSynRel Flux Barrier's and PM's Variables		
Parameter	Classical Parametrization	Spline Parametrization
$k_{a(1)}$	[0.3 0.8]	[0.3 0.8]
$k_{a(2)}$ and $k_{a(3)}$	[0.1 0.5]	[0.1 0.5]
$k_t(1)$, $k_t(2)$, $k_t(3)$	[0.1 0.9]	[0.1 0.9]
$k_{PM(1)}, k_{PM(2)}, k_{PM(3)}$	[0.2 0.6]	[0.2 0.6]
Control points	-	[-0.9 0.9]
Total number of parameters	9	21 (9 + 12) 2, 4, 6 parameters for control points
Objective Functions		
$f_1 : max\ T_{avg}, < 98$ Nm $f_2 : min\ T_{ripple}, < 20$ % $f_2 : min\ P_{iron}$		

4 and 6 respectively for outermost, middle and innermost barriers. Based on the number of variables to be optimized, total number of designs are 9000 and 18000 for classical and spline parametrizations. Objectives of the optimizations are to maximize average torque and minimize torque ripple. A summary of the parameters and objectives are further provided in Table 2.5.

2.3.2.1.1 Optimization Results

Optimization results are presented in Figure 2.17 a) in terms of pareto desings. Average torque and torque ripple values of these are depicted in the figure. Designs with spline barrier shapes achieve higher average torque than fluid barrier shape by a margin of 4%. In addition there is a marginal improvement in torque ripple when the lowest torque ripple designs are compared however in general similar torque ripple levels are achieved. One of the spline designs is selected on the pareto front on the having a good compromise between average torque and torque ripple and shown in Figure 2.17 b). Comparing the results with the previous opti-



a)

Figure 2.17: Optimization results of the PMaSynRel with classical and spline parametrization: a) Pareto front, b) selected design.

mization for SynRel rotor design (Figure 2.10) it is easily noticeable that increment in terms of average torque is in the range of 4 to 7%. The first apparent reason for that is the lack of radial ribs in the previous optimization which would in its presence cause an increase in the q-axis flux and cross-saturation leading to decreased

torque. The other reason for that is the utilization of low grade ferride PMs which is mostly contributing to increased performance in the field weakening region. In order to elaborate on this three machines are further analyzed. The first one is the selected PMaSynRel design optained with spline parametrization from Figure 2.17, second one is the same one as the first but without magnets and the last machine is the selected SynRel design obtained from Figure 2.10. Machines are first analyzed in the *dq* current plane and their MTPA and maximum torque per voltage (MTPV) operations are calculated. Three performance indexes, i.e torque, power and power factor (PF) versus speed characteristics are shown in Figure 2.18. Although a direct

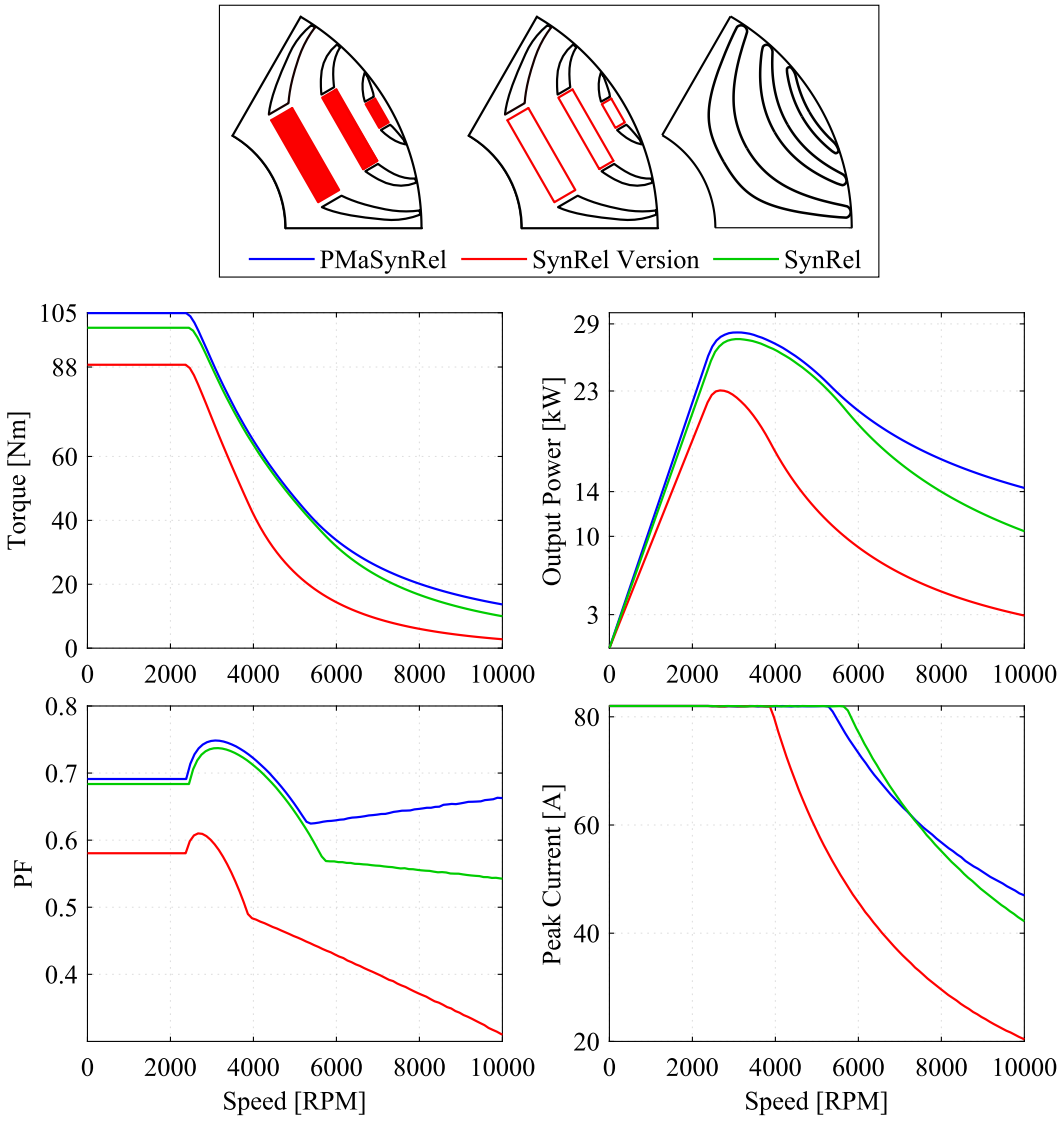


Figure 2.18: Comparison of machine characteristics with and without PMs

comparison would not be fair as the SynRel machine is without the ribs, average torque comparison yields similar values for PMaSynRel and SynRel machines. In

particular, up to around 5500 rpm PMaSynRel and SynRel machines have very similar values in terms of output power and PF as well. It can be deducted that up to this speed, PMs mostly compensate for the performance decrement arising from structral ribs. On the other hand, after this threshold speed PMaSynRel machine overperforms. When current versus speed graph is investigated this threshold speed is actually the limit after which the MTPV starts and current amplitude starts to decrease. PF of two machines also show some similar trends and at the maximum speed of 10000 rpm the difference reaches its maximum.

When the magnets are removed from the PMaSynRel machine, not only torque but also output power and power factor is greatly reduced due to the presence of ribs. It is also seen that MTPV starts at much lower speed compared to the other machines.

2.4 Experimental Assesment

In this section experimental validation is carried out for the previously selected PMaSynRel machine design from section 2.3.2.1 as shown in Figure 2.17. Description of the test setup and the test procedure is first explained and then the results are shared. Test results are compared to those obtained by means of FEA and the discrepancies are discussed.

2.4.1 Skewing of the Rotor

The selected PMaSynRel machine has 106Nm of average torque and 17% of torque ripple. With the aim of further reducing the torque ripple skewing is applied to the rotor. The key here is to reduce torque ripple as much as possible while trying to minimize reduction in average torque. Skewing is well known and widely applied to electric machines of different types mostly to obtain a smooth torque waveform. In [31] skewing is analytically investigated for SynRel machines and it is discussed that a skewing angle equal to a slot pitch is the most beneficial one. Of course this is based on neglecting the nonlinear behaviour of the machine and can change when it is considered through numerical analysis. This aspect has been investigated in [32] [33].

Another important point of consideration is the number of segments when

applying discrete (step) skewing. A high number of rotor segments increase manufacturing difficulty but additionally it gives rise to 3D affects caused by axial flux flow. This effect has been discussed in [34] through comparison of 2D multi-slice and 3D FEA. With these considerations number of skew steps are selected to be 3.

Choice of the skew angle is studied through a simple parametric optimisation where skew angle is varied up to 1.6 times the slot pitch (10 ^{o} mechanical angle). The results of this study is shown in Figure 2.19. The skew angle which gives the minimum torque ripple is found to be around 8 degrees and selected for the application. At this amount of skewing, average torque decreases to 97.2 Nm.

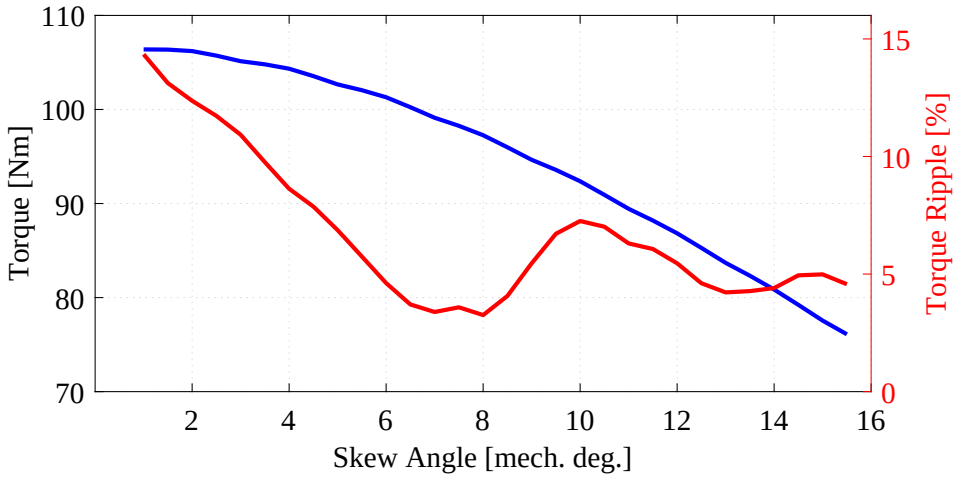


Figure 2.19: Torque and torque ripple with respect to increasing skew angle.

2.4.2 Prototype Machine

Due to supply chain availability and time constraints to obtaining the Y30 grade ferrite magnets, it has been decided to assemble and test the prototype machine without permanent magnets. Due to the time limitations we had been facing, despite the difficulties, it is decided to proceed with a motor without magnets.

Rotor of the prototype machine is shown in Figure 2.20 in the final assembly process before being inserted into the stator. Three rotor stacks have been put together obeying the skewing angle.

2.4.3 Test Procedure and Setup

A picture of the test setup is shown in Figure 2.21 where the load motor, prototype motor and the torquemeter are labelled. Two inverters are used during the

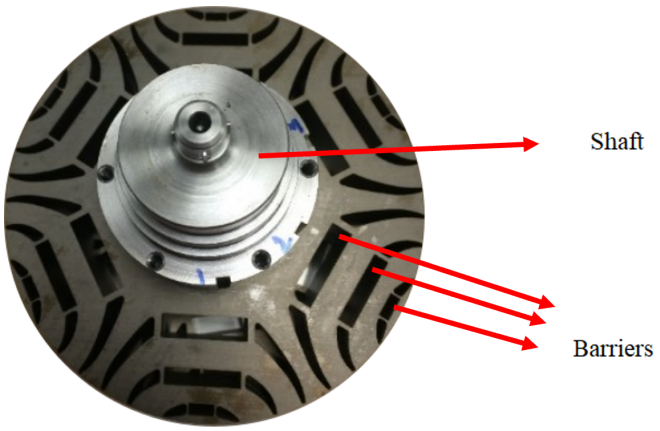


Figure 2.20: Rotor of the prototype motor.

tests, where each controls one of the motors. Load motor is used in speed mode to adjust the desired speed and the prototype motor is used in torque mode. uCube control platform which is developed and implemented within the research group at the University of Nottingham is used to control the motors [35].

The primary aim of the experimental work is to obtain torque versus current characteristics of the machine. For this purpose, dq current plane is divided into a regular grid. With a number points defined for both current pairs (id, iq) with 8A steps a maximum of 80 A_{peak} is reached through a total of 100 grid points. The test is performed at low speed, at almost one third of the rated current to be able to neglect the effect of iron losses.

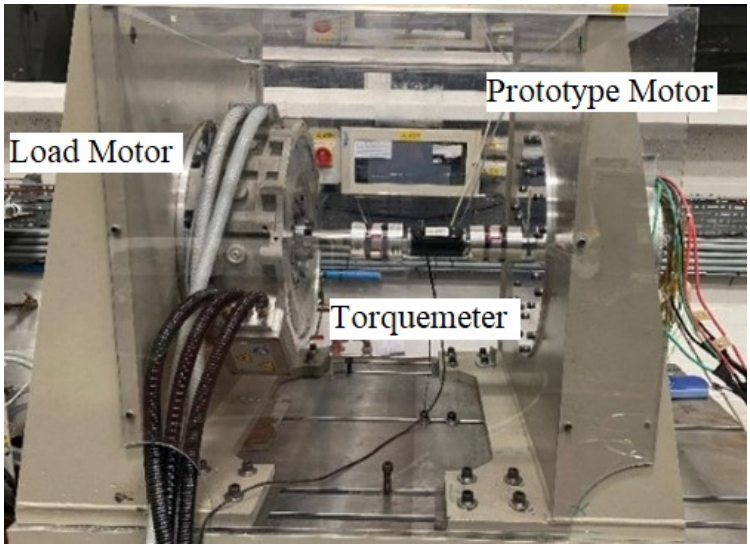


Figure 2.21: Bench setup for the prototype machine.

2.4.4 Results

Test results are given in terms of torque contours in Figure 2.22 in comparison with the results obtained by FEA. Additionally, current circles are shown corresponding to current vectors. Constant torque curves are shown until 110Nm and the machine produces about 90Nm when the supplied current amplitude is 80A.

It is observed that especially towards higher current levels, analysis results overpredict the performance of the prototype machine. The discrepancy between test and analysis results are lower at the more useful operating region where q-axis current is higher than d-axis current but tends to increase mostly in the low q-axis current area with high d-axis current. These differences can be explained mainly by two factors, if measurement errors are neglected. One of them is the difference in the geometry occuring due to manufacturing which alters the all performance and the other being the different material characteristics of the lamination material.

However, in overall results stay in the acceptable margins. Particularly at the rated condition of 82 A_{peak} where MTPA for both machines are very close to 60^o, there is a 5.2% difference between the results.

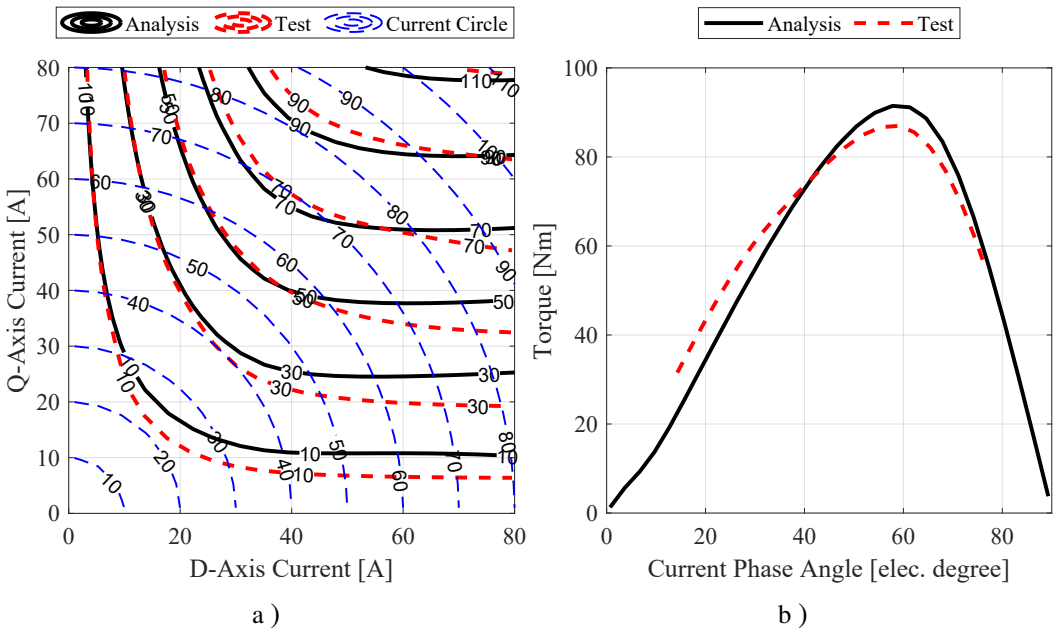


Figure 2.22: Test and analysis results: a) torque contours and b) torque versus current phase angle.

2.5 Conclusion

First chapter of the thesis focused on the design and optimization of SynRel motors with a particular interest in rotor design. Various optimizations are performed with different objectives to comprehend their effect on the final geometry and moreover a novel flux barrier structure is proposed to enhance characteristics compared to conventional type of of geometry.

Starting with the previous work, a good summary of the literature is obtained and state-of-the-art design techniques as well as common practices are discussed. Detailed explanation of geometry parametrization utilizing fluid shaped barriers are given and the number of variables describing the geometry are examined. It is shown that it is possible to increase or decrease degrees of freedom by connecting variables together or making them independent. With a medium number of variables (4) to describe flux barrier geometry, three different optimizations are performed with different target functions and constraints. This study showed that optimizations are quite dependent on the objective functions and considerably affects the results. Distinctly, the effect of selecting minimization of iron loss as a target function is revealed, showing that it can transform the results. On the other hand, it is found out that considering the iron losses without a constraint on average torque does not necessarily yields best results as in this case torque is decreased. Instead, increase of average torque has to be further directed towards a limit meanwhile trying to minimize the iron losses.

After studying the fluid shaped barrier structures, a novel flux barrier shape is proposed. The aim of this new structure is simple: to increase the geometric degrees of freedom which can not be achieved by using classical parametrizations. To achieve this a number of control points are introduced to classical parametrization and the new barrier shape is obtained through merging these control points by using splines. An optimization study is conducted using both classical and spline parametrization and with the expense of higher computational time, some minor improvements are achieved through better utilization of design space thanks to the spline parametrization.

Addition of permanent magnets to both parametrizations are then explained and spline parametrization with PM slots are used to optimize a PMaSynRel

geometry with ferride magnets. For this study, using spline barriers was more advantageous and consequently one of the designs are selected for manufacturing.

During the manufacturing phase, some supply problems prevented to progress as planned and the prototype machine has been built without PMs. Experimental verification of the protoype machine is achieved and compared to the results obtained through FEA. Results show that in overall a good match is obtained.

2.5.1 Possible Future Work and Improvements

For the extension of the conducted work, following points can be followed:

1. Parametrizations can be further enhanced considering the manufacturing tolerances to obtain more robust designs.

2. Optimization of the SynRel machine can be done including the stator and mechanical considerations for a more wholesome design approach. As an additional point, multiple operation conditions and their effect on the geometry can be investigaed.

Chapter 3

Topology Optimization for Synchronous Reluctance Machine Design

In this chapter, topology optimization (TO) is investigated for SynRel machines for a possible design and or refinement tool. After providing previous work in the field, various optimizations are performed on a benchmark machine to evaluate the effect of different topology related parameters. Results are thereby discussed in terms of performance, feasibility and computation time. As a final remark, TO is performed on an existing design to discuss its usage as a design refinement tool.

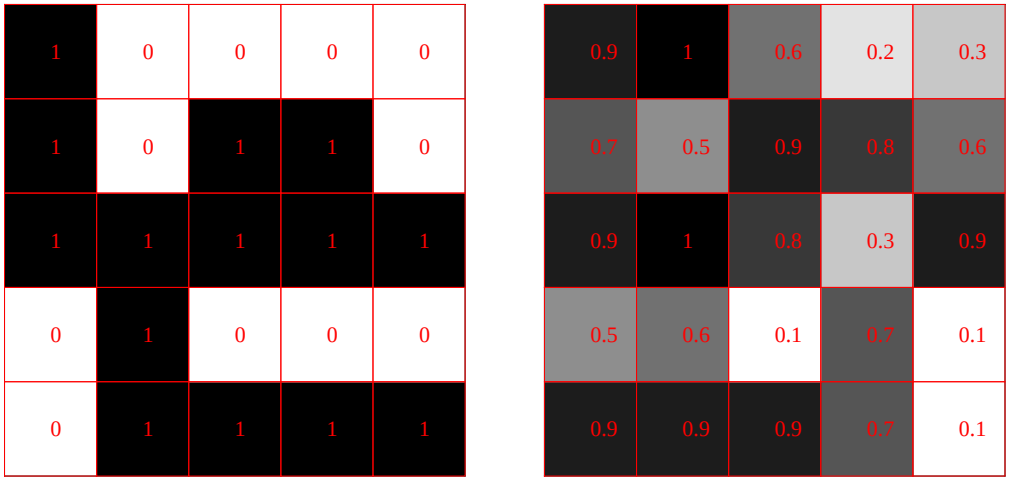
3.1 Introduction

Throughout the years, different design procedures have been applied to design SynRel machines. These mostly focused on the rotor design as the torque generation and other related performances such as power factor and efficiency is dominantly effected by its anisotrophic geometry. Early studies mainly revolve around analytical approaches to form flux barriers in order to maximize the saliency, thus increasing the electromagnetic torque. Along with that, minimization of torque ripple which is generally linked to noise and vibration is studied [8] [36] [37]. These works provided a strong basis for future research where the FEM is adapted and used with computation algorithms to effectively optimize the flux barrier shape. Traditionally, optimization of a SynRel rotor aims to find optimum geometric pa-

rameters describing a specific shape. As discussed in the previous chapter, different flux barrier topologies exist however circular [16], fluid-shaped [38] and straight-segmented barrier structures [20] [21] are most commonly stuied in the literature. In [15], these different flux barriers are compared in terms of performance and time required to converge for an optimal solution and it is shown that each of them presents advantages and disadvantages.

The optimization undertaken with specific geometric parameters for a certain shape is proven to be a very effective design approach for reaching the objectives in a limited time frame. On the other hand, the parameters being related to a single structure naturally limit the exploration space. Even in the best condition that global optimum is achieved with a parametric optimization, it is not necessarily the best solution among other geometric structures. For this intriguing problem, using TO can be a key as it is not limited by any pre-defined shapes. It aims to find the optimal structure based on the distribution of materials rather than template-based geometries.

TO is originated from mechanical design prospects. Among the initial works, a practical application based on the homogenization method (HM) is presented [39]. A modified version of this method is proposed in [40] and thus TO is introduced to electromagnetic devices. Since then, an increasing interest has occurred and many methodologies have been developed while some are combined together to design electrical machines. Among the different methods, On/Off method, density method (DM) and level set method are the most popular ones. The idea behind the On/Off method, as the names suggests, is to simply turn on and off the materials for a given discretized design space. This is shown with a basic example in Figure 3.1 a), where a design space is represented with a 5x5 rectangular grid. Assuming that only two materials are considered, blocks shown with black color (=1) represents iron and the ones shown with white (=0) represents air. The number of materials can be increased for more complex problems. For the discretization of the design space, since the common practice is to use FEM in electromagnetic analysis, a practical approach is to directly use finite elements. It is important to underline that discretization has a tremendous effect in the On/Off method. Resolution of the design space can be increased or decreased by changing the number of elements. As a result, one can assume a better solution can be obtained but this



a) On/Off method b) DM

Figure 3.1: Description of design spaces usuing On/Off method and DM.

brings computational complexity to the design problem. Total number of possible material distributions exponentially increase and can be shown with the formula $m_n^{e_n}$ where m_n stands for number of materials and e_n is the number of elements. For m_n=2 and n_e=25 as in the shown example of Figure 3.1 a), there are 2^{25} varieties of the final design space with different distribution of materials and in that number it is possible to find global and local optimums. Using On/Off method, PM poles of a surface permanent magnet (SPM) machine is studied in [41]. An area is discretized into 100 quadrilateral elements and two materials, PM and air are switched on or off to find the optimal distribution. A heuristic algorithm is used for the optimization, relying on a simple updating scheme. Two different optimizations are performed with these settings, one starting from a full PM design space and removing PM materials and the other starting from a design space composed of air and adding PM materials to it. Expectedly, these two optimizations produce different sub-optimal results, with the optimization starting from full PM design space performing better. Obviously between these two cases initial solution composed of PM is much closer to the target functions (maximising induced voltage and reducing reluctance torque) and produces much more feasible results. Later another set of optimizations are undertaken with an additional iron material. In these ones, much complicated structures are obtained which would only be possible to manufacture using composite materials.

A SynRel machine is optimized in [42] using a stochastic algorithm, i.e

genetic algorithm. Starting from a simple structure resembling three layers of flux barriers, TO was applied to optimize a full rotor. Because the design space was discretized into quadrilateral elements, a smoothing process is introduced to the final design to smooth sharp corners.

A variant of the classical On/Off method is used in [43] by employing normalized Gaussian network. In this method, rather than controlling material of each cell individually, a number of Gaussian functions are used to determine the materials therefore enough number of Gaussian functions need to be used to well-cover the design space. Additionally by using two Gaussian networks, it is possible to obtain four different materials. Authors use paralleled local search algorithm together with genetic algorithm to accelerate optimization progress. Optimization focuses on an IPM motor which can have two different magnet materials, iron and air. Optimization settings related to number of Gaussian functions, their sizes and intersections are studied by means of different optimizations considering both magnetic and mechanical objectives. According to the results higher number of Gaussians with good amount of intersections tend to result in better distributions. Later this study is extended to also optimize a SynRel rotor [44] where an outcome of the optimization is shown in Figure 3.2. Gaussian network based On/Off topology optimization is then

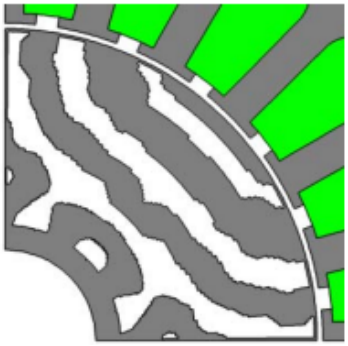


Figure 3.2: SynRel rotor structure obtained by TO process as presented in [44].

used in another study [45] for design of a line-start SynRel machine. Clear representation of Gaussian functions and shape production are presented in this work as shown in Figure 3.3. Authors use initial screening during optimization to identify if the obtained shape is one-piece or not. Only those feasible are then admitted to the second phase where a steady-state analysis takes place. After this stage, third stage which is the transient analysis phase begins to make sure starting torque can be reached for self-starting. Only the designs which are obeying the objective functions

are subjected to the transient analysis due to high computational burden. Although the number of variables are much more decreased (40 Gaussians) with the adaption of Gaussian network, total optimization time is noted to be one and a half months. As an extension of this work, a similar optimization approach is adapted to design line-start, internal permanent magnet (IPM) machine in [46]. Amongst the other

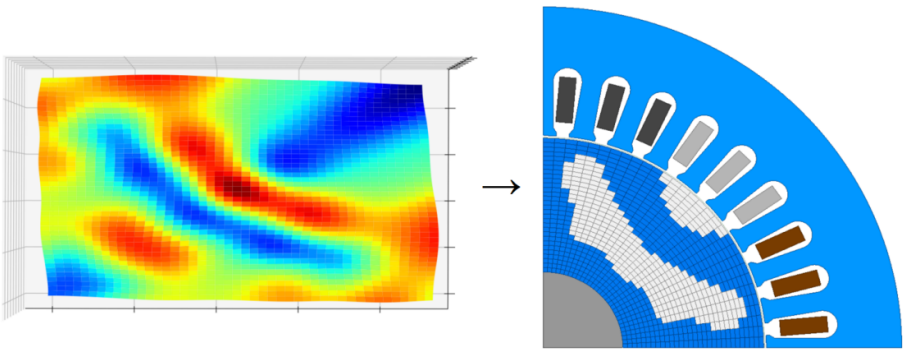


Figure 3.3: Shape production based on Newton Gaussian Newtork as presented in [45].

methods, DM found itself a good place in the literature along with On/Off method. One of the root works investigating this method has been presented in [40]. In the study it is referred as ”optimized material distribution”, but ”density method” and ”solid isotrophic matrial with penalisation” (SIMP) are also used in the literature. DM can be thought as a different implementation of the On/Off method. Instead of elements that can have material properties varying between two extreme points such as 0 and 1 they can attain also the values in between. This is shown in Figure 3.1 b) where some cells are colored in tones of gray with values between 0 and 1. These are called intermediate materials and are basically neither air nor iron but somewhat in the middle with respect to their value.

The number of variables to be optimized using DM is high due to to the fact that it represents the material properties of the cells that make up the design space. Nevertheless as opposed to On/Off method variables are continuous. This is particularly important as derivative based optimization algorithms can be effectively used. In fact, most of the recent studies utilizing this method relies on the gradient-based optimization algorithms due their fast convergent nature. With this being said, a certain direction needs to be found with gradient-based algorithms, thus sensitivities are required to be known. To find the derivative for each variable with numerical methods such as finite difference methods require running the analysis

for each variable creating immense computational burden. For this reason, adjoin variable method (AVM) is frequently implemented to calculate sensitivities. Using AVM, it is possible to obtain sensitivities with a single evaluation of the objective, greatly reducing the computational burden [47].

DM is applied to a simple C-core actuator system using multiple design spaces with different materials in [48]. Sequential linear programming (SLP) is used as the specific optimization algorithm. Air, iron, PM and coil distribution are the design space materials for maximising the force.

Optimization study of a magnetic coupler is studied in [49]. In this study element sensitivities are obtained using finite difference method. Different interpolation schemes between materials are considered by controlling the exponential term named the penalization coefficient. Effect of changing this variable to the final results are discussed.

Interpolation formula is shown with Equation (3.1), where μ_0 is the permeability of vacuum, μ_r is the relative permeability, p is the normalized density between 0 and 1 and n is the penalization coefficient. In general this interpolation scheme is known as polynomial scheme and degree of the polynomial can be controlled with n. Other interpolation schemes are also used in various studies and are summarized in [50]. For the sake of clarity, interpolation scheme with increasing value of the penalization coefficient is shown in Figure 3.4 when mu_r=1000. Use of penalization coefficients higher than 1 is generally considered to minimize intermediate materials. Clearly, using an increased number of n pushes p to become 1.

$$\mu_i = \mu_0[1 + (\mu_r - 1)\ pi^n] \tag{3.1}$$

In another study, an actuator and a PM model are optimized [51] . TO problems are repeated using different initial values (for example starting from p=0, $p = 0.5$, etc...) and results show that this has a marginal effect on both objective value and final geometry. Penalization coefficient is also analyzed in the aim of removing the intermediate materials however this approach ended up to create convergence problems.

A switched reluctance machine (SRM) is studied in [52]. In this study instead of using AVM or finite difference method to obtain sensitivities, analytical

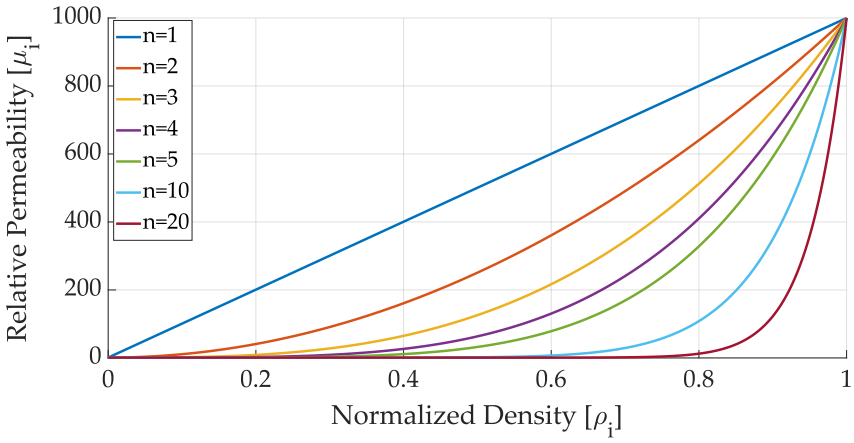


Figure 3.4: Various interpolation schemes characterized by increasing values of the penalization coefficient for permeability mapping$n$.

sensitivities are used. Both stator and rotor of the SRM are optimized considering also the drive parameters as optimization variables. Compared to the initial model, torque ripple is successfully reduced with some decrement in the average torque.

An IPM machine has been optimized by using method of moving asymptotes (MMA) as the primary algorithm. AVM is used for obtaining the sensitivites with respect to average torque and torque ripple. Two different magnet placements are initially chosen and kept constant through optimizations. Special consideration is given to eliminate intermediate materials by using an additional filtering objective.

One of the extensive works revolving around SynRel machines is presented in [53]. With the aim of improving the sensitivity based nature of the DM and to converge towards a smooth material distribution, authors start from a design space with random hollow circles. A sensitivity filtering is further applied and different results with different filtering radii is shown. It was shown that by using a larger filtering radius it is possible to obtain more manufacturing friendly structures.

Three dimensional (3D) TO is applied first to an electromagnet and the pole head of a salient pole synchronous generator in [50]. Author here uses an additional objective function, called filtering function, to effectively reduce the amount of intermediate materials.

A coupled magneto-structural TO is applied to wound field synchronous machines to optimize its rotor, focusing on the winding and the core area in [54]. Results obtained using TO is compared to results obtained through a conventional

parametric optimization and it is shown that better and feasible results are possible. Later a similar method is applied to the design of SynRel machines [55] with and without pre-formed rotor bridges.

In the light of previous work available, it is safe to say that TO is already a popular topic not only in simple electromagnetic devices but also in complex ones such as electric motors. While there are a number of works focusing on electric machines, there are still a few studies focusing on SynRel machines. When complex anisotropy requirements of this specific machine type is considered, obtaining an optimal solution using TO is even more challenging compared to parametric optimization. On the other hand, TO can hold invaluable insight for SynRel machines as it can remove the boundaries of classical parametric design routines.

In this part, through the analysis of various optimization settings, usage of DM based TO is investigated for SynRel rotor design. As a distinguishing factor, a number of optimizations are performed on a benchmark machine and effect of critical parameters are addressed. Effect of mesh structure, initial density, penalization coefficient and optimization objectives are deeply investigated compared to a benchmark machine obtained with parametric optimization. Additional work is also provided to elaborate on the usage of TO as a design refinement tool through application on an already optimized design space.

3.2 Methodology

A commercial FEM software, JMAG Designer, is used throughout this chapter. It is selected to be used due its implementation of DM and other electromagnetic analysis capabilities. To perform a DM based TO, it is required to have internal control over FEM solution steps. Instead of going through complex and time-consuming development of an in-house FEM package, it is found to be appropriate to proceed with an existing software. In JMAG, finite elements are directly used as cells which can attain different material properties for DM. These are the center of TO as they act as sole variables of the optimization. A modified version of the interpolation formula previously shown with Equation 3.1 is used internally and given by:

$$v_i = v_0 \left[1 + (v_r - 1)\ pi^n\right] \tag{3.2}$$

In this interpolation function, reluctivity is used and interpolated instead of permeability. In Figure 3.5, Equation (3.2) is shown with increasing number of n.

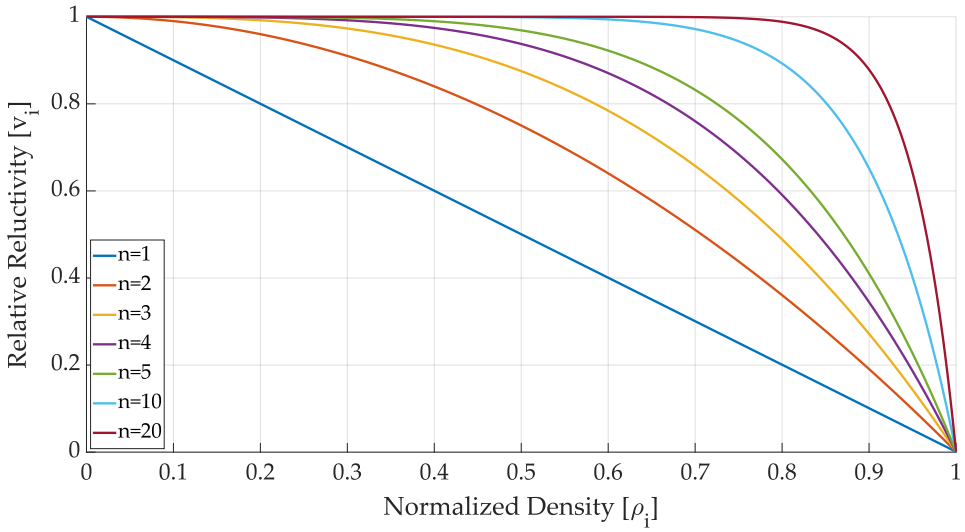


Figure 3.5: Various interpolation schemes characterized by increasing values of the penalization coefficient for reluctivity mapping$n$.

Maximum value of reluctivity is taken as 1/1000 to be easily compared with Figure 3.4. This value is reached when p becomes equal to 1. Distinctively in reluctivity mapping (for $n > 1$), for the low values of p, relative reluctivity becomes close to air reluctivity. This basically creates a possibility to greedily push p to become closer to 1. The effect of using reluctivity mapping instead of permeability mapping is discussed on case problems in [56]. Based on the findings, authors deduce that using reluctivity mapping smoother sensitivities can be obtained leading to less intermediate materials. All the optimizations that are conducted considers the nonlinear behaviour of the materials. In contrast to Figure 3.5, which is created for demonstration purposes, reluctivity is in fact a function of flux density changing with respect to material properties. Additionally, symmetrical rotor poles are considered through mirroring the mesh thus variables between two sides of the middle axis (q-axis). It is possible to consider the full rotor with or without periodicity to come up with asymmetrical pole structures however this aspect is not considered as the aim is to investigate other properties of TO. The optimizations will be performed based on gradient search meaning that after the sensitivities are computed using AVM, material densities will be appropriately changed with respect to the objectives.

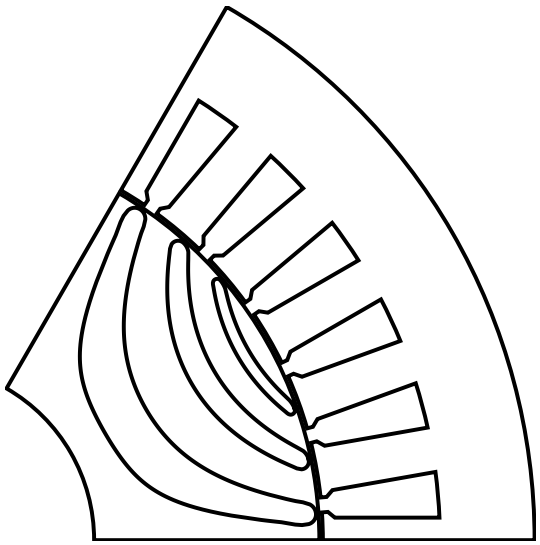


Figure 3.6: Benchmark SynRel machine obtianed with parametric optimization.

3.2.1 Benchmark Machine and Analysis Settings

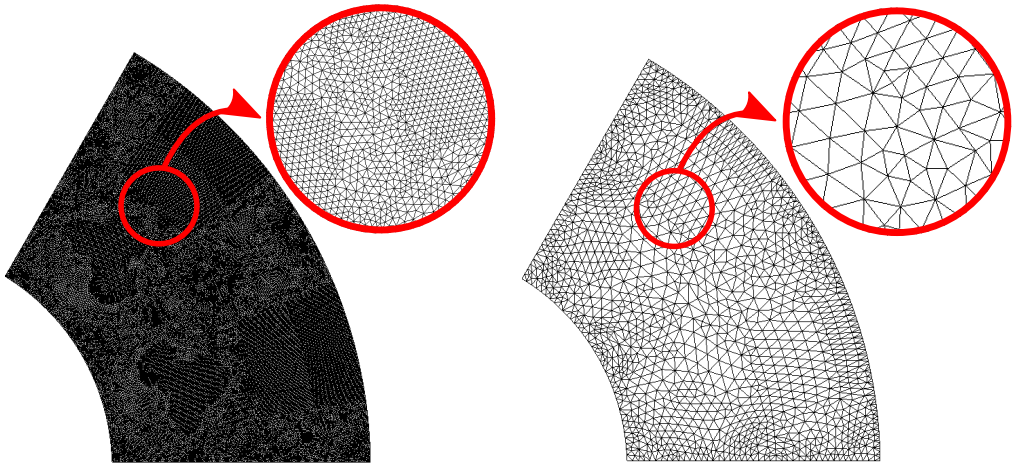
Results obtained through execution of TO are intended to be compared with a machine designed using a traditional, parametric optimization. For this purpose, the selected machine design (classical parametrization) from Figure 2.10 is used. General dimensions of this machine has already been given in Table 2.1 and the resulting geometry is shown in Figure 3.6. For the optimizations that will be presented onwards, one sixth of the electrical period is analyzed with 1^o mechanical steps. A current phase angle of 60^o electrical degrees and a current amplitude of $82A_{peak}$ is used. It is worth mentioning that, in these conditions benchmark machine produces 100.8Nm and 7.3 % torque ripple due to slight differences between material property definitions in Ansys Maxwell and JMAG.

3.3 Optimizations Starting from an Empty Design Space

In this section, effect of mesh intensity, initial design space material properties, penalization coefficient and objective functions will be investigated. All the examinations will be performed starting from an empty geometry. Only maximization of average torque will be considered but after that another case study with minimization of torque ripple will also be provided. Although a structural analysis is not performed during TO, a bounding layer which is not included to design space is included. This way it is guaranteed all results have the same tangential rib of 0.5mm, which is also the case with the benchmark machine.

3.3.1 Effect of Discretization

Discretization, in this case finite element mesh, directly affects the performance of any conducted analysis. Normally when there is a geometry, performance of the mesh is measured as the ability to represent the geometry. Additionally, mesh settings are often changed for different parts of the geometry with respect to any foreseen sensitive parts. An example for this is the concentrated mesh in the airgap region for electric machines. Moreover, there is a tradeoff between the number of elements and the performance in terms of computation time. After the mesh is saturated enough, electromagnetic performance does barely change with respect to increasing mesh but increases the computation time. In the case of TO, a similar trade-off does exist between the computation time and resolution of the design space. The concern here would be to obtain a mesh fine enough so that TO will not be restricted to produce satisfactory results within time limitations. To examine this effect, four different mesh intensities are set and analyzed. Sides of the triangular mesh are increased starting from a maximum length of 0.25mm to 2 mm with 0.25mm steps. Minimum and maximum cases are shown in Figure 3.7. Total mesh size on the left is around 7000 elements and on the right it is around 88000. Using



a) b)

Figure 3.7: Maximum and minimum mesh densities used for optimization; maximum length of: a) 0.25mm and b) 2mm.

four different mesh intensities, TO is performed with the objective of maximizing average torque. Penalization coefficient in this case is 1 and initial density for the design space is 0.9 (very close to iron). Number of iterations were limited to 300 for each model, even though the computation time was dominantly determined by

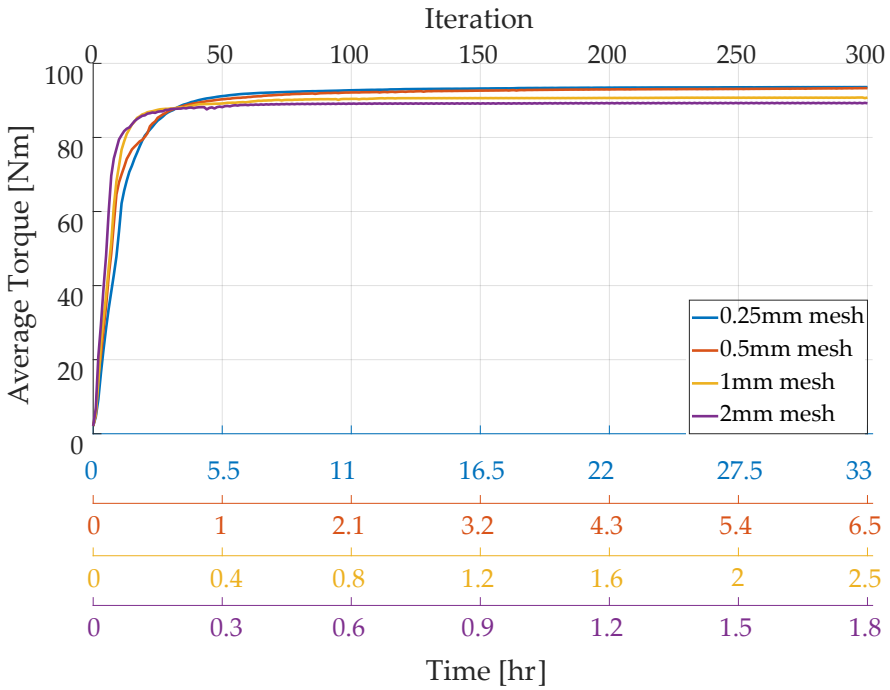


Figure 3.8: Optimization results considering different mesh settings.

mesh density. Optimization results are shown in Figure 3.8 which depicts iteration and computation time versus average torque. Models with a maximum mesh length of 1 and 2mm reach their knee points (the point after which there is only incremental gain) at around 30^{th} iteration where the others reach this treshold around 45^{th}. This might be insignicant in terms of iteration number though it says that sensitivities of cells with respect to material are lower thus the speed which they evolve is also lower. The best cases result in 97.5, 97.2, 94.7 and 93.2 Nm average torque for decreasing mesh intensity. With the increased resolution of the design space, it became possible to obtain better designs by compromising the computation time. Quantitatively, there are 31 hours of difference in time and 4.5% difference in torque between 0.25mm and 2mm mesh. Distribution of material and flux densities of the best designs are given in Figure 3.9 to show the converged topologies that resemble flux barriers. Even though a bounding outer frame is used, models with 0.5 and 2mm mesh do not have a feasible mechanical connection to the frame. This points out the need to add further constraints to the optimization process related to manufacturing feasibility or a refinement stage in order to make the optimal solution feasible. Nevertheless, among analyzing all the optimal solutions, it is evident that there are negligible amounts of intermediate materials that do not represent any major challenges for shape definition.

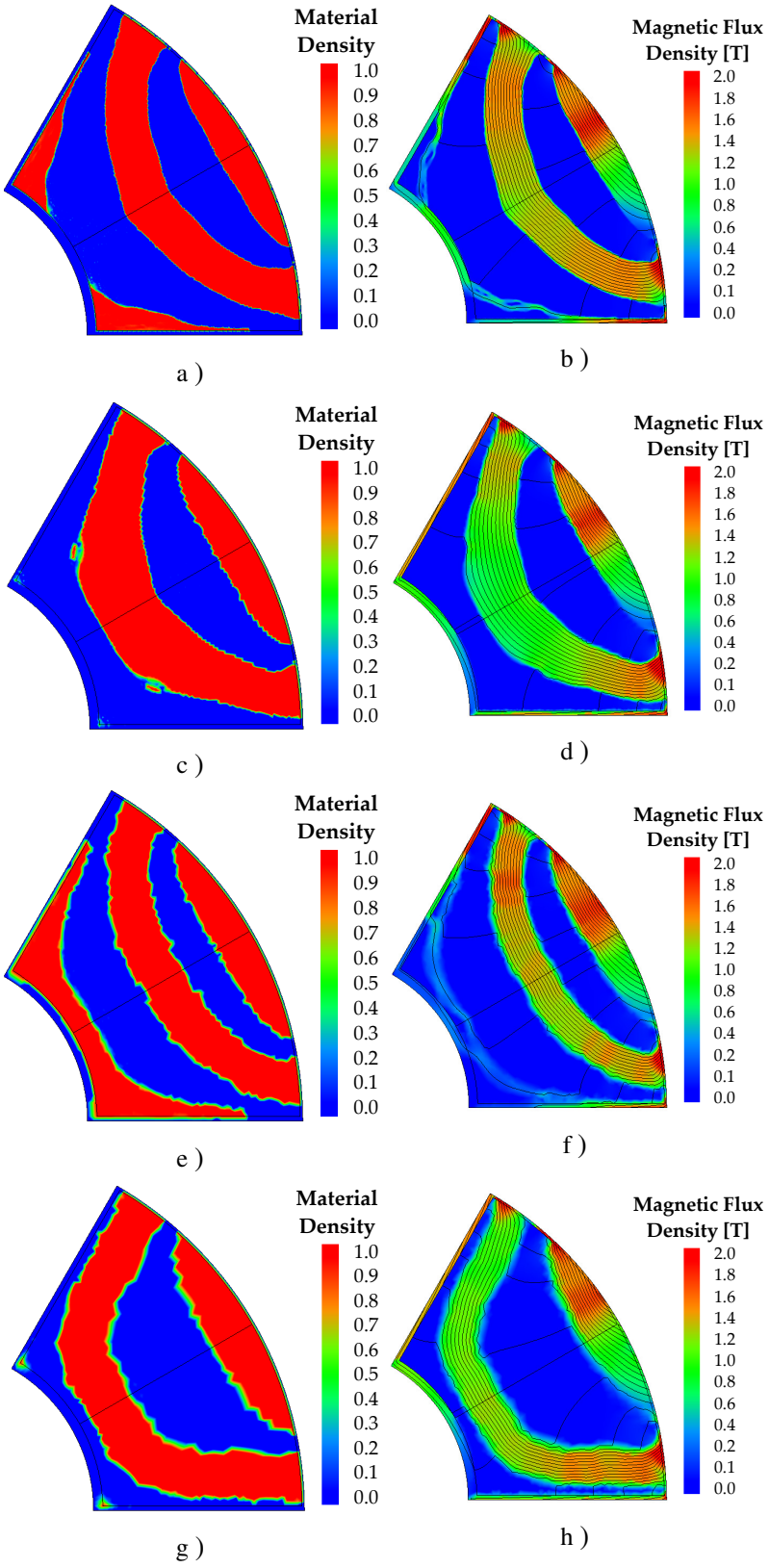


Figure 3.9: Material and flux density distributions for optimization results with increasing mesh intensity: a) 0.25mm mesh material distribution, b) 0.25mm mesh flux density distribution, c) 0.5mm mesh material distribution, d) 0.5mm mesh flux density distribution, e) 1mm mesh material distribution, f) 1mm mesh flux density distribution, g) 2mm mesh material distribution, h) 2mm mesh flux density distribution.

3.3.2 Effect of Initial Density

Initial distribution of material properties in the design space is another important factor in the TO. This parameter basically determines the initial solution that the optimization will build on. To investigate its effect on the final performance and material distribution, a design space using 1 mm mesh is used. The reason for selecting this mesh intensity depends on the previous results where reasonable computation time and a good overall performance is obtained compared to others as shown in Figure 3.8. Three different optimizations are performed starting with initial density values of 0.2, 0.5 and 0.9 where the penalization factor is 1 for all the cases. Results of these are shown in Figure 3.10. Marginally different average torque values are obtained as 94.3, 95.2 and 94.7 Nm for increasing initial densities. Although final torque values are similar, from convergence point of view; starting from a design space whose material properties are closer to air required higher iterations to reach the knee-point. This behaviour can be explained by the low sensitivities obtained in the early stage of iterations encountered with low densities. Distribution of material densities are shown in Figure 3.11, Upon investigation, it is seen that best designs obtained with initial densities of 0.2 and 0.5 have more intermediate materials compared to the one starting from more iron like material distribution. Moreover, in these two cases although some iron is obtained towards the shaft, there is barely a proper connection between the parts other than the bounding frame. In reality, flux is only flowing through first and second segments because the iron path created with the aid of bounding layer is saturated.

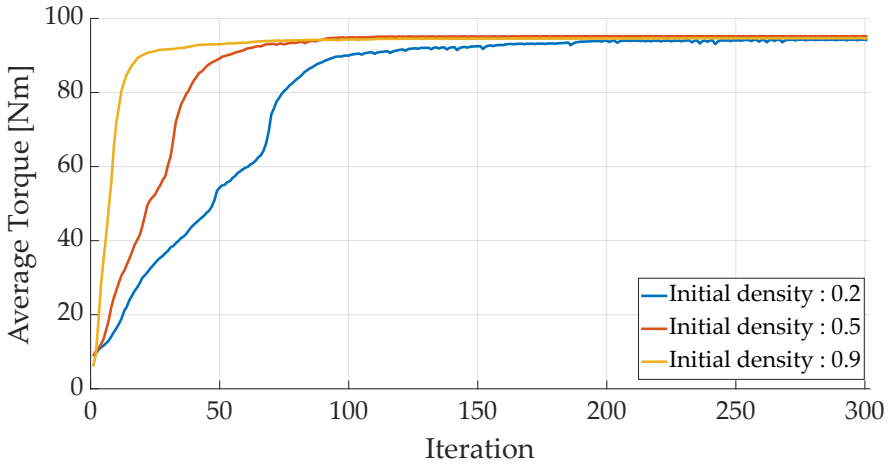


Figure 3.10: Optimization results considering different starting densities.

It can be said that, the bounding layer is acting as a limiting aspect, but actually the more general explanation is probably the lack of any objective pushing towards low torque ripple. In this case of torque maximization objective, a two piece iron segment was enough to generate torque and the whole optimization evolves correspondingly. Apart from these observations, it is clear that the initial starting point has only a little effect on the objective values. A similar conclusion was presented in [51], though the target device in that work is a magnetic shield which has relatively less complex geometric requirements. Combining all these results and considering the material distribution is affected by the complexity and nature of the problem, there seems to be not a major effect of initial density at least in the case a total uniform initial distribution. However it would not be appropriate to generalize this effect for different electromagnetic devices.

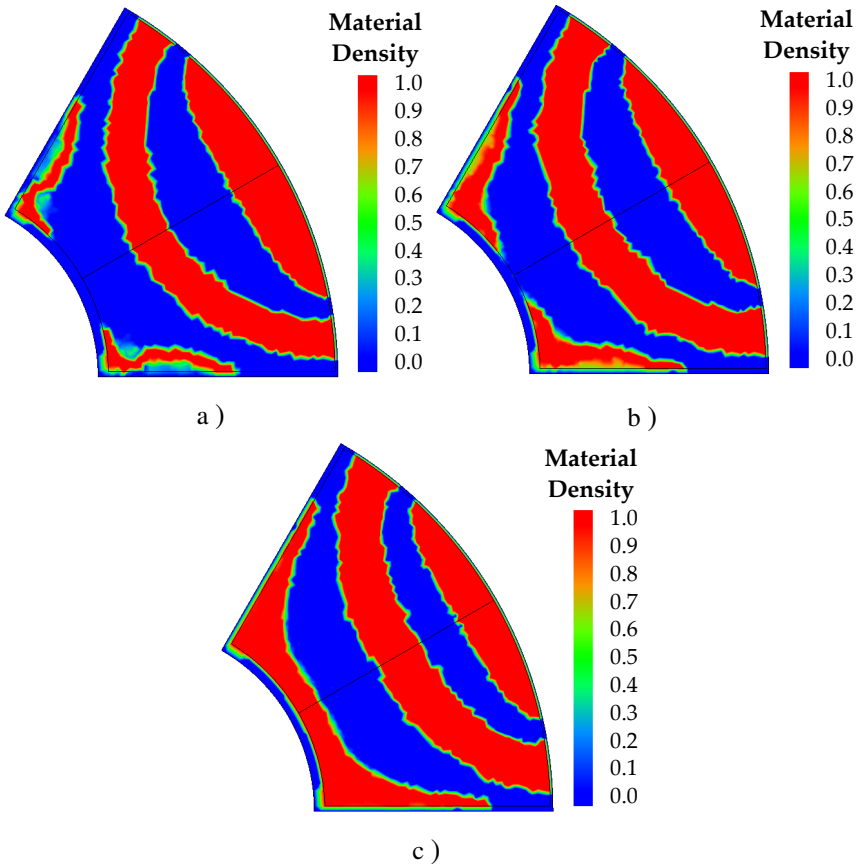


Figure 3.11: Material distributions for optimization results with increasing initial densities: a) p= 0.2, b) p=0.5, c) p=0.9

3.3.3 Effect of Penalization Coefficient

The exponential term in Equation (3.2) has the possibility to produce better results by changing the gradient at which the material properties change. To assess this dependency a number of optimizations are performed on the 1mm mesh model starting from a design space of p=0.9. Starting from a penalization coeffi-

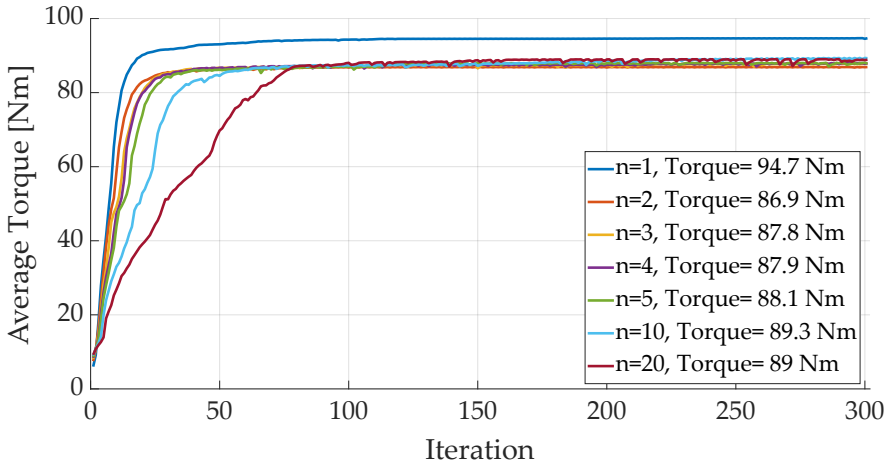


Figure 3.12: Results of optimizations with different penalization coefficients.

cient n=1, a total of 7 cases are considered. The results of these optimizations are shown in Figure 3.12. Clearly values of n=10 and n=20 are extreme situations as shown previously in Figure 3.5. Actually, initializing the design space with p=0.9 for all values of n can be considered as an unfair practice due to the fact that p=0.9 for increasing n means that material properties become much more like air. Based on Figure 3.12, it is possible to see this as a reflection because with the increasing n the number of iterations required to reach the knee-point increases.

Material distributions for the best cases are given in Figure 3.13. Apart from the case n=1 which is not in this figure but the same as the one shown in Figure 3.11 c) and n=20, all distributions resemble each other. There seems to be tendancy of increasing intermediate materials with increasing penalization factor. However, from Figure 3.5 it is also known that with the increasing n, material properties become increasingly more like air. It might be possible to further increase the number of iterations to obtain less intermediate materials but evidently, increasing the penalization coefficient with the starting density of 0.9 worsens the objective result. Based on the fact that initial density changes with respect to the penalization coefficient, some additional optimizations are performed to examine the effect of

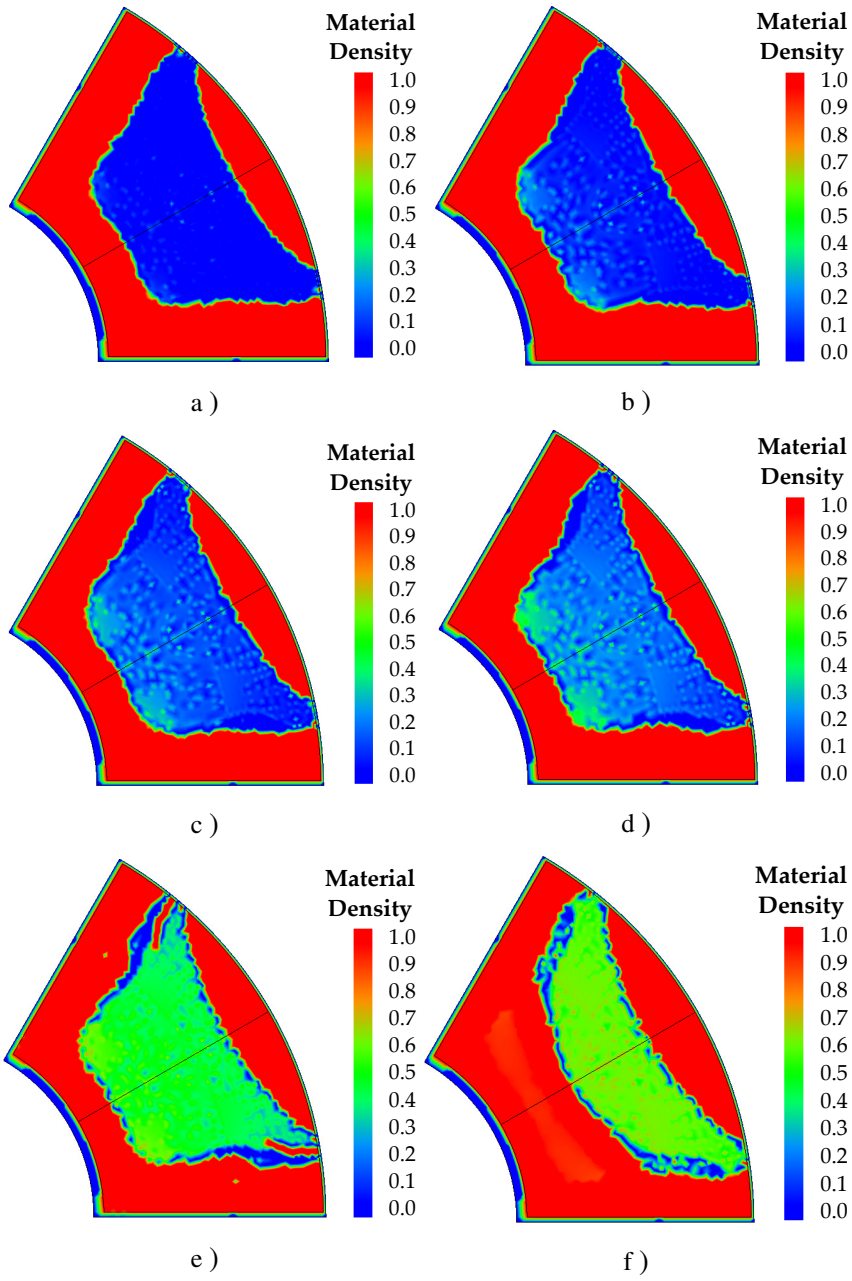


Figure 3.13: Material distributions for optimization results starting from p=0.9, with increasing n: a) n= 2, b) n=3, c) n=4, d) n=5, e)n=10, f)n=20.

both initial density and penalization factor. Initial densities of 0.2, 0.5, 0.7 and 0.95 are selected together with penalization coefficients of 2, 4 and 10. The results of these optimizations are presented in Figure 3.14. With these cases, unlike the ones obtained in Figure 3.12, it is seen that some higher torque values are obtained. It is seen that for different values of n, increasing initial density leads to different solutions due to their changed material characteristics. Material distributions belonging to highest torque best cases are given in Figure 3.15. Material distributions actually point out that all distributions are very similar from magnetic point of view as the flux flow is only achieved through two segments. Besides, apart from the distribution obtained with n=10 p=0.7 all distributions look alike. Additionally average torque of these designs are extremely close to each other however when n increases amount of intermediate materials increase. Combining with the results shown in Figure 3.14 and Figure 3.11, it can be deduced that for this case of a SynRel rotor, n=1 and n=2 yields best results.

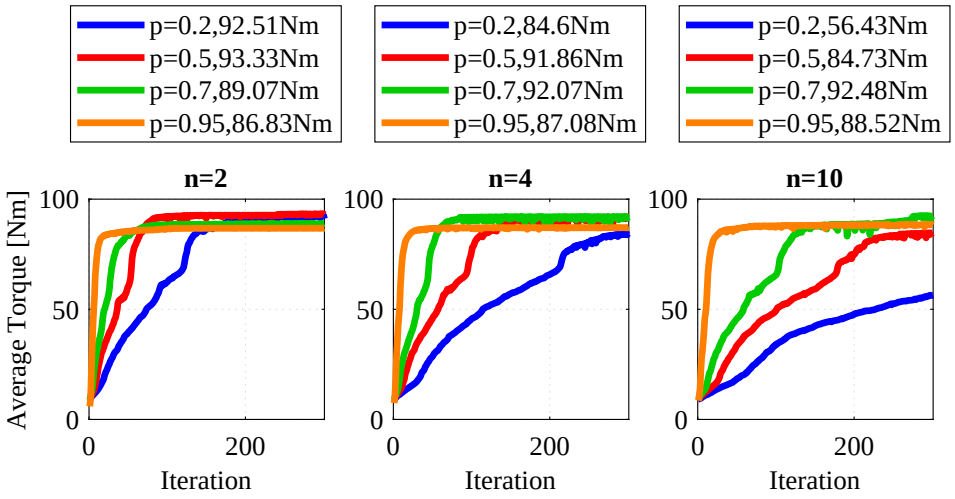


Figure 3.14: Results of optimizations with different penalization coefficients and initial density.

3.3.4 Effect of Torque Ripple Minimization

The optimization of torque ripple is generally more challenging than optimizing average torque alone, as a smooth torque waveform corresponds to a smooth flux distribution in the air-gap for a number of positions. Moreover taking into account the evolution of average torque from previous optimization results, evaluation of torque ripple is also different since the average torque will start from a very low

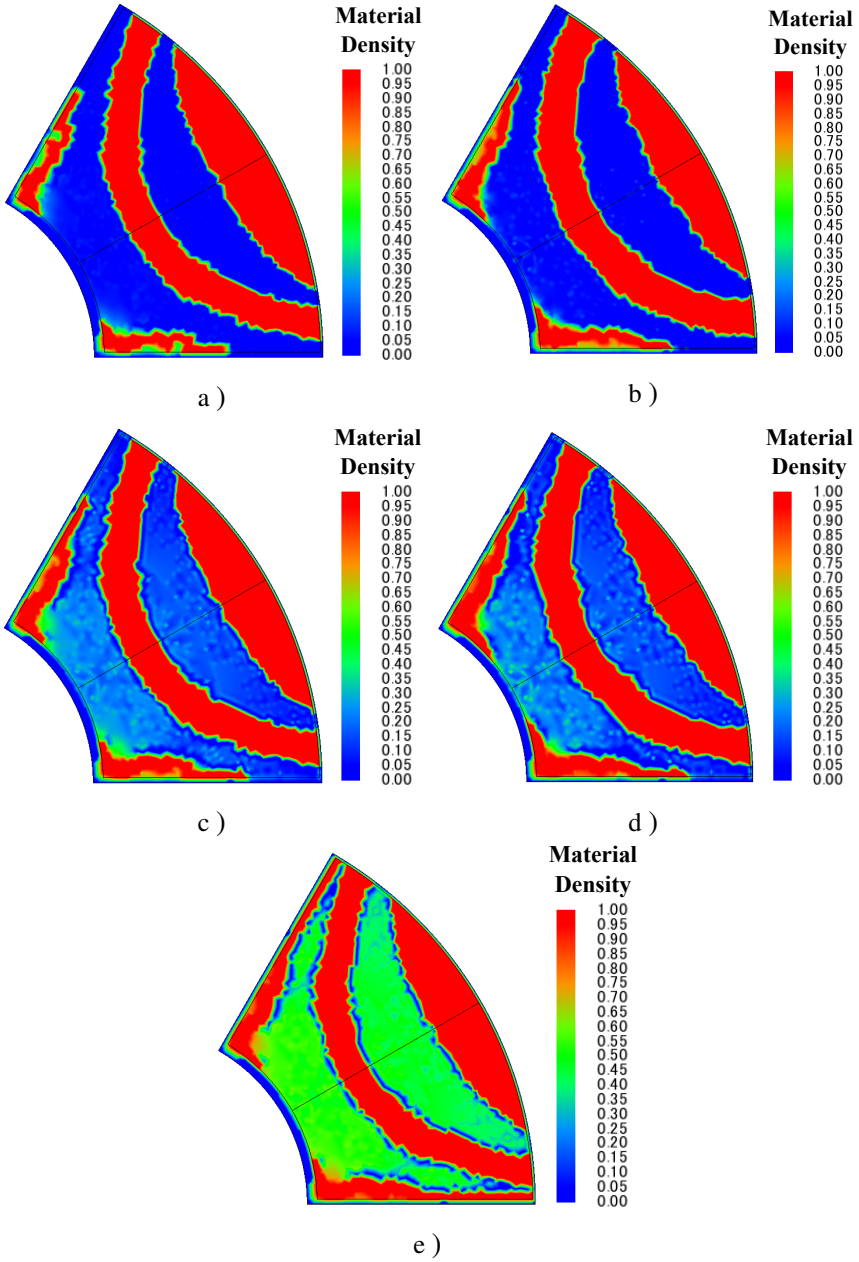


Figure 3.15: Material distributions for optimization results: a) n=2 p=0.2, b) n=2 p=0.5, c) n=4 p=0.5, d) $n = 4$ p=0.7, e) n=10 p=0.7

value and increase over time.

For this reason, number of iterations for this study is increased to 1000. A total of four optimizations are performed with 1 mm mesh model and one optimization with 2 mm model. For the 1 mm mesh model, penalization coefficients of 1, 1, 2 and 2 are used with initial densities 0.5, 0.9, 0.2 and 0.5 respectivelty. As for the 2mm mesh model penalization coefficient is 1 and initial density is 0.9. The best of both optimizations considered as the one with the highest average torque with the lowest ripple, are shown in Table 3.1 and Figure 3.16. One of the most important

Table 3.1: Optimization results with torque ripple objective.

Mesh	n	p	Average Torque [Nm]	Torque Ripple
1	1	0.5	90.08	7.25
1	1	0.9	92.1	6.3
1	2	0.2	84.4	6.3
1	2	0.5	95.17	2.2
2	1	0.9	92.3	4.6

outcomes of adding minimization of torque ripple as an objective is seen as the formation of additional air segments which were not existent in the previous results. For the designs with 1mm mesh and n=1, reduction of torque ripple is achieved by a cut-off like structure as shown in Figure 3.16 a) and b). Material distribution obtained with n=2 and p=0.2 seems to be umcomplete with the lowest average torque compared to others. However starting with n=2 and p=0.5, a clear two barrier structure with an additional cut-off like empty space is obtained and the highest torque is obtained with these settings as 95.17 Nm. For the 2mm mesh model, flux flow is distributed into the rotor from three different points. This is similar to a three flux barrier SynRel design obtained through a parametric optimization. Evidently, the most feasible design seems to be the one obtained with 2mm mesh model, though the non-existence of a feasibility objective prevents to comment on this aspect as the aim is not obtaining a robust structure.

3.4 Optimization Starting from a Non-Empty Design Space

In the previous section, various optimization settings are addressed starting from an empty design space. The aim in this part, is to find answer to the question: can a traditionally optimized geometry be refined through TO?

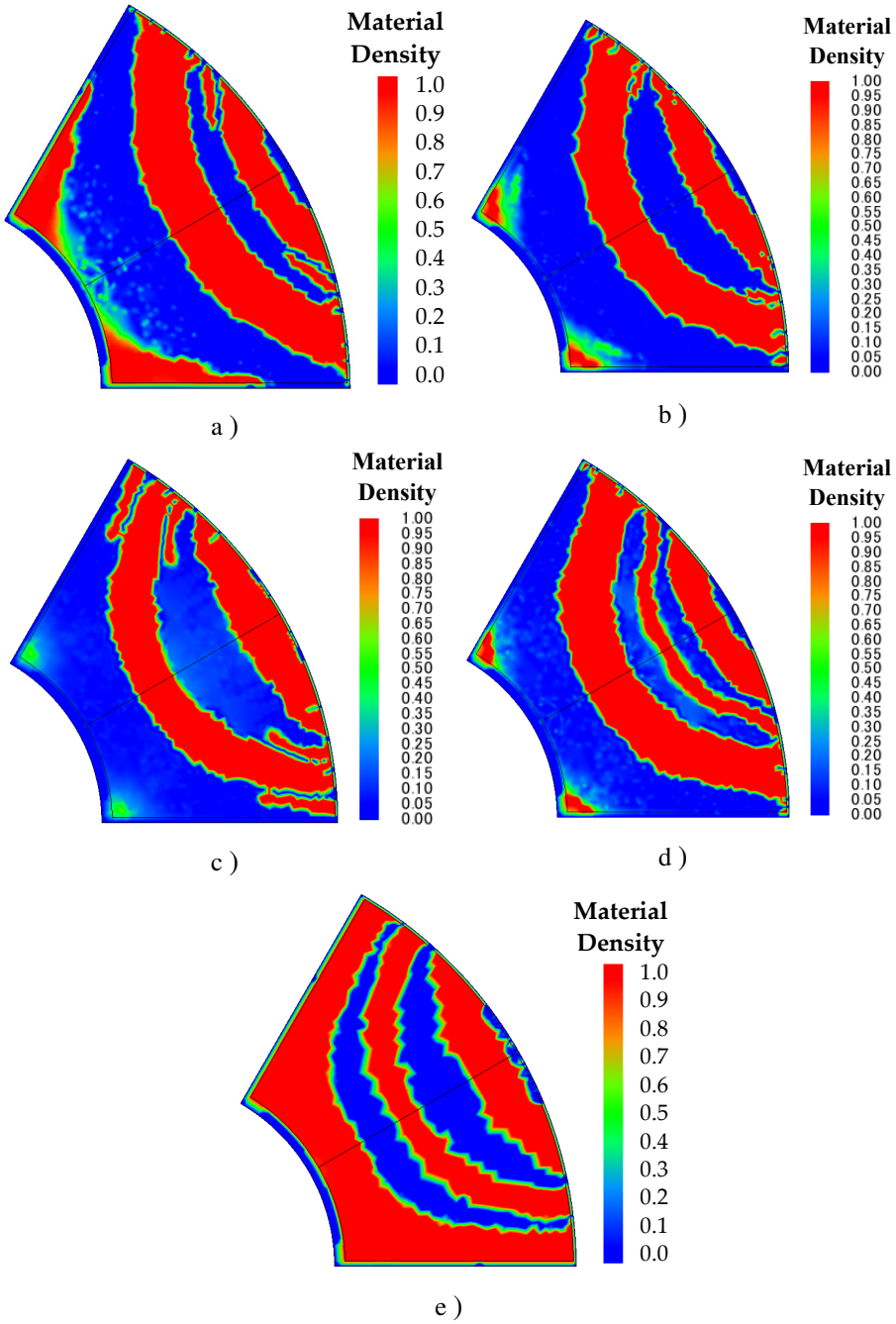


Figure 3.16: Results of torque ripple minimization for 1mm mesh model: a) n ==1, p=0.9, b) n=1, p=0.5, c) n=2, p=0.2, d) n=2, p=0.5 and 2mm mesh model: e) n=1, p=0.9.

For this purpose, the rotor of the benchmark machine is used with its three flux barrier optimized geometry (shown in Figure 3.6). An important point is that, the flux barriers of the benchmark machine is fixed meaning that TO will directly add onto it. A single objective of average torque maximization is considered and the maximum number of iterations are limited to 300. A total of six optimizations are performed with lower and higher meshes with different penalization factors and initial densities. These, along with results are presented in Table 3.2. As it was the case

Table 3.2: Optimization results starting from an already optimized design space.

Mesh	n	p	Average Torque [Nm]	Torque Ripple
low	1	0.5	101.62	11.84
low	1	0.9	102.08	7.46
low	2	0.2	95.79	28.84
low	2	0.5	99.02	20.00
high	1	0.9	102.3	6.5
high	2	0.5	91.7	30.00
Parametric optimization, Average Torque= 100.8Nm, Torque Ripple= 7.3 %				

with previous optimization studies once again it is seen that effect of optimization settings are subject to the optimization problem. Specifically when n=2 results are unsatisfactory. The reasons for such results can be identified by examination of material distributions shown in Figure 3.17. With the designs with n=2 it is observed that the shape of middle and innermost barriers are greatly changed. Additionally the end-point area of outermost and middle barriers are also much thicker than the original case which caused torque ripple to increase. Also in the case of using finer mesh when n=2 and p=0.5 the innermost segment is completely eliminated.

On the contrary, in all the designs where n=1 an improvement in terms of average torque is obtained. The most improvement is obtained when n=1 and p=0.9. In this case average torque is increased by 1.5 % and torque ripple is reduced to 6.5 %. It can be clearly seen that the outermost and middle barriers have only minor changes in the shape while the innermost barrier is enlarged towards the shaft. This increase in the total ratio of air to iron thickness in the rotor is the reason for the torque increase due to better exploitation of soft magnetic material. As a result, a minor performance increment is obtained by applying TO as refinement tool. The underlying significance of this change in the performance is the fact that when using the parametric expression of the geometry, it is not possible to achieve such a shape, unless certain modifications are made to increase the geometrical de-

grees of freedom. Interestingly, this newly obtained shape somehow resembles the optimization result obtained with spline parametrization as shown in Figure 2.11.

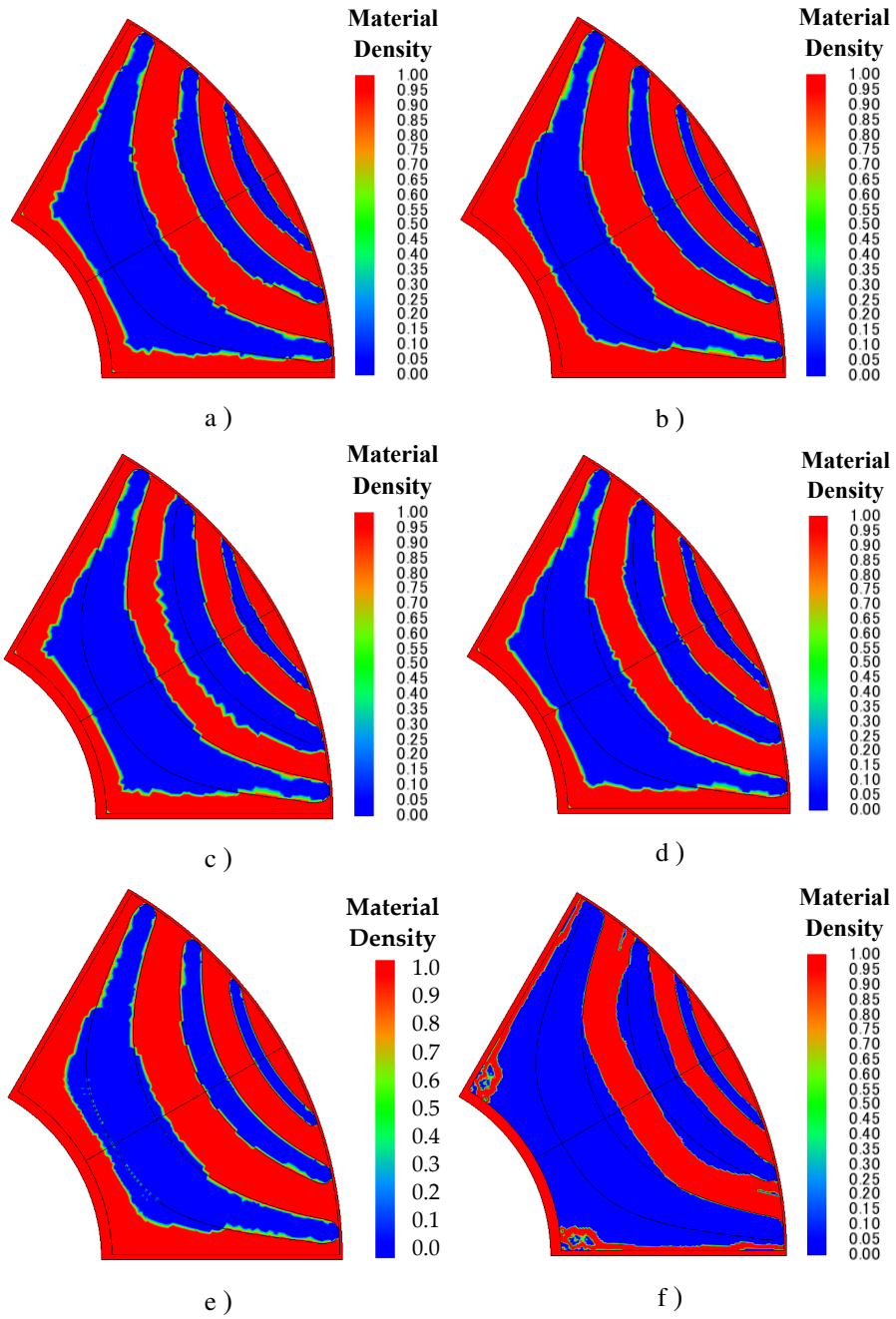


Figure 3.17: Material distribution of optimization results starting from an already optimized geometry, low mesh: a) n=1, p=0.5 b) n=1, p=0.9, c) n=2, p=0.2 d) n=2, p=0.5; high mesh: e) n=1, p=0.9, f) n=2, p=0.5.

3.5 Conclusion

After going into the details of geometric design and optimization through parametrization of flux barriers in chapter 2, in this chapter design possibilities using a completely different approach is employed. Using one of the TO methods, i.e DM, design possibilities are investigated. The work on TO starts with a detailed literature view on TO and its evolution throughout the years. Focusing on On/Off method and DM, the previous work applied to electromagnetic devices with a focus on electric machines are reviewed. Due to the fast convergence nature of the DM, it is selected to be used in this study considering also its availability as a tool. Using DM, but also in the general TO approach, final results are shaped by the optimization settings as they are actually the only variables to adjust. These settings, namely discretization of design space, properties of material interpolation and objective functions are studied on to understand their effect and possible benefits.

To start with, effect of mesh on the final material distribution are investigated. It is found out that by increasing the design space resolution it is possible to obtain better designs at the cost of increased computation time. Obviously this is prone to change based on the target device and even better results can be obtained with a finer mesh regarding a different machine or electromagnetic device. Other optimization variables, initial density and penalization factor are then looked into as they are two major internal settings of the DM based TO. Since there is a strong dependency of initial density to penalization coefficient, they have to be evaluated together. Results show that high values of penalization coefficients are harder to control due to their exponentially increasing steepness and moreover they tend to increase intermediate materials. Best cases are obtained with values up to 4 or 5. For the initial material properties of the design space, though varies with the penalization coefficient, it seems that around 0.5 is a good choice. Particularly for higher penalization coefficients, starting with a high value of initial density (close to 1) leads to poor results which is a cause of material properties being too close to iron.

A major change in the results are obtained when minimization of torque ripple is added as an objective function. Compared with the cases when it was not considered, inclusion of this objective lead to structures resembling multiple flux barriers.

It is an important realization that, none of the optimizations starting from an empty design space resulted better than a parametrically optimized geometry. However, formation of barrier-like structures starting from an empty design space is quite valuable.

As a last remark, design possibilities starting from an already optimized design space is investigated. This is achieved by using a parametrically optimized geometry which was previously obtained in chapter 2. The outcome of this examination is quite positive, as some minor improvements are obtained compared to the initial design.

Finally, it has to be underlined that, almost all optimizations starting with an empty design space produced unfeasible structures. The aim of the optimizations were to investigate individual effects of optimization settings and to possibly obtain non-conventional shapes which were not possible by means of geometric shape design, however it is an important point to realize that mechanical aspects have to be considered when TO is used.

3.5.1 Possible Future Work and Improvements

Some possible future work are summarized as below:

1. A more sophisticated optimization algorithm can be employed to handle difficulties encountered during TO.

2. Results obtained by TO can be enhanced and more feasible structures can be obtained by taking mechanical aspects into account.

3. A design space starting from a randomly distributed initial density might be a good idea to investigate. By doing so there is a good chance that more of the design space is utilized effectively.

4. Although only rotor of a SynRel motor is considered in this work, design of an IPM or PMaSynRel structure could be interesting. Flux guides that are normally geometrically parametrized can be formed through DM.

Chapter 4

Magnetic Equivalent Circuit Modelling

This chapter focuses on analysis of electric machines by means of MEC. Starting with the literature view, an overview of the current state of art and motivation is explained. After that, the modelling principles of a network type MEC will be given. Comparative study will then be presented between results obtained by FEM and MEC to show capabilities of the MEC.

4.1 Introduction

Design and analysis of electromagnetic devices, in particular electric machines, constitutes a complex and nonlinear problem where FEM is primarily used as an analysis tool. Typically, an analysis using FEM is composed of pre-prossessing, solving and post-processing. During these processes, first of all definition of geometry, materials and excitations are done and then solution takes place. Later in the post-processing stage all required quantities are calculated thus an analysis can be said, completed. However, in order to complete an electric machine design, a number of analyses need to be conducted with the aim of finding the most suitable design with respect to target application. The number of required analyses depend on the application and its complexity. For example, traction applications are rather tangled due to their performance requirements for more than one operating condition. Therefore, it is required to have more than one analysis for each motor design to compute its performance. As a consequence, time spent on each design candidate

becomes a critical parameter. Computation time of FEM based design processes can become prohibitive when such demanding applications are of interest. For this reason, designers and researchers conducted considerable amount of studies to seek for alternate methods throughout the years. One of the outcomes of these work is the equivalent circuit approach where magnetic quantities are represented with their electric counterparts in an electric circuit. A very simple representation is shown in Figure 4.1 where resistance, current and voltage are replaced by reluctance, flux and MMF.

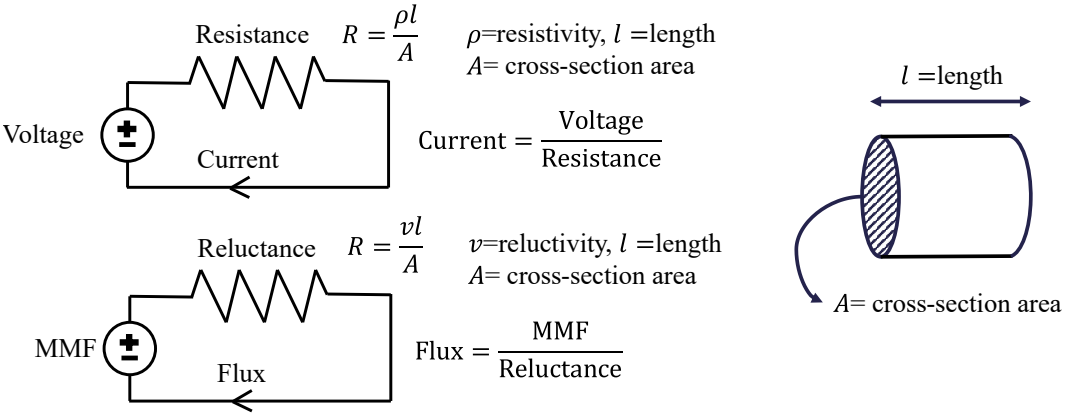


Figure 4.1: Magnetic to electric circuit anology.

Historic development of MEC modelling of electromagnetic systems date back to late 1960s where the main principles were presented [57] [58]. In these work the usage of already applied electric circuit analogy is extended for more complex magnetic structures such as multi-excited systems having magnetic linking to each other. One of the first academic works using MEC to model electric machines is known to be [59]. In this work, equivalent circuit representations for transformer, IM and a salient-pole synchronous machine are presented where non-linearity and rotation are taken into account while analyzing the circuits. In [60] an IM machine is analyzed both in terms of transient and steady-state performances. Later, the same author presented a simplified and faster version in [61]. The MEC as presented in [60] is given in Figure 4.2. It is seen that, reluctances accounting for different parts of the geometry is used, meaning that the MEC can also be utilized for design purposes. In 1990, another work for MEC is presented for analysis of synchronous machines which is also capable of including saturation [62].

A simple MEC, also called lumped parameter model, has been presented [63] to model hybrid stepper motors where both coil and PM excitations are used.

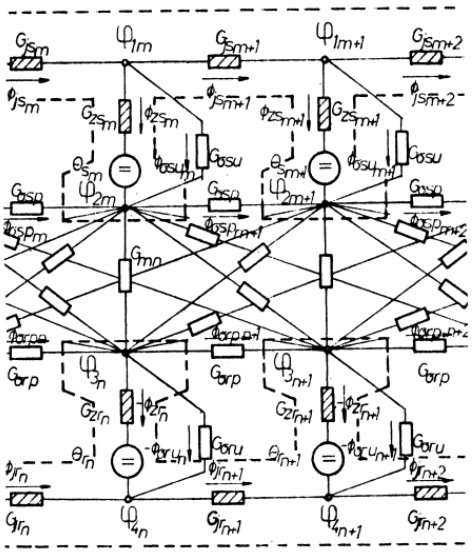


Figure 4.2: MEC of an induction machine as presented in [60] - shaded reluctances indicate saturable elements.

The proposed model is also experimentally verified in this study. Although generally built in 2D there are also some early studies considering 3D MEC structures. One of such work is presented in [64]. A relatively detailed equivalent circuit structure is used to model a permanent magnet linear synchronous motor (PMLSM). Geometry is divided into a number of hexahedron elements connected to each other by their centroiods. Authors do not mention the number of elements used in the study however from Figure 4.3 it is almost clear that for each hexahedron element 6 reluctances are used which should lead to high number of equations to be solved for. The results are later compared with those obtained with experiments and good match in terms of forces is obtained.

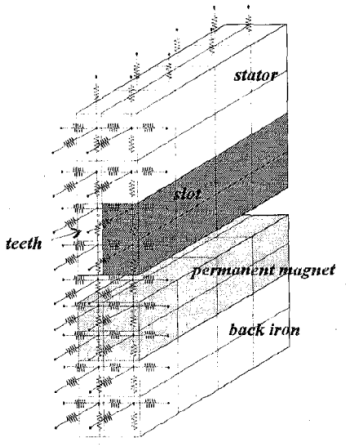


Figure 4.3: 3D MEC structure of a PMLSM as presented in [64].

Another paper published at late 1990s, uses MEC to model an SPM motor [65]. Different types of elements enabling uni-directional and bi-directional flux flow are used in the MEC structure as shown in Figure 4.4. The importance of using bi-directional elements can not be overstated enough as the direction of flux flow is unknown before solving the system. Whereas in case of uni-directional elements flux paths are strictly pre-defined and causes accuracy of such models to decrease or limit their usages.

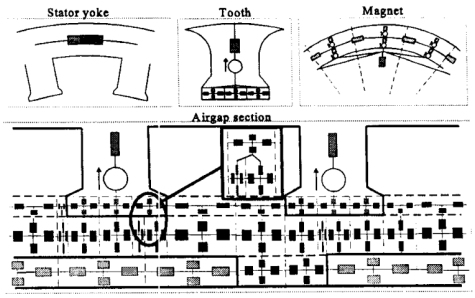


Figure 4.4: MEC used to model SPM motor as presented in [65].

In the aim of applying MEC technique with a direct saturation model, a switched reluctance motor (SRM) is analyzed in [66]. Authors make use of field distributions obtained with FEM to create two different equivalent circuits for aligned and un-aligned positions of SRM. Gauss-Sidel method is adopted to iteratively calculate saturation. Comparison between MEC analysis, FEA and experimental results yields small discrepancy when characteristic waveforms and values are considered.

In [67] authors create a very simple MEC structure to model an IPM machine. Although simplistic approaches do not generally favour accuracy, in this case direct prediction of d and q axis flux paths thus inductances, lead to good match between FEA and MEC analysis.

An SPM type brushless direct current (BLDC) motor is analyzed in [68] using a 3D MEC. The purpose of this study is to investigate symmetrical and asymmetrical rotor overhang effect which can only be done by means of 3D analysis. Despite the fact that nonlinear saturation is not mentioned throughout the study experimental comparison confirms results obtained by 3D MEC. Same authors later used genetic algorithm (GA) coupled with 3D MEC to conduct an optimization aiming to reduce cogging torque and increase average torque [69]. Experimental

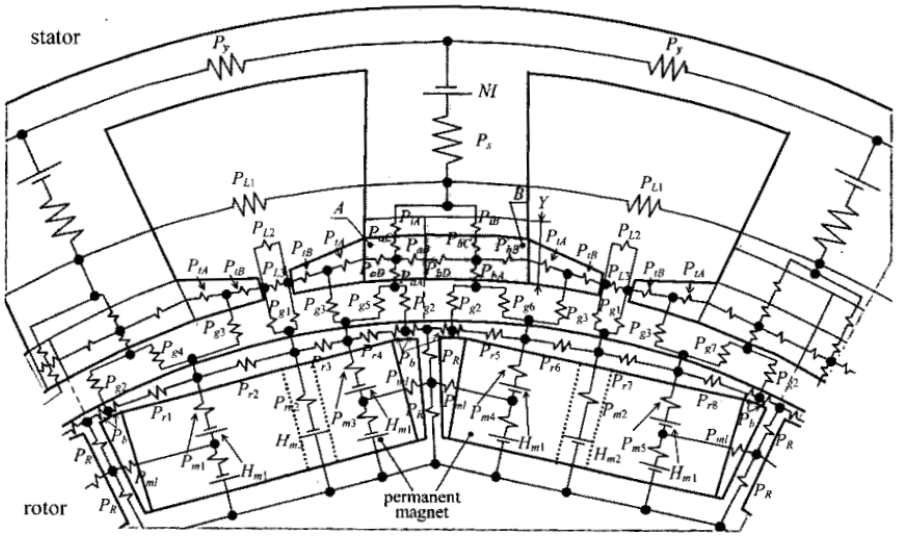


Figure 4.5: MEC used to model an IPM machine specifically focusing on local saturation as presented in [70].

results for initial and optimized designs are compared with results obtained by 3D MEC and only a small mismatch is found.

An IPM machine with inset magnets have been analyzed with a MEC structure in [70]. Authors use concentrated reluctances around PMs and stator tooth tips to capture the effect of local saturations. Effect of saturation is indeed important through all parts of the machine however specifically for IPM machines, non-linear behaviour in these regions affect the main flux paths hence determines the performance. The overall structure of the MEC is shown in Figure 4.5. Computation time for MEC model and FEM model is also compared and MEC analysis is approximately 24 times faster than FEA as given by authors. Later the MEC model is used for design purposes via GA, aiming to reduce motor volume. Same authors later in 2005 [71], applied a similar MEC with stator tip regions described by saturable reluctances, this time to an SPM machine. They use an exponential iteration scheme to update permeability.

A flux-switching machine is analzyed using a MEC [72], considering 6 different MEC structures to account for different positions of the rotor. These 6 MECs are obtained based on the rotation and change of flux distributions in the machine. Saturation is also taken into account iteratively, though exact method remains to be unknown.

A PMLSM is analyzed in [73] taking into account of saturation. Authors use a rather simple equivalent circuit structure in the study and they enhance it

by making use of an airgap distribution function based on position of PMs and stator tooth tips. Using such a function helps to obtain more accurate flux density distribution in the airgap as the MEC model is able to only compute flux density at certain points depending on the discretization of reluctance elements.

It is known that IMs have been one of the main focus of alternative modelling techniques, mainly due to its high computational burden required to simulate the transient behaviour. In this regard, authors in [74] present one of the most complete methodologies for MEC modelling of IMs. Description of stator windings, different parts of the stator, rotor and rotor currents are well identified considering the saturation with Gauss-Siedel method. Lastly, experimental measurements are compared and discussed.

Another 3D MEC presented in [75] analyzes axial flux PM machine. As similar in other MEC structures, reluctance elements accounting for leakage parts are separately placed and their values are separately calculated. Results are compared with 3D FEA and good accuracy is obtained with much less computation time.

Another research focusing on MECs, models IPM machines with moving airgap and cross-coupling effects [76]. The MEC structure seems to be built mostly focusing on the rotor to obtain the performance which is highly dependent on saturation. The rotor reluctances are shaped according to the IPM motor topology as shown in Figure 4.6. Stator reluctances are quite uniform as each tooth and each yoke part between teeth are modeled by one reluctance each. MMF sources are placed and their values are calculated based on the current and winding matrix made of 0s and 1s for each slot per phase.

Until now, MEC models that are specifically focusing on certain motor topologies are reviewed. Based on these previous works and others which have not been included, it can be said that a general MEC model is yet to be built. The importance of this is that, in order to analyze different motor topologies different MEC structures have to be built. Additionally, flux paths are mostly predefined, reducing the accuracy of the models. Other aspects include the ambiguity of the non-linear material saturation and rotation due to the lack of clear explanations.

Lately, more systematic and detailed MEC structures were presented in the literature. One of the first examples, uses uniform network of reluctances (with

bi-directional elements similar to those in [65]) in a similar fashion to mesh elements used in FEM [77]. Although this structure has been only applied to a PMLSM, it is possible to talk about a generic model as reluctances have been uniformly generated to fill the design space.

In a similar structure, an axial flux SPM type machine has been modelled by using a number of 2D MEC structures and using them as radial slices [78]. Loop current method (also referred as mesh current method) is used to solve circuits. For the non-linear saturation, Newton-Raphson method is used and matching results are obtained when 3D FEA results are compared. Besides, computation time is greatly reduced (from 15 hours with 3D FEA to 3 seconds with MEC).

Node voltage method is used to solve for the circuit structure presented in [79] to analyze a flux switching machine. Non-linear material characteristics are accounted for by using fixed-point iteration and Newton-Raphson method together.

A SRM is modelled by using a uniform reluctance network structure in [80] also utilizing Newton-Raphson method. Authors later apply the same technique to build a dynamic machine model to obtain radial forces [81].

Lastly, in [82] three different machine types (IM, SynRel machine and IPM machines) are analyzed by making use of a similar structure. Authors use a simple iteration scheme similar to interval halving method (bisection method) to

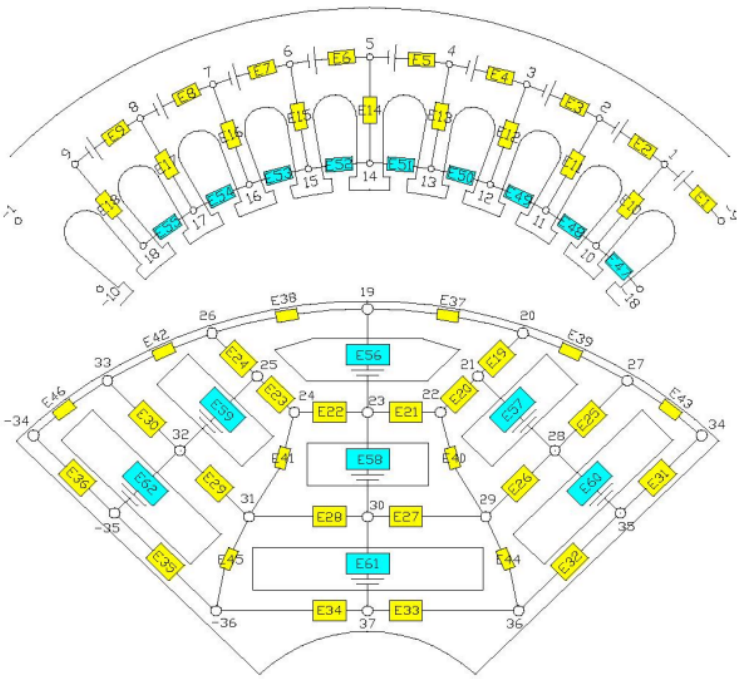


Figure 4.6: MEC model of an IPM machine as presented in [76].

account for non-linear saturation.

Even though these recent works on MEC provide a more general approach, the full capability of such equivalent circuit structures are not explored yet. For example, least periodicity conditions incorporating single pole symmetry (odd symmetry) is not presented in the literature. This is significantly important as it would be possible to increase the accuracy or reduce the computation time compared to the case where pole pair symmetry (even symmetry) is used. Other than that, the adaption of rotation (or linear motion) can be further eased without using a different method such as interpolation on the moving boundary as in [79] and airgap permeance function in [82].

In the MEC that will be described onwards, it is intended to provide a comprehensive approach about the general-purpose application of a highly accurate MEC. The aim is to build the basis for an alternative or supporting modelling technique to FEM in terms of accuracy with reduced computation time also addressing the previously mentioned shortcomings.

4.2 Description of the MEC

On a fundamental level, MEC as used in this work is a network composed of reluctances and MMF sources. The main building block of this network is a cell element (CE) and it describes a small part of the geometry. Typically it consists of two horizontal and two vertical reluctances. The reason for using four reluctances for a CE is to provide bi-directional flux flow and consequently increase the accuracy. A typical CE is shown in Figure 4.7 enclosed with dashed, red lines. Since it is a matter of preferred coordinate system, the words ”horizontal” and ”vertical” do correspond to ”tangential” and ”radial”. Based on the fact that rotating electric machines are of interest in this work, cylindrical coordinate expressions will be primarily used.

Apart from the standard CEs, there are boundary cell elements in the MEC. These CEs are only used on the boundaries, such as upper and lowermost parts to describe a rotating electric machine to impose a Dirichlet like boundary condition similar to FEM. In the MEC, the flux flow towards the outer edges of the magnetic structure is prevented by removing 1 of the radial reluctances. These

elements are shown with enclosed blue dashed lines in Figure 4.7. In the case of other type of magnetic systems similar approach can be used to tailor standard CEs to get boundary CEs.

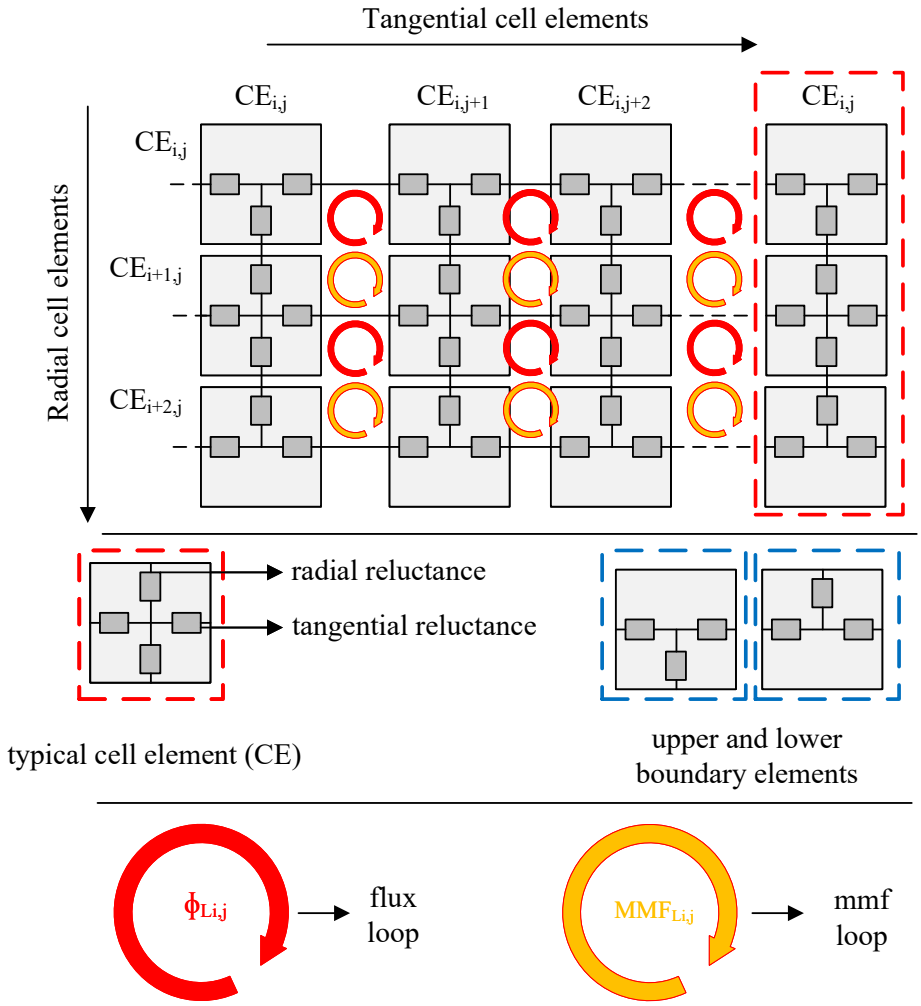


Figure 4.7: General structure of the MEC and different CEs.

A very simple MEC network with 3 radial and 3 tangential CEs is depicted in Figure 4.7. Indexing of the CEs are shown with subscripts (i, j) where i refers to the vertical position and j refers to the horizontal position. Indexing of the reluctances are done exactly in the same manner, separately for radial and tangential reluctances.

In terms of solution technique there are two alternatives: node voltage method and loop current method (mesh current method). Ideally both of them yield the same results however the formulations are different. If node voltage method is used, node potentials would be the unknown and if the loop method is used, loop

fluxes would be the unknown. Since they are not interchangable the solution technique of the circuit structure needs to be defined at an early stage. In [83] both methods are compared in linear and non-linear conditions and it is found out that in the linear conditions they perform the same. When non-linear convergence is analyzed using the Newton-Raphson method, loop method overperforms. The reason for different performances is due to numerical differences arising in Newton-Raphson iterations. Clearly, this is a comparison for a specific system considering only one iteration scheme and might not be generalized when other iteration algorithms are used. Anyway, since Newton-Raphson method is intended to use, loop method will be used in this work.

Using the loop method, loop fluxes needs to be solved for so that flux densities of reluctances can be obtained, therefore in each closed section formed between reluctances there is a flux loop. Additionally, in this study, MMF sources will also be defined in terms of loops. These are also shown in Figure 4.7. Flux loops (Φ_L) and MMF loops (MMF_L) are indexed in the same manner as CEs.

Total number of loops and reluctances can be calculated based on the number of radial CEs (n_R) and tangential CEs (n_T) as follows, n_L stands for number of total loops and n_{RE} stands for total number of reluctance elements:

$$n_L = (n_R - 1)n_T \tag{4.1}$$

$$n_{RE} = (2n_R - 2)n_T + 2n_T n_R \tag{4.2}$$

It is to be noted that that here calculation n_L and n_T are not generalized and depends on the structure of the MEC itself. For different magnetic systems, different boundary CEs would be used and these descriptions would not be valid.

4.2.1 Boundary Conditions

Similar to FEM, boundary conditions should be considered in the MEC to obtain correct solutions and fully benefit from magnetic periodicities.

Usually when analyzing a radial flux electric machine with the 2D FEM, upper and lower boundary lines are defined as Dirichlet boundary and zero flux condition is applied on those so that flux flow is not perpendicular to them and field

solution is confined in the target geometry. As previously mentioned, in the case of MEC this is handled by making a change to a standart CE with 2 radial and 2 tangential reluctances. According to the magnetic system, one of the radial or tangential reluctances can be removed in order to restrict flux flow further in that direction. In this case, this is achieved by removing a radial reluctance as shown in Figure 4.7.

The other type of boundary that needs to be applied is to simply utilize periodicity where it is possible. In integer slot machines, number of slots is an integer multiple of number of poles, which makes it possible to analyze only a fraction of the whole structure and then multiply it with the integer multiple. Of course excitations do also need to be periodic (recurring) if this is desired to be used.

Periodic boundary condition is further divided into even and odd-periodic conditions. In the even-periodic condition, the geometry needs to be complete in terms of excitations and geometry. An example of this condition would be a geometry analyzed with a pole pair. In the odd-periodicity case, a single pole is sufficient beacuse the unmodelled pole is reflected back to the model at the joining boundaries. The differences in periodic boundaries are shown in Figure 4.8, showing the model varieties of a full model, even-periodic model and odd-periodic model. By using the odd-periodicity it is therefore possible to analyze only a portion of the geometry reducing the computation time or using the same number of mesh elements, increase the accuracy.

When analyzing rotating machines (circular structure), in order to use one of the mentioned periodic conditions, the CEs on one side (thus reluctances) need to be connected to the CEs on the other side to ensure continuation of flux flow. With this condition, a full model or an even-periodic model can be analyzed without any need for modification. To be able to use odd-periodic model, this connection is also required but the unmodelled part's flux needs to be reflected by virtual connections which will later be explained in detail.

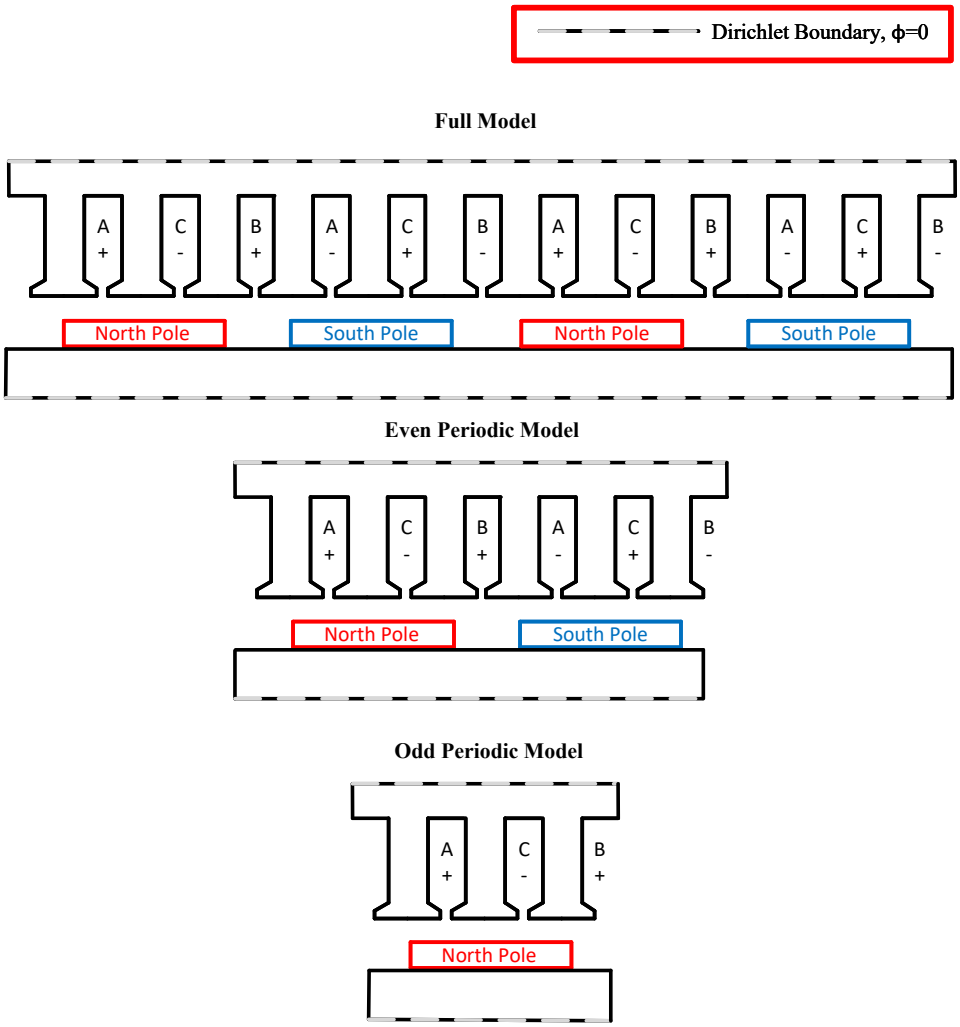


Figure 4.8: General structure of the MEC and different CEs.

4.2.2 Discretization and Definition of Machine Geometry

As defined and explained previously, MEC is made up of tangential and radial CEs. The number of these CEs define the discretization and so the ability to reprent a geometry and its model complexity. This is practically similar to use of mesh in FEM. The higher the number of total CEs, higher the accuracy but increased computation time.

A very simple geometry and its description is first shown for clarity and then an actual motor geometry will be shown. If the simple geometry of Figure 4.9 is examined, the geometry definition can be completed with the following steps:

1. The number of CEs defining the MEC needs to be defined previously. In this case for demonstration purposes a simple 4x4 (4 vertical vs 4 horizontal)

MEC structure is selected.

2. Each CE's centroid is checked if it is or if it is not in the shapes.

3. This check gives either 1 or 0 for each CE and these values are stored in a matrice called Material Matrix (will be denoted as M) and total number of M is the same as total number of different materials.

To move on with a more complex geometry, a SynRel machine and its discretization is given in Figure 4.10. Even with a course mesh of 28x36, a good desciption of the geometry is achieved. Nonetheless, due to the shape of CEs being arc segments, a full match can not exist. A better approximation can be achieved by increasing the number of cells with the expense of increased computation time. The fact that there are no exact solutions for this issue suggest number of CEs should be determined with respect to the geometry. One of the easy approaches is to separately determined the number of elements to ensure the critical thicknesses are perfectly achieved. For example, in the example of Figure 4.10, the number of radial CEs in the rotor tangential ribs, stator tooth tip and in the airgap regions are made to match the exact thicknesses.

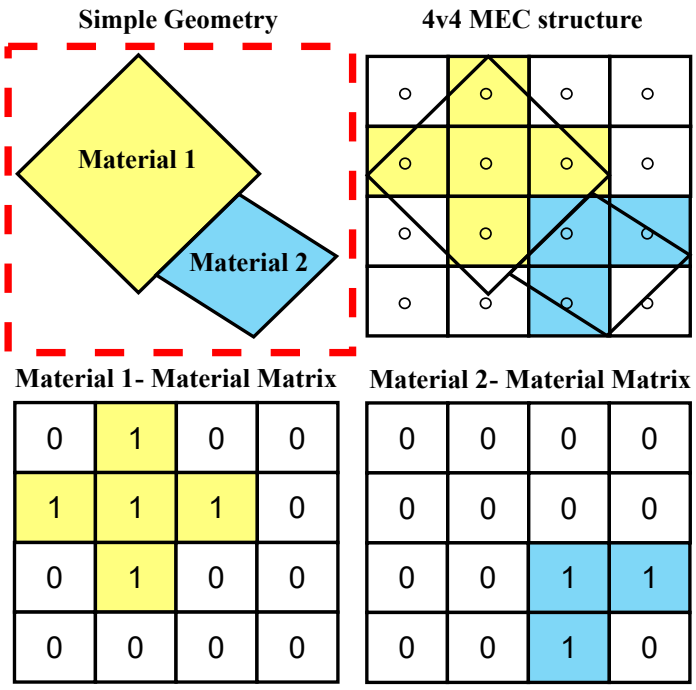


Figure 4.9: Simple example of geometry description.

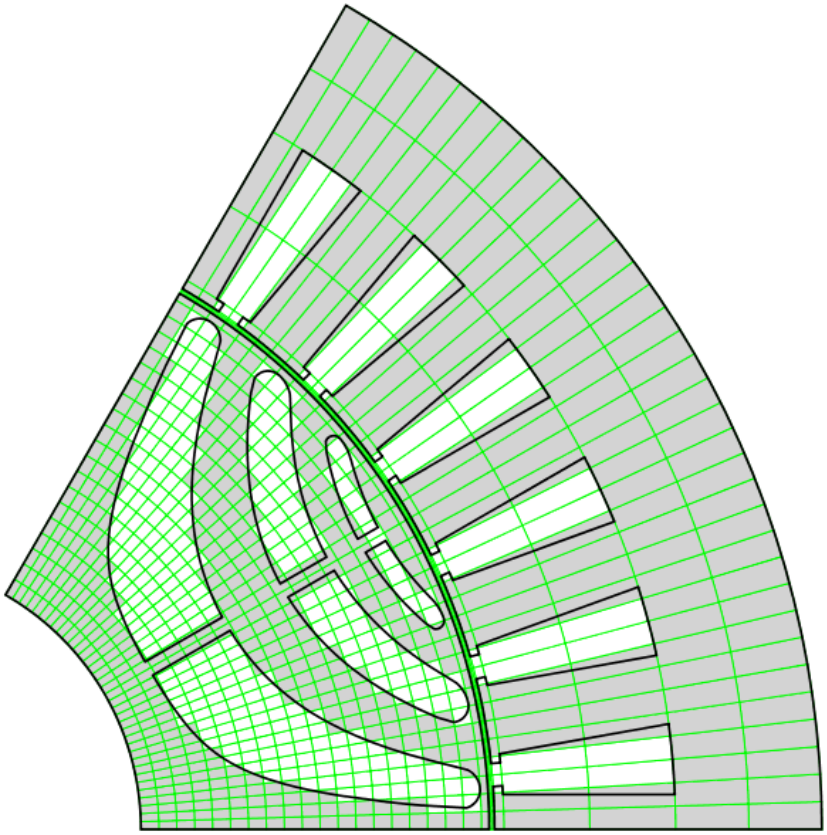


Figure 4.10: Geometry description of a SynRel machine on a 28v36 MEC.

4.2.3 Handling the Rotation

Rotation in the MECs are rather problematic as they can easily overcomplicate the whole procedure. Here a simplistic approach is followed to handle the rotating parts which can also be applied to any type of movement. The key here is to avoid any possible re-meshing or indexing that would cause an additional computation.

The method adopted here is to simply shift the material matrix in the preferred way of rotation. To visually exemplify, the example from Figure 4.9 is used and rotated in Figure 4.11. This way, at each rotation step only the material matrix is updated without the need for any additional change.

An important point that arises with this rotation method is the limitation of the rotor position. Since the number of columns in the material matrices are equal to the number of tangential CEs, with each shift minimum number of rotation angle is limited to the mechanical degree of the model to be analyzed divided to n_T.

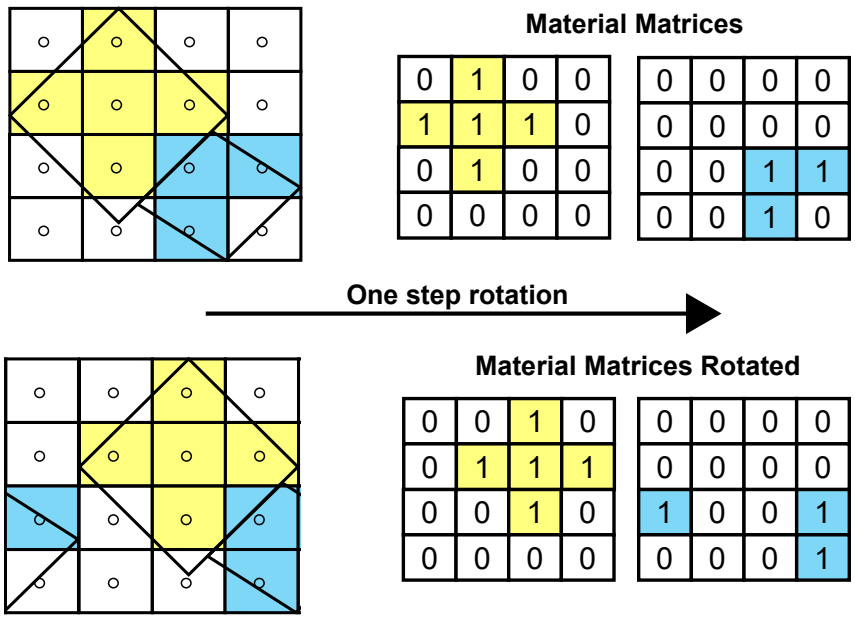


Figure 4.11: Simple example of rotation.

4.2.4 Calculation of the Reluctance Values

A general formula for the calculation of the reluctance assuming identical cross section is given as:

$$R = \frac{l}{A} v(B) \tag{4.3}$$

where l is the length of the assumed flux tube, A is the cross section area and $v(B)$ is the reluctivity as a function of the flux density. Since the assumed flux tube shape is circular, length and cross-section areas for radial and tangential elements has to be separately defined.

A simple illustration of the circular CE is given in Figure 4.12. In the figure, r_l and r_u stands for lower and upper arc radii. Thickness of an element in the radial direction is denoted as t and axial length (stack length) is given as l_{axial}. The angular span of a CE is described by θ.

The length and area of radial reluctances then can be defined using the following equations:

$$\text{length of radial reluctances, } l_r = \frac{r}{2} \tag{4.4}$$

$$\text{area of lower radial reluctances, } A_{lr} = \frac{2pi}{360} \left(r_l + \frac{t}{4}\right) \theta \; l_{axial} \tag{4.5}$$

$$\text{area of upper radial reluctances, } A_{ur} = \frac{2pi}{360} \left(r_l + \frac{3t}{4}\right) \theta \; l_{axial} \tag{4.6}$$

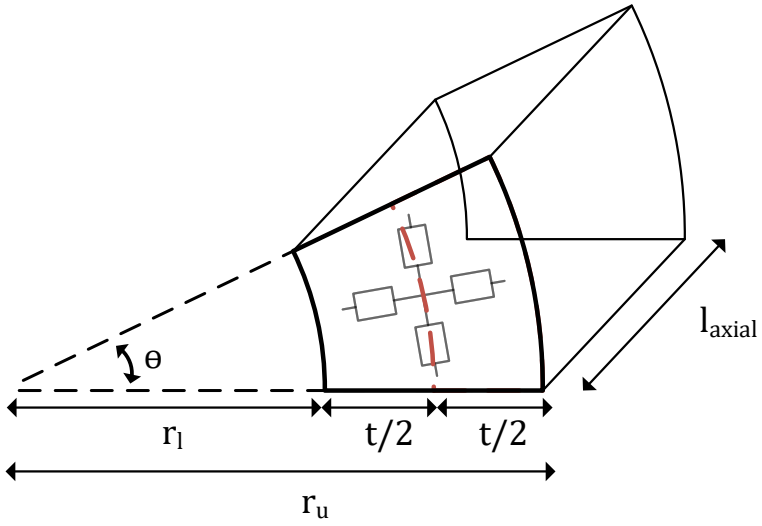


Figure 4.12: CE shape and reluctance dimensions.

Similarly for the tangential reluctances, length and area can be written as below:

$$\text{length of tangential reluctances, } l_t = \frac{2pi}{360}\,(r_l + \frac{t}{4})\,\theta \tag{4.7}$$

$$\text{area of tangential reluctances, } A_t = t\; l_{axial} \tag{4.8}$$

The quantities t and θ are directly depending on the discretization, namely n_R and n_T respectively. In this MEC structure, tangential CEs are distributed uniformly meaning that θ is the same for all CEs, however it can also be made non-uniform and in that case for different tangential positions CEs would have different θ values. For the thicknesses of CEs, a non-uniform distribution is used and this leads to different CEs having different thicknesses, thus varying r, for different radial positions. The reason behind using non-uniform radial thicknesses is to define some parts separately to perfectly fit their lengths. This is particularly beneficial for high saturation areas such as rotor tangential ribs and stator tooth tips.

4.2.5 MMF Definitions

MMF sources in electromagnetic systems exist due to current carrying conductors and permanent magnets. In the equivalent circuit modelling, both of these sources can be modelled by inserting voltage sources in the appropriate parts

of the circuit. In this work a slightly different approach is adapted by directly representing the MMFs as loop MMFs. This is advantageous due to two reasons. Firstly, placing the voltage sources can be problematic, leading to confusion, and second in the case where voltage source elements are used, eventually total MMF in every loop has be calculated and used in the loop matrix form for solution of the system in the loop method formulation.

4.2.5.1 MMF due to Windings

MMF of a winding (MMF_W) with N number of turns and current I can be expressed as:

$$\oint H\,dl = N.I = MMF \tag{4.9}$$

For the MEC, when a CE is a winding, its total MMF is divided equally between its shared loops. An exemplification is provided in Figure 4.13 with one and two CEs being windings where all CEs have the same surface area. In the Figure 4.13 (a) a single CE in a 3v3 MEC structure has a total MMF equal to MMF, and the surrounding loops do share this value equally, divided into 4. The other example, as depicted in Figure 4.13 (b), portrays two sets of windings that collectively generate a total MMF equivalent to MMF. Consequently, each individual winding yields an MMF value of $\frac{MMF}{2}$. In this scenario, the MMF of each coil in the set is initially distributed equally among the neighboring loops, resulting in an allocation of $\frac{MMF}{8}$ per loop. Moreover, if a particular loop accommodates multiple MMF contributions from distinct sources, these individual contributions are added together.

For a more realistic case, such us a slot area having multiple number of CEs holding certain number of turns and current flowing inside, each CE's MMF contribution has to be calculated with respect to their surface areas. This can be calculated by using Equation (4.10). Here MMF_{CE} is the contribution of a CE in the winding region, MMF_W is the total winding MMF and SA_{CE} is the individual surface area belonging to a CE in the winding region.

$$MMF_{CE} = \frac{MMF_W}{SA_W} \cdot SA_{CE} \tag{4.10}$$

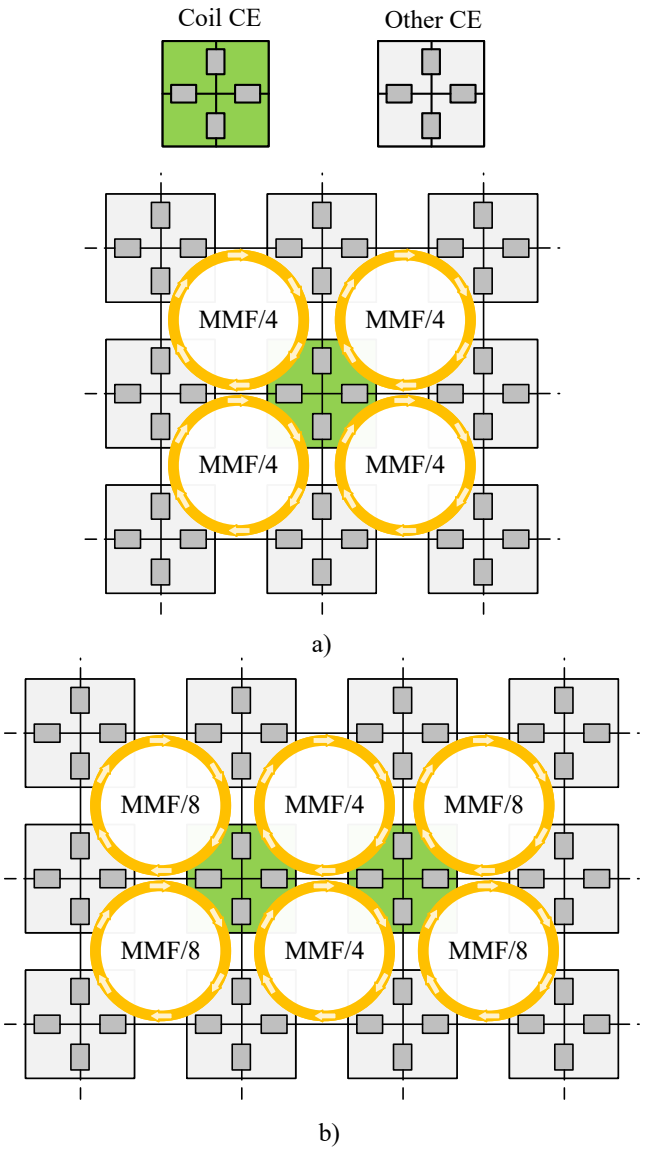


Figure 4.13: Example of a winding MMF

4.2.5.2 MMF due to PMs

MMFs belonging to PMs are defined in a similar way to those of windings. If a CE is of a PM material, MMF is again reflected, shared between the neighbouring loops. In the particular case of PMs, this distribution of MMF is not equal among the loops due to the magnetization direction of the PMs.

As discussed in [84], the MMF of a PM in linear operating conditions can be written as in Equation (4.11) where H_c is the coercivity of the magnet and l_{PM} is the length of the magnet in the magnetization direction.

$$MMF_{PM} = H_c \, l_{PM} \tag{4.11}$$

A single CE of PM is shown in Figure 4.14 in a 3x3 MEC structure. Neighbouring loops around the PM CE is numbered from $\text{MMF}_{\text{PM-1}}$ to $\text{MMF}_{\text{PM-4}}$. Collective MMF in each of these loops can be written as:

$$MMF_{PM-1} = \frac{1}{2}[+H_c l_t cos(\alpha) + H_c l_r sin(\alpha)] \tag{4.12}$$

$$MMF_{PM-2} = \frac{1}{2}[+H_c l_t cos(\alpha) - H_c l_r sin(\alpha)] \tag{4.13}$$

$$MMF_{PM-3} = \frac{1}{2}[-H_c l_t cos(\alpha) - H_c l_r sin(\alpha)] \tag{4.14}$$

$$MMF_{PM-4} = \frac{1}{2}[-H_c l_t cos(\alpha) + H_c l_r sin(\alpha)] \tag{4.15}$$

In Equation (4.12), the aim is to distribute MMF of the PM in the loops both in terms of radial and tangential flux contributions depending on the magnetization direction α. It is important to note that α here is not the global magnetization direction and has to be calculated for each PM CE. For example, setting $\alpha = 90^o$ creates a radial magnetization as the lengths are calculated in cylindrical coordinates.

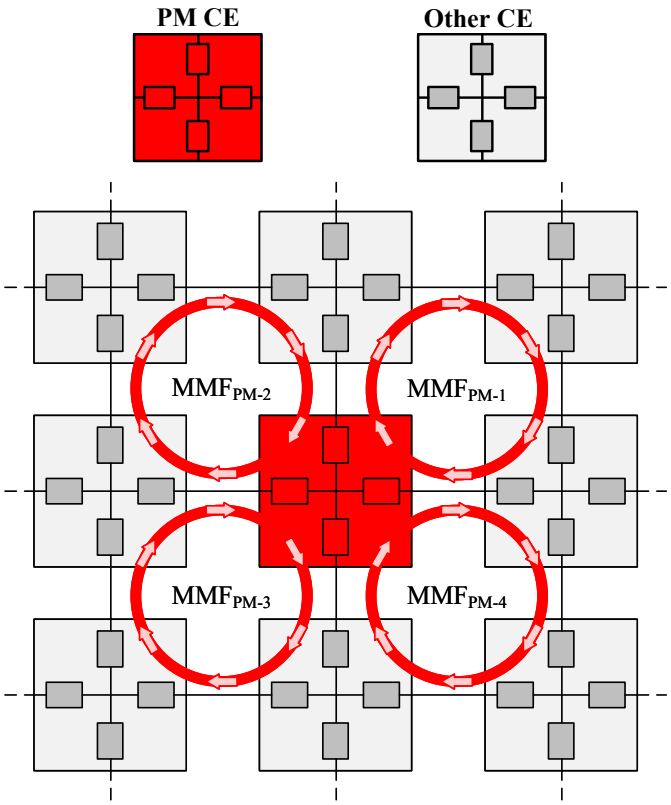


Figure 4.14: Example of a winding MMF

4.3 Solution Technique

As previously mentioned, loop method is the main formulation of the MEC and hence loop fluxes ϕ_L are the unknowns. In order to solve for the flux, normally the following equation is used:

$$\phi = \frac{\text{MMF}}{R} \tag{4.16}$$

However with this equation only a single reluctance or an equivalent smaller circuit structure can be solved. For complicated circuits having a number of loops, a system of equations have to be formed and solved using matrix operations in the form of Equation (4.17).

$$R_L^{-1}\ \text{MMF}_L = \phi_L \tag{4.17}$$

The Equation (4.17) comes from the loop current solution approach. When the equations for all of the loops are written, reluctances and fluxes are seperated and then written in the matrix form to solve the system of linear equations.

Evidently, R_L, ϕ_L and MMF_L are the loop quantities. Although previously shown with two indexes (i, j), ϕ_L and MMF_L are used as single column vectors of size [n_L x 1] due to matrix operations. Conversion of matrix sizes are done column wise and will be underlined through the thesis when needed.

4.3.1 Building the Loop Reluctance Matrix R_L

Forming the matrices ϕ_L and MMF_L are straightforward using the definitions in the previous chapter. On the other hand, forming the matrix R_L requires a different approach. Basically, R_L is the matrix containing the reluctance values of different loops and its size is [n_L x n_L]. Diagonal elements of R_L can be found by the summation of all reluctances in a loop. This is universal for any kind of MEC structure and independent of any other property. The other elements of R_L shows the reluctance values shared by other loops. These elements, unlike the diagonal ones, are unique to the structure of the CEs and MEC.

Considering a 3x3 simple MEC structure as shown in Figure 4.15, R_L will be formed as an example. In the figure all loops are numbered in two ways, both in linear and matrix indexes. If it is assumed that all of the reluctances do have a value

of 1, R_L can be written as:

$$R_L = \begin{array}{c} \\ \text{Loops} \downarrow \end{array} \begin{array}{c} \text{Loops} \rightarrow \\ \begin{bmatrix} 8 & -2 & -2 & -2 & 0 & 0 \\ -2 & 8 & -2 & 0 & -2 & 0 \\ -2 & -2 & 8 & -2 & 0 & -2 \\ -2 & 0 & 0 & 8 & -2 & -2 \\ 0 & -2 & 0 & -2 & 8 & -2 \\ 0 & 0 & -2 & -2 & -2 & 8 \end{bmatrix} \end{array}$$

All diagonal elements (i, j) where $i = j$ of matrix R_L are the sum of all reluctances in the loop. Since there are a total 4 radial and 4 tangential reluctances in each loop, each diagonal entry is equal to 8. Then, other elements need to be filled. For the first loop ($L_{1,1} = L_1$), the other loops in connection are ($L_{1,2} = L_2$), ($L_{1,3} = L_3$) and ($L_{2,1} = L_4$) meaning that in R_L's first row and first column, 2^{nd} , 3^{rd} and 4^{th} elements are nonzero. Since the first loop shares 2 radial elements with the second loop, and since the relative direction of the second loop to the first loop is opposite, these elements attain a value of -2. Similarly, ($L_{1,2} = L_2$) has connections on its left, right and down sides with elements ($L_{1,1} = L_1$), ($L_{1,3} = L_3$) and ($L_{2,2} = L_5$). If any two loops are not connected then their position in the matrix becomes 0 (for example ($L_{1,1} = L_1$) and ($L_{2,3} = L_6$)).

Same procedure can be followed to calculate the other elements of R_L. In general, all the irregularities of connections arise due to the existence of boundary CEs, first and last column of CEs. Other than that loops in the middle parts all have 4 connections between the upper, left, right and bottom loops.

Of course, when the number of CEs are high there needs to be an automatic procedure to form R_L. One way to do it in coding environment is to use "for loops" with different conditions. Another way is to approach the problem in a different way and build R_L by using a seperate connection matrix. This "connection" matrix is called loop incidence matrix , L [78]. Loop incidence matrix is a matrix of size [n_{RE} x n_L] and it gives information about how a reluctance is associated with a loop.

The elements of L can be find by the following procedure:

- If a reluctance is in a loop and in the same way of loop direction, its element

in the matrix becomes 1.

- If a reluctance is in a loop but in the opposite way of loop direction, its element in the matrix becomes -1.
- If a reluctance is not associated with a loop its element in the matrix becomes 0.

Once the matrix L is formed, R_L can be obtained by Equation (4.18). Here **R** is the diagonal matrix including all of the tangential and radial reluctances. The placement of the reluctances in **R** starts with the tangential reluctances from left to right, continues with the radial reluctances from left to right and then repeats in the same order.

$$R_L = L^T \mathbf{R}\, L \tag{4.18}$$

4.3.1.1 Applying Odd Periodic Boundary Condition

Until here, the procedure to obtain matrix R_L is explained in detail, however this is for the case when an even periodic condition (pole pair symmetry) or the whole magnetic model is used. To use the odd pole periodicity, incidence matrix L needs to be built in a slightly different way. Since it is required to impose the flux of the unmodelled part, either the first or last loops should thought to be in the opposite direction to impose negative flux coming from the other pole.

To explain visually, a 4x4 MEC structure is illustrated as an example in Figure 4.16. In the Figure 4.16 (a) the even periodicity condition is shown as ex-

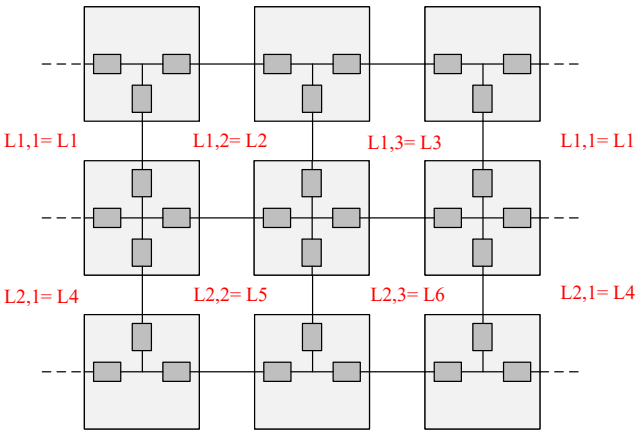


Figure 4.15: Simple example of 3v3 MEC structure

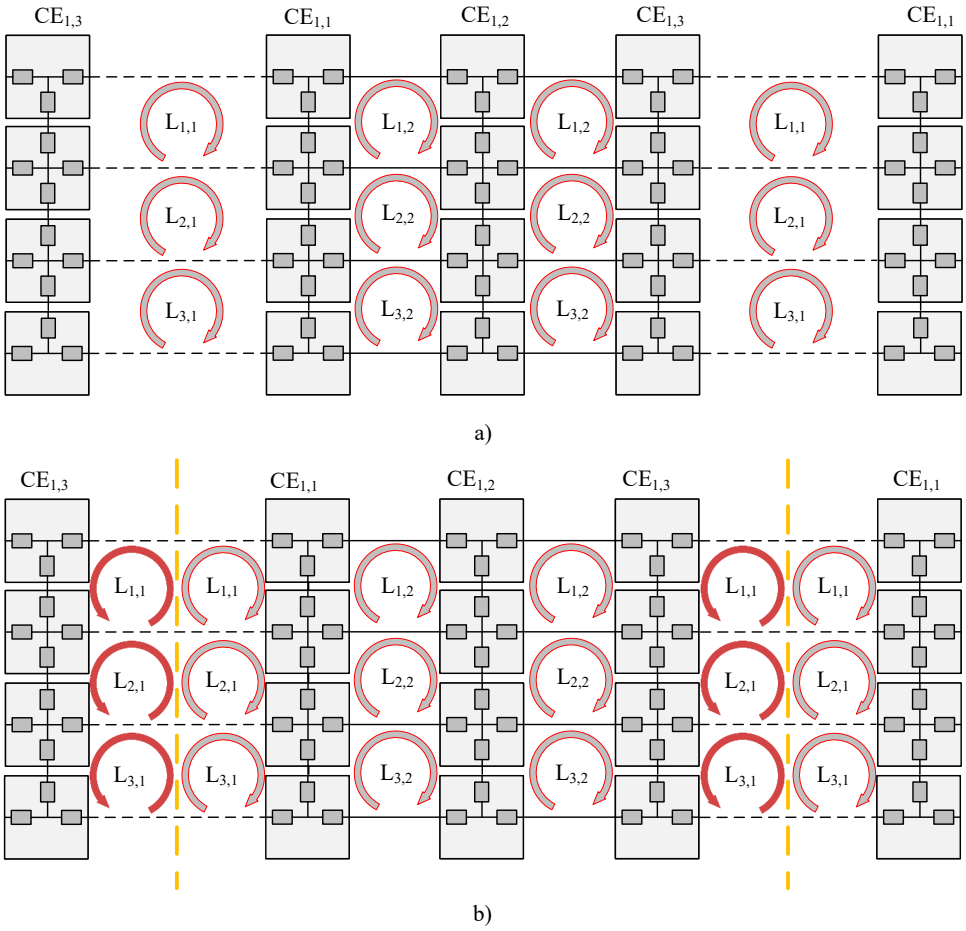


Figure 4.16: Visualization of periodic boundaries: (a) even periodicity, (b) odd periodicity

plained before. As it is seen, all the loops have the same direction. In the Figure 4.16 (b) the odd periodicity condition is shown. To emulate the unmodelled part's flux, loops with the index j=1 are first divided into two loops with opposite directions. The necessity to represent a loop in a divided way is based on the fact that the CEs with the index numbers $j = 1$ and $j = n_T$ are actually edge elements whose reluctances share the same flux but in opposite direction.

4.3.1.2 Writing R_L in Terms of Linear and Non-linear Reluctances

In the previous subsection it has been revealed that R_L can be written in terms of the loop incidence matrix L and diagonal matrix of reluctances $\mathbf{R}$ as in Equation (4.18). With the inclusion of $\mathbf{R}$ it is possible to separate linear and non-linear reluctances for different materials, using the material matrices M. In this manner, first M defined for each material needs to be transformed into diagonal

matrix incorporating all reluctances. This matrix will be shown as **M**. Additionally a constant diaganol reluctance matrix $\mathbf{R_C}$ needs to be constructed. Every element of $\mathbf{R_C}$ is calculated using Equation (4.12) without using the reluctivitiy term $v(B)$. Using those, it can be written for different materials that:

$$\mathbf{R_{air}} = \mathbf{M_{air}} \cdot \mathbf{R_C} \cdot v_{air} \tag{4.19}$$

$$\mathbf{R_{copper}} = \mathbf{M_{copper}} \cdot \mathbf{R_C} \cdot v_{copper} \tag{4.20}$$

$$\mathbf{R_{PM}} = \mathbf{M_{PM}} \cdot \mathbf{R_C} \cdot v_{PM} \tag{4.21}$$

Then for the linear materials it can be written:

$$\mathbf{R_{ns}} = \mathbf{R_{air}} + \mathbf{R_{copper}} + \mathbf{R_{PM}} + ... \tag{4.22}$$

Finally, R_L can be expressed in terms of seperate saturating and non-saturating reluctances as below:

$$R_L = L^T \left(\mathbf{R_{ns}} + \mathbf{M_{iron}} \cdot \mathbf{R_C} \cdot v(B)\right) L \tag{4.23}$$

Defining R_L in terms of seperate saturating and non-saturating reluctances is useful especially from the non-linear iteration point of view which will be explained in the next sub-chapter. It is important to underline that, material matrices M and consequently **M** needs to be updated for each step of rotation and needs to be rebuilt. Since only the rotor reluctances will be changed, stator part of the material matrices will remain the same.

4.3.2 Non-Linear Iteration Using Newton-Raphson Method

Newton-Raphson iteration is used for non-linear calculation of material properties. The method is used to calculate roots of non-linear functions in an iterative manner. Given a function $f(x)$ and an initial guess x^k, Newton-Raphson method can be written as below to find the next solution:

$$x^{k+1} = x^k - \frac{f(x^k)}{f'(x^k)} \tag{4.24}$$

Equation (4.24) is then used repeatedly until the desired value is reached. For multivariable functions, the equation takes the form:

$$x^{k+1} = x^k - J(x)^{-1} f'(x^k) \tag{4.25}$$

where $J(x)$ is the Jacobian matrix. Jacobian matrix can be written as below using the partial derivatives of $f(x_n)$ with respect to x_n:

$$J = \begin{bmatrix} \frac{\partial f_1}{\partial x_1} & \frac{\partial f_1}{\partial x_2} & \cdots & \frac{\partial f_1}{\partial x_n} \\ \frac{\partial f_2}{\partial x_1} & \frac{\partial f_2}{\partial x_2} & \cdots & \frac{\partial f_2}{\partial x_n} \\ \vdots & \vdots & \ddots & \vdots \\ \frac{\partial f_m}{\partial x_1} & \frac{\partial f_m}{\partial x_2} & \cdots & \frac{\partial f_m}{\partial x_n} \end{bmatrix}$$

As the general formulation suggests, an equation has to be in the form $f(x) = Ax - b$ for Newton-Raphson method to be applied. As a result, Equation (4.17) has to be transformed to the same form. Since the main variable to solve for is the loop fluxes ϕ_L, Equation (4.17) can be rewritten as Equation (4.26) in terms of flux dependent loop reluctance matrix R_L and MMF loops MMF_L. Here ϕ_L and MMF_L are used in their single column vector versions with size [n_L x 1].

$$r(\phi_L) = R_L(\phi_L)\phi_L - MMF_L \tag{4.26}$$

Function $r(\phi_L)$ is the residual function and needs to be reduced during the iterations. Now, when Newton-Raphson method is applied to the Equation (4.26), one can obtain Equation (4.27). The concurrent use of Equation (4.27) starts with an initial guess ϕ_L^k and continues until the selected error criteria is met. For the initial calculation of ϕ_L^k, Equation (4.17) is solved using an initial reluctivity (or permeability) value for saturable reluctances. For the other steps of the MEC simulation, the first iteration uses previous step's converged reluctivity values. Reluctivity matrices of the moving&rotationg parts need to be shifted as well to match the rotated material matrices.

$$\phi_L^{k+1} = \phi_L^{k+1} - J(\phi_L^k)^{-1} r(\phi_L^k) \tag{4.27}$$

The Jacobian of the system $J(\phi_L^k)^{-1}$ is the hearth of the Newton-Raphson method and to obtain the derivatives of each element of R_L with respect to each element

of ϕ_L is a long and complicated process. The problem arises as there is no direct relation between two quantities and a chain of relationships have to be build connecting reluctance loops elements to reluctances, reluctances to flux density, flux density to flux of each reluctance and finally to each flux loop element. An example of this process is explained step-by-step in [83]. An alternate method to obtain the Jacobian has been presented in [78] through a set of matrix operations and loop incidence matrix L plays a key role in that.

$$J = R_L + L^T(\mathbf{M_{iron}} \cdot \mathbf{R_C} \cdot \mathbf{A}^{-1} \cdot \frac{d\upsilon_{r_{RE}}}{d|B_{RE}|} \cdot \frac{d|B_{RE}|}{dB_{RE}})\ ((L\phi_L U) \cdot L) \tag{4.28}$$

In Equation (4.28), Jacobian matrix is given. Here $\mathbf{A}$ is the cross-section area of each reluctance in the diagonal form with the size [n_{RE} x n_{RE}]. Since it is diagonal matrix, inverse of A contains reciprocal of each cross section area of reluctances. The term $\frac{d\upsilon_{r_{RE}}}{d|B_{RE}|}$ is the derivative of reluctivity of each reluctance with respect to the absolute value of the flux density and $\frac{d|B_{RE}|}{dB_{RE}}$ is the derivative of the absolute flux density to the real flux density. The necessity for inclusion of these terms are due to the positive definition of the B-H Curve in the first quadrant. The derivative term $\frac{d\upsilon_{r_{RE}}}{d|B_{RE}|}$ can be calculated numerically using finite differences as shown with Equation (4.29). Calculation of this derivative term strictly depends on the B-H Curve and its definition. It is also possible to derive an analytical expression for it, if the B-H curve is defined with an equation. In this work, B-H curves are numerically defined and subjected to linear interpolation, hence a numerical derivative is used.

$$\frac{d\upsilon_{r_{RE}}}{d|B_{RE}|} = \frac{\upsilon_{r_{RE}}(|B_{RE}| + \Delta_B) - \upsilon_{r_{RE}}(|B_{RE}| - \Delta_B)}{2\Delta_{|B|}} \tag{4.29}$$

In Equation (4.29), $\Delta_{B_{RE}}$ is a small perturbation applied to the flux density in order to calculate the derivative.

Lastly, in the Equation (4.28) U is another connection matrix describing the relation between different flux loops. Its size is [n_L x n_L] and if any two loops are sharing a reluctance the associated value in the matrix becomes 1. Additionally all diagonal elements are 1. If the loops are not connected by any means its element U_{ij} becomes 0. An easy way to obtain U is through changing the nonzero elements of $L^T L$ with ones.

4.3.3 Calculation of Electromagetic Quantities

After the each converged step of MEC simulation, electromagnetic properties are calculated. First flux density of each reluctance needs to be computed, followed by the flux density of each CE. Afterwards torque and flux linkage can be obtained by using flux densities.

Using the loop incidence matrix L, flux passing through each reluctance can be calculated using Equation (4.30).

$$\phi_{RE} = L\,\phi_L \tag{4.30}$$

Here ϕ_{RE} stands for the flux belonging to each reluctance and its size is [n_{RE} x 1] where ϕ_L has the size [n_L x 1]. Once the flux of each element is found, flux density of each reluctance B_{RE} can be calculated using Equation (4.31). As in the previous notations A is the diagonal matrix of cross-section areas belonging to reluctances.

$$B_{RE} = \phi_{RE}^{T}\,A^{-1} \tag{4.31}$$

Elements of B_{RE} includes the flux densities of radial and tangential reluctances and hereafter these will be named as B_r and B_t for the following calculations. Since all of the flux densities are now known, it is possible to calculate flux densities for the CEs.

$$B_{rad_{ij}} = \frac{B_{r_{ij}} + B_{r_{i+1,j}}}{2} \tag{4.32}$$

$$B_{tan_{ij}} = \frac{B_{t_{ij}} + B_{t_{i,j+1}}}{2} \tag{4.33}$$

$$B_{ij} = \sqrt{B_{rad_{ij}}^2 + B_{tan_{ij}}^2} \tag{4.34}$$

In Equation (4.32) and (4.33) two radial and two tangential reluctances are averaged to find the value of flux density components. As for the flux density, Equation (4.34) is used.

After the calculation of flux densities, flux linkages and torque can be calculated. From the matrix M_{copper}, the indexes of CEs in the winding areas are

known and for each CE_{ij} neighbouring loop indexes can be written as $(i-1, j)$, $(i-1, j+1)$, (i, j), $(i, j+1)$. The loop indexes are in fact determined assuming that the winding CEs are not located on the boundary elements and if they are, loop indexes has to be changed accordingly. Using the Equation (4.35) flux linkages of CEs can be calculated. After that, flux linkage of a winding λ_W can be written by adding all of the $\lambda_{CE_{ij}}$ together.

$$\lambda_{CE_{ij}} = \frac{SA_{CE_{ij}}}{4SA_W} \sum_{i-1}^{i} \sum_{j=1}^{j+1} \phi_{L_{ij}} \tag{4.35}$$

At this point, one would obtain all the flux linkages of the winding regions λ_W which is equal to the number of slots divided by the periodicity. Additionally, winding configurations can be written for each phase. For instance, a single layer winding configuration for 36 slot 6 pole using a single pole perodicity, can be written as:

$$\begin{aligned} W_A &= [1 \quad 0 \quad 0 \quad 0 \quad 0 \quad -1] \\ W_B &= [0 \quad 0 \quad 0 \quad 1 \quad 1 \quad 0] \\ W_C &= [0 \quad -1 \quad -1 \quad 0 \quad 0 \quad 0] \end{aligned} \tag{4.36}$$

Then one can obtain the phase flux linkages with k_p being the periodicity number (for this example k_p=6) and N_t being the number of turns in each slot :

$$\lambda_A = \lambda_W W_A^T \cdot k_p \cdot N_t \tag{4.37}$$

$$\lambda_B = \lambda_W W_B^T \cdot k_p \cdot N_t \tag{4.38}$$

$$\lambda_C = \lambda_W W_C^T \cdot k_p \cdot N_t \tag{4.39}$$

If a double layer winding configuration is used, same procedure can also be followed with modified winding matrix.

For the calculation of the torque, Maxwell's Stress Tensor is used [85]. Torque calculation takes place in the airgap using the radial and tangential components of the flux density at a certain radius. It is generally recommended to have a number of mesh layers in the airgap region in FEA and the middle layers flux densities are taken into account of. Similarly, in the MEC at least 3 layers are used and the middle layer is used for the calculations.

$$T = \frac{2\pi}{n_T \mu_0} r^2 l_{axial} \sum_{j=1}^{n_T} B_{rad_{i,j}} \cdot B_{tan_{i,j}} \tag{4.40}$$

Using Equation (4.40) torque for each rotor position can be calculated. Here r is the radius where torque calculation takes place.

4.3.4 Overall Process of the Solution

Until now the whole solution procedure of the MEC is described. To sum up the whole procedure from start to end, a summary of the operations are shown in Figure 4.17.

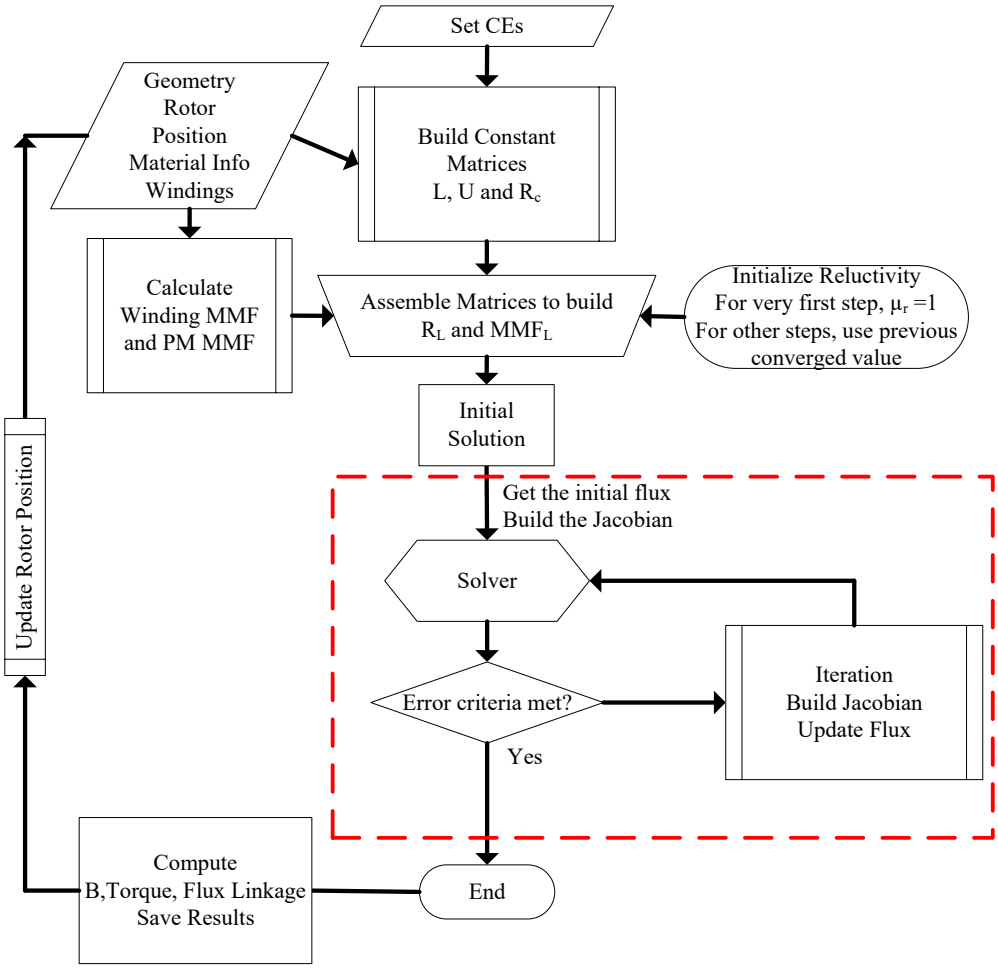


Figure 4.17: MEC solution procedure

As the basic building block of the MEC is the CE, first number of radial and tangential CEs needs to be selected along with the geometry, material and winding definitions. The next steps will then be building the material matrices M

and constant matrices L, U and R_c. At this stage Winding and PM MMFs (MMF_W and MMF_{PM}) are also formed. After that the initial loop reluctance matrix R_L is formed with the initial reluctivity and all other matrix operations are done. The first step of the solution start with the initial solution as shown in the Figure 4.17 and then the results are passed into the iterative solver part enclosed in red dashed lines in the flowchart. In the iterative solver, Jacobian matrix is built and ϕ_L is updated until the error criteria is met. As soon as the solution for a particular step is accepted as converged, post-processing is done by calculating the flux densities, torque and flux linkage values. After that rotor position is changed, preparing the matrices for the next step of the analysis. This routine then continues until the desired number of steps are completed.

4.3.5 Discussion on MEC Performance

All the steps and processes explained in the previous sections deal with matrix operations of big size. Distinctly, the most recurring equation involving matrix multiplication and inverses is Equation (4.28) and (4.27). These has to be run over and over again for the nonlinear iteration thus their execution plays a key role in the computation time of the whole code.

To give an idea of the matrix sizes, if the total number of CEs are 6750 then total number of loops becomes 6600. This makes a size of [6600 x 6600] matrix for the matrices J and R_L. Luckily most of the elements of these matrices are zero and in this case sparse matrices can and must be used. As an example, in the MATLAB environment where the MEC analysis is implemented, matrix multiplication of two diagonal matrices with size [6600 x 6600] takes about 2.068 s whereas doing the same operation with the sparse version of these matrices yield 7 x 10^{-4} s. Working with sparse matrices basically enables to operate only on the nonzero elements rather than going for full-size matrix multiplication. Sparse matrices are generally used whenever there are matrix operations of big-size and also common in FEM.

Undoubtedly, employing sparse matrices significantly accelerates the execution of matrix operations; nevertheless, it is essential to adhere to other beneficial coding practices as well. A noteworthy practice worth highlighting is the usage of

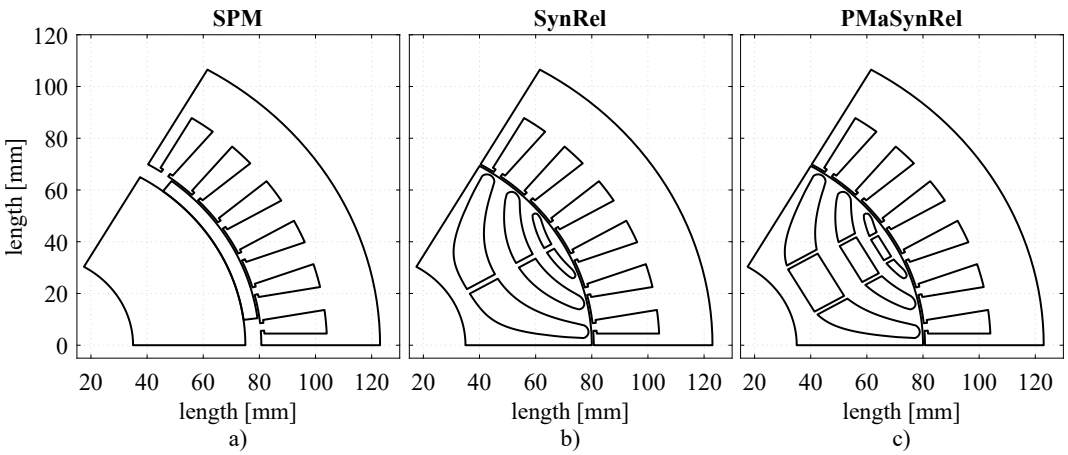


Figure 4.18: Geometries of analyzed machines: (a) SPM, (b) SynRel and (c) PMaSynRel

loops. Their concurrent use should be limited in order to prevent any computational burden, especially when a lot of parameters are employed. During the development of the code, these are taken into account to make most of the MEC regarding the fast computation.

4.4 Analysis Using the MEC

In this part, three different machine types, ie SPM, SynRel and PMaSynRel machines are analyzed at different conditions using MEC and results are compared in detail with the ones obtained by FEM. All three machines do share the exact same stator, winding configuration and outer dimensions. In fact, the stator is the same as the one used in optimizations in chapter 2. General parameters of the stator and detailed rotor parameters belonging to machines are given in Table 4.1. Lamination material for both rotor and stator is M250-50A and all magnets are Neodymimum type N42EH class. Winding configuration is the single-layer 3-phase winding layout as previously defined with Equation (4.36). The geometries of the machines are shown in Figure 4.18. It is to be noted that, these machines are just created for analysis purposes and are not a final product of a design process or an optimization.

4.4.1 Single Point Analysis

All machines are analyzed using a peak current of 82A and a phase advance angle of 45^o. One sixth of the electric period (20 mechanical degrees) are an-

Table 4.1: Dimensions of the SPM, SynRel and PMaSynRel machines.

General Dimensions		
Parameter	Value	Unit
Statour outer radius	123	mm
Rotor outer radius	80	mm
Air-gap length	0.7	mm
Shaft radius	35	mm
Stack length	120	mm
Rated current	82	A_{peak}
Current density	10	A_{RMS}/mm^2
Cooling flow Rate	10	L/min
Lamination material	M250-35A	
SPM Parameters		
Magnet thickness	5	mm
Magnet span	45	mech. deg. ^{o}
Magnet Material	N42EH	
SynRel Parameters		
No of barriers	3	
Radial ribs thickness	2	mm
Tangential ribs thickness	1	mm
PMaSynRel Parameters		
No of Barriers	3	mm
Magnet Thicknesses	3.014-6.84-12.18	mm
Radial ribs thickness	3	mm
Tangential ribs thickness	1	mm
Magnet Material	N42EH	

alyzed using 1 mechanical degree steps. Discretization of the machines are achieved using 60 tangential and 63 radial CEs, making a total number of 15000 reluctance elements, 3780 CEs and 3720 loops. Distribution of radial CEs are presented in Table 4.2.

On the other hand, mesh sizes of the FEM models are deliberately reduced to be close to no of CEs for a clear comparison of results and computation times. Mesh sizes are 3614, 4958 and 4761 for SPM, SynRel and PMaSynRel machines, respectively.

Airgap flux density waveforms of the machines are presented in Figure 4.19 where the rotor position is θ_r=0^o. A good agreement between FEA and MEC results are obtained through comparison. Based on the Figure 4.19 it can be inferred that radial flux densities are well matching with only very minor deviations. Comparing the tangential flux densities, there are visible discrepancies occurring particularly at the peaks of the waveform. Clearly, since the radial flux densities are well matching and having higher amplitudes than tangential flux densi-

ties, in overall flux density waveforms are only slightly effected. Differences in the airgap flux density plots can be attributed to the resolution differences of two models, mainly arising from the tangential points that the flux densities are obtained. Although the mesh size of the FEM models are decreased, still the airgap mesh is quite high compared to MEC models. The mesh in MEC also effects the geometry description which means that there is an additional error coming from the imperfect description of the machine geometries.

Flux density distributions of the machines obtained from the field solutions with FEM and MEC are given in Figure 4.20. The contour plots of the flux density distributions show that flux densities in the most sensitive regions such as stator tooth tips, tangential and radial ribs are well captured. This, along with the airgap flux density graphs indicate that saturation is well managed.

Comparison between torque, torque ripple and analysis times are provided in Table 4.3. In this single operating condition, average torque values are in a good harmony. On the other hand, it is seen that the discrepancy in tangential flux densities as discussed earlier are carried forward in the torque calculation and reflected as a difference in torque ripple values. Difference in the torque ripple will be further investigated in a wider range of operation points and by means of a sensitivity analysis in the next subsections. Considering the computation times there is a clear difference between the FEM and MEC analysis. MEC analysis is 12,12.5 and 20 times faster then the consequent FEA for SynRel, PMaSynRel and SPM machines respectively. The varying computation times for both FEA and MEC analysis is a

Table 4.2: Discretization properties of machines.

Stator and Airgap	
Part	Number of Radial CEs
Stator yoke	5
Stator teeth	5
Stator tooth tip	2
Airgap	3
SPM Rotor	
Magnet	6
Rotor yoke	42
SynRel and PMaSynRel Rotor	
Tangential ribs	2
Rotor	48
Number of Tangential CEs = 60	

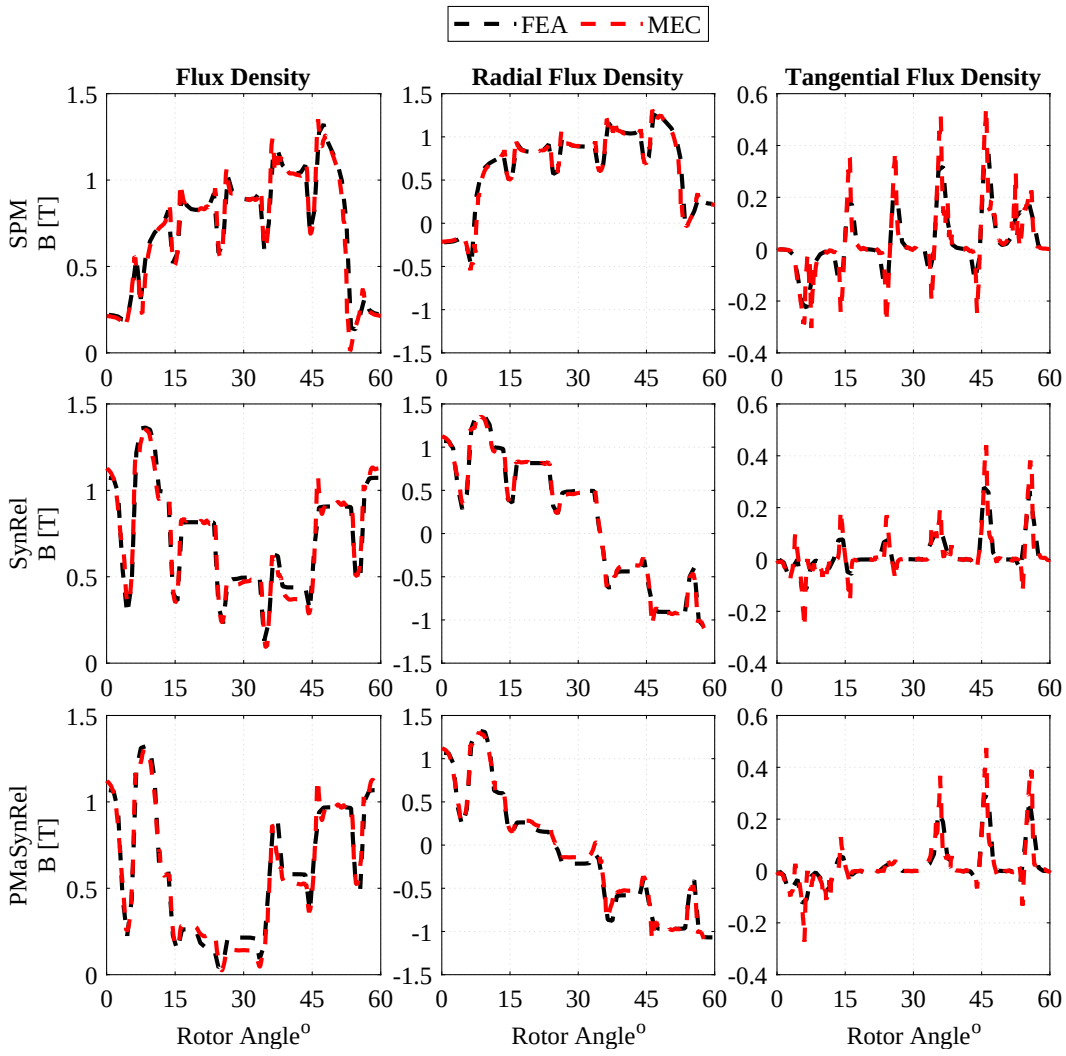


Figure 4.19: flux densities

result of different iteration numbers affected by dissimilar saturation characteristics of the machines.

4.4.2 Analysis in the DQ Current Plane

Apart from the single point analysis it is also important to investigate the MEC results in a wide range of operation points to better understand its capabilities in terms of saturation. All machines are analyzed in the dq current plane up to double the rated current (160 A_{peak}) with equally spaced 100 points. Analysis is again done for one sixth of the electrical period and one degree mechanical step is used (total 21 steps). Results of these analysis are shared in terms of torque, torque ripple and dq fluxes in Figure 4.21.

Flux-current relationship is shown in the first column of the Figure 4.21

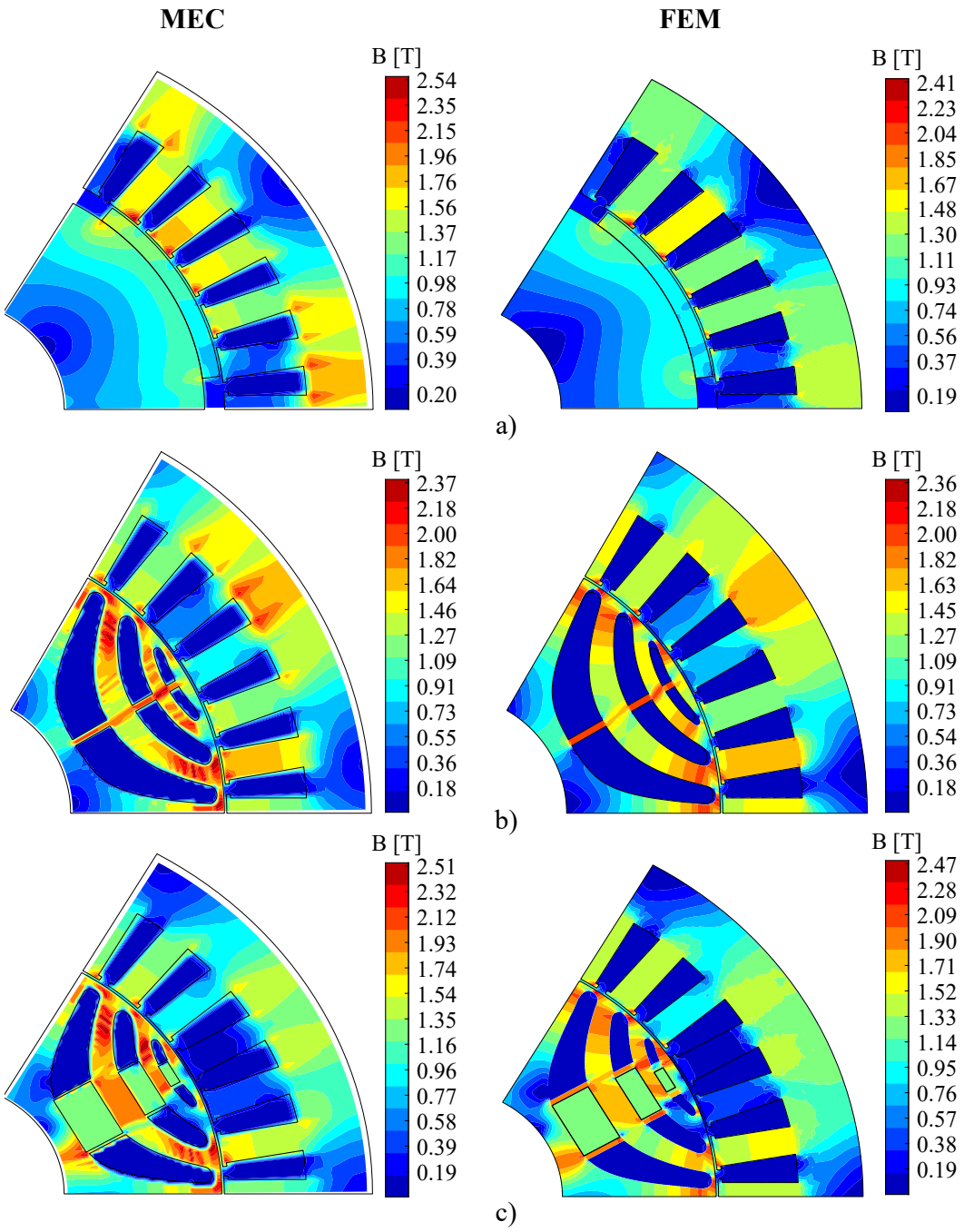


Figure 4.20: Flux density distributions obtained with MEC and FEA for analyzed machines: (a) SPM, (b) SynRel and (c) PMaSynRel

in terms of dq fluxes as a function of the homonym current. On the next column of graphs, torque is given as a function of dq currents. Similar to the torque, torque ripple is also shown as a function of dq currents on the last column. For the torque ripple graphs, only the regions where there is torque production for all machines are shown as there is no torque production when either i_d= 0 or i_q= 0.

SPM machine shows a good matching trend regarding fluxes and torque contours. The q-axis (magnet axis) flux obtained with the MEC is slightly higher

Table 4.3: Single point analysis comparison of FEM and MEC

	SynRel		PMaSynRel		SPM	
	FEM	MEC	FEM	MEC	FEM	MEC
Mesh&CEs	4958	3780	4761	3780	3614	3780
Time [s]	46.4	3.8	52	4.1	47.9	2.4
Torque [Nm]	74.9	74.6	104.7	109.4	120.6	122.2
Ripple [%]	12.3	33.3	17.4	29.4	25.8	23

than FEM result which can be explained by the lack of perfect geometry description. In this case actual PM span is lower than the PM span obtained with the MEC. Observing the flux density distribution in Figure 4.20 it is seen that the PM is covering slightly more area than it should have. Evidently, this is being reflected in the torque contours and MEC torque is marginally greater than FEM values. Comparing on a point to point basis the average difference in torque is 1.7 %. The torque ripple contours however do not show a qualitative match of contour shapes due to the lack of tangential points for the solution obtained with the MEC. This being the case, there are large areas between the contour lines that are close in terms of value.

For SynRel machine both d and q-axis fluxes obtained with MEC show a very good agreement with the FEM results. The small incline at the start of the q axis flux linkage curve indicates that the saturation is well captured even in the radial ribs region. Well predicted saturation is particularly significant for this type of saturation dependent machines. Comparing the torque contours there is a good harmony between the results and the difference between the obtained torque values are an average of 2.2%. Torque ripple comparison between the FEM and the MEC yields similar contour trends. Contradicting with the contour shapes, torque ripple values are seen to be distant from each other. Discretization of the mesh in the airgap region can be put forward as the primary source of discrepancy.

In the case of PMaSynRel machine, the MEC-computed d-axis flux linkage well matches the FE one while the q-axis one shows an almost constant difference between the MEC and FEM results. Given the fact that this mismatch is present at i_d=0A (no cross-saturation), it can be ascribed to an error in the estimation of the PM flux linkage. Indeed, a rectangular shaped PM cannot be perfectly represented with a polar discretization and in this case it is overestimated. Higher

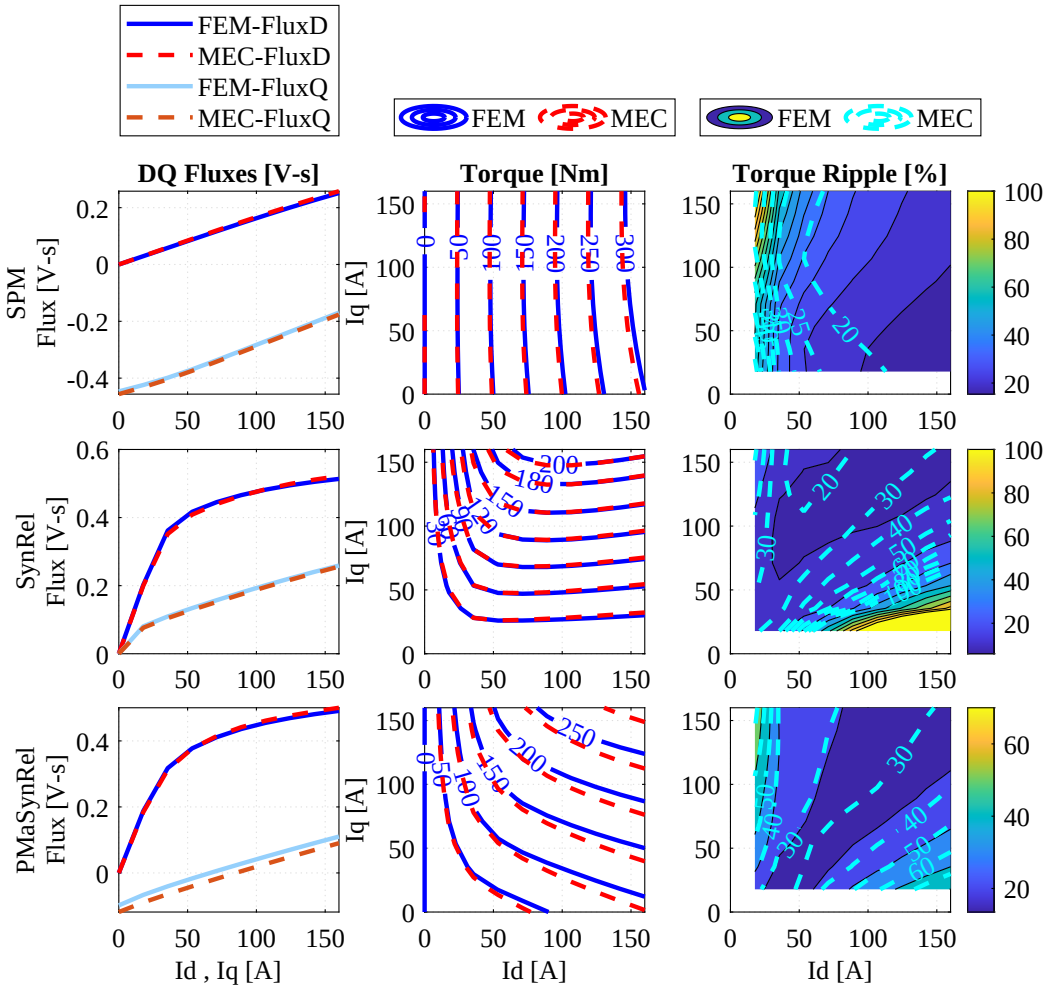


Figure 4.21: Results of *dq*-current plane analysis for SynRel, PMaSynRel and SPM machines using FEM and MEC

PM flux further distorts the torque contours, causing the MEC results to be higher at some extent, however the average error in the torque points is 7.3%. Apart from the PM flux, another possible reason for the difference is the geometry mismatch in the radial ribs regions as they can only be approximated to a certain level directly related to length of CEs. For the torque ripple it is seen that the contour shapes are in a matching trend but as was the case with the other machines in terms of exact values they differ from each other.

4.4.3 Sensitivity Analysis with Respect to CEs

The aim of this study is to identify sensitivity of CEs to the results through a simple sensitivity analysis by changing the number of CEs. For this case study, PMaSynRel machine is selected as the torque comparison in the previous subsec-

tion yielded highest discrepancy. Using a single operating point i_d=124.45A and i_q=17.78A, PMaSynRel machine is subjected to changes in the number of radial and tangential CEs in different regions of geometry. As a reference FEA results in 91Nm torque and 41% torque ripple at this point and takes 47s to complete.

Performance with respect to number of CEs are investigated in four scenarios where the number of radial CEs for specific parts and number of tangential elements are varied. In each case the unmentioned parts will have the same number of CEs as was presented in Table 4.2. Analysis time with increasing total CEs is also captured, averaging a total of 10 analysis for each step belonging to each scenario. In the following, four different sensitivity cases are shown:

- S_1: The number of radial CEs describing the rotor tangential ribs are changed;
- S_2: The number of radial CEs describin the rotor are changed where the ribs part stays constnat (=2);
- S_3: The number of radial CEs describing the sator yoke and teeth parts are equal and changed;
- S_4: The number of tangential CEs are changed in multiples of 60 which is the mechanical angle of a single pole due to symmetry.

Results of S_1 and S_2 are shown in Figure 4.22. In the case S_1, it certainly appears that increasing the number of radial CEs in the tangential ribs regions have no effect to neither torque nor torque ripple but to increase computation time. When the radial CEs in the rotor region are increased in case S_2, it is seen that there are some slight variations both in terms of average torque and torque ripple however they remain to be negligible and there is no clear benefit.

The remaining two cases S_3 and S_4 are shown in Figure 4.23. Increasing radial CEs in stator yoke and teeth regions in case S_4 indicates a beneficial trend towards the reference values obtained through FEA. As a remark, it can be deduced that increasing the CEs here is beneficialy only up to a certain point above which does not lead to a major benefit but just increases the computational time. The most effecting parameter seems to be the number of tangential CEs as presented in the case S_4. In this case both average torque and torque ripple moves towards the refer-

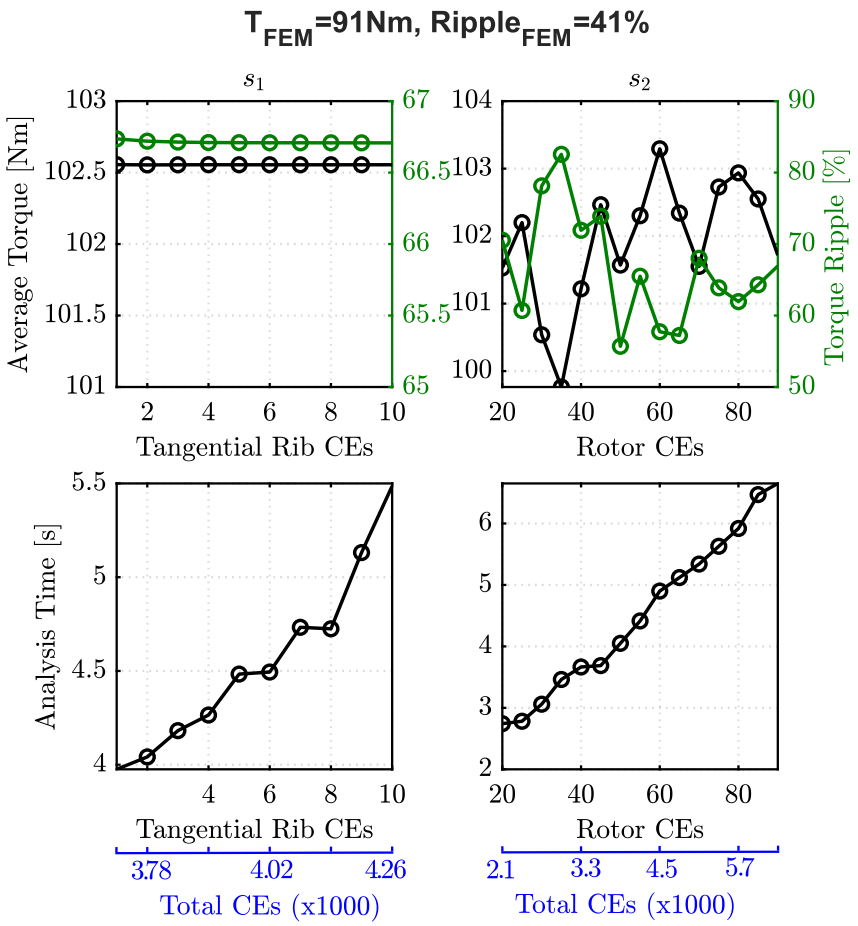


Figure 4.22: Results of sensitivity analysis S_1 and S_2

ence values with reduced discrepancy with a drawback of increased computational time.

4.5 Experimental Verification

In order to further elaborate on the capabilities of the developed MEC, a SynRel machine is tested and the results obtained through tests, FEA and MEC are compared.

Machine to be tested is an off-the-shelf SynRel machine whose geometry is shown in Figure 4.24. It has rounded slots and four flux barriers in the rotor where the innermost barrier has a radial rib for mechanical integrity. The number of poles and slots are, 4 and 36, respectively. It has a rated current of 2.9 A_{rms} and a rated torque of 7 Nm at the speed of 1500 RPM. Winding of the machine is a single layer distributed winding. The specifications and dimensions of the machine are summarized in the Table 4.4.

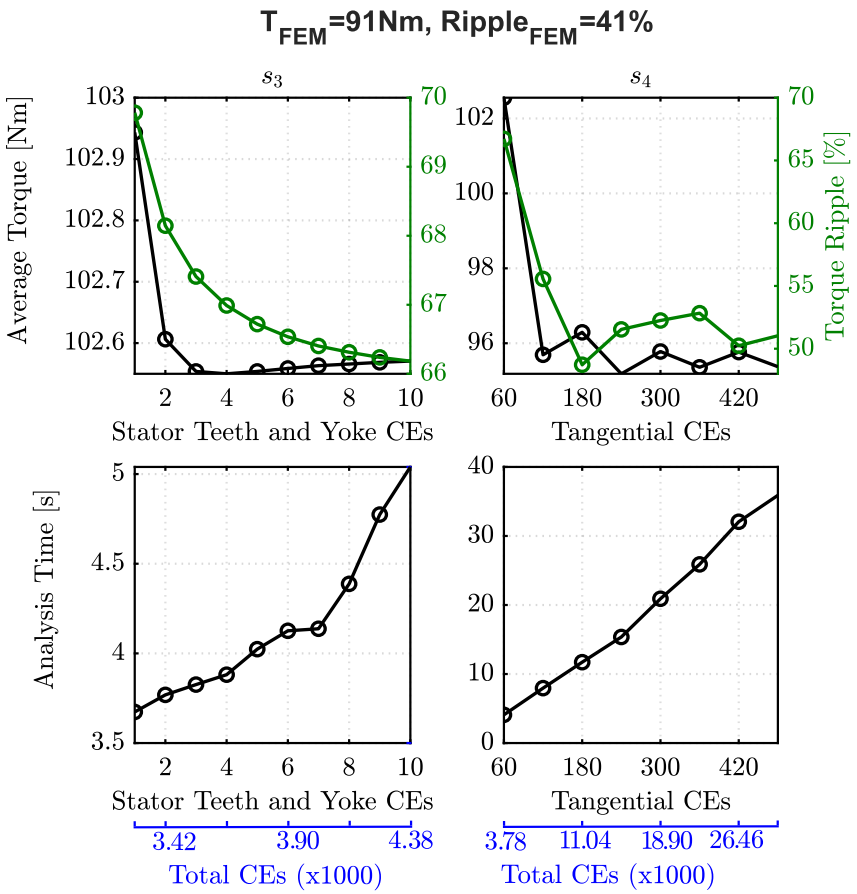


Figure 4.23: Results of sensitivity analysis S_3 and S_4

4.5.1 Test Procedure

Test procedure presented in [86] is followed throughout the tests. In this methodology the aim is to obtain flux linkages in a number of points to identify magnetic characteristics of the machine. Desired operation conditions lie on the dq current plane irrespective of the machine type though the quadrant of interest changes. PMaSynRel and SynRel machines mostly operate on the first quadrant for motoring mode shaped by positive d and q-axis currents. Therefore the first step is to build a number of points in the dq current plane. For a uniform distribution of current pairs (i_d, i_q) a rectangular grid division is used.

Since it is not possible to directly measure the fluxes, voltages should be measured. However due to the resistive behaviour of the conductors, measured voltage includes resistive voltage. Following describes the required process to obtain fluxes without the resistance effect.

Given the current vector $\overrightarrow{I_S}$ and flux vector $\overrightarrow{\lambda}$, voltage vector $\overrightarrow{V_S}$ can be written in terms of phase resistance R_S as in Equation (4.41). Here w stands for the

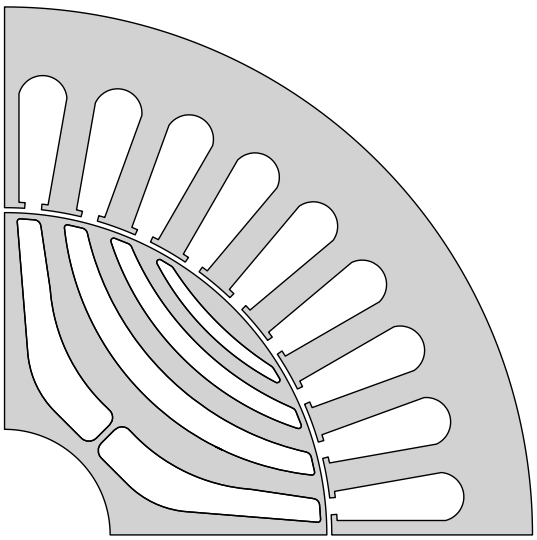


Figure 4.24: Geometry of the SynRel machine to be tested.

Table 4.4: Specifications of the SynRel machine to be tested.

General Dimensions		
Parameter	Value	Unit
Statour outer radius	75	mm
Rotor outer radius	45.78	mm
Shaft radius	15	mm
Lamination material	M400-50A	
Winding Properties		
No of layers - type	1 - Distributed	
No of turns per slot	82	
Specifications		
Rated speed	1500	RPM
Rated torque	7	Nm
Rated power	1.1	kW
Rated current	4.1	A_{peak}
Rated voltage	400	V
Maximum speed	2100	RPM

electrical speed. Current and flux vectors can be consequently decomposed into d and q-axis components as in Equation (4.42) and (4.43).

$$\overrightarrow{V_S} = v_d + j\, v_q = R_S \overrightarrow{I_S} + j\, w\, \overrightarrow{\lambda} \tag{4.41}$$

$$\overrightarrow{I_S} = i_d + j\, i_q \tag{4.42}$$

$$\overrightarrow{\lambda} = \lambda_d + j\, \lambda_q \tag{4.43}$$

Voltage components v_d and v_q can be further written as:

$$v_d = R_S\, i_d - j\, w\, \lambda_q \tag{4.44}$$

$$v_q = R_S\, i_d + j\, w\, \lambda_d \tag{4.45}$$

Two current vectors then can be written as $\overrightarrow{I_M}$ and $\overrightarrow{I_G}$ where the former stands for motor operation and the latter stands for braking or generator operation. Consequently their d and q-axis current components can be written as below corresponding to being in the first and fourth quadrant, respectively:

$$\overrightarrow{I_M} = i_d + j\, i_q \tag{4.46}$$

$$\overrightarrow{I_G} = i_d - j\, i_q \tag{4.47}$$

When the motor is operated with these motoring and generating current sets, resultant fluxes, as it is the case with the current pairs, become conjugate. This is showed with Equation (4.48) and (4.49).

$$\overrightarrow{\lambda_M} = \lambda_d + j\, \lambda_q \tag{4.48}$$

$$\overrightarrow{\lambda_G} = \lambda_d - j\, \lambda_q \tag{4.49}$$

Corresponding voltage vectors then can be written as:

$$\overrightarrow{V_M} = v_{d_M} + j\, v_{q_M} = R_S\, \overrightarrow{I_M} + j\, w\, \overrightarrow{\lambda} \tag{4.50}$$

$$\overrightarrow{V_G} = v_{d_G} + j\, v_{q_G} = R_S\, \overrightarrow{I_G} + j\, w\, \overrightarrow{\lambda} \tag{4.51}$$

Then, averaging two voltage vectors lead to two expressions:

$$\frac{\overrightarrow{V_M} + \overrightarrow{V_G}}{2} = \frac{v_{d_M} + v_{d_G} + j\, v_{q_M} + j\, v_{q_G}}{2} \tag{4.52}$$

$$\frac{\overrightarrow{V_M} + \overrightarrow{V_G}}{2} = \frac{R_S\, i_d + j\, R_S\, i_q + R_S\, i_d - j\, R_S\, i_q + j\, w\, (\lambda_d + j\, \lambda_q) + j\, w\, (\lambda_d - j\, \lambda_q)}{2} \tag{4.53}$$

Right hand side of the Equation (4.53) can be simplified to obtain Equation (4.54):

$$\frac{\overrightarrow{V_M} + \overrightarrow{V_G}}{2} = R_S\, i_d + j\, w\, \lambda_d \tag{4.54}$$

For the Equation (4.52), if Equation (4.44) and (4.45) is substituted into it, one can obtain:

$$\frac{\overrightarrow{V_M} + \overrightarrow{V_G}}{2} = \frac{R_S\, i_d - j\, w\, \lambda_q + R_S\, i_d + j\, w\, \lambda_q + j\,(v_{q_M} + v_{q_G})}{2} \tag{4.55}$$

If this is further simplified, it is possible to obtain:

$$\frac{\overrightarrow{V_M} + \overrightarrow{V_G}}{2} = R_S\, i_d + \frac{j(v_{q_M} + v_{q_G})}{2} \tag{4.56}$$

Finally, equating Equation (4.54) and (4.56) together yields:

$$\frac{v_{q_M} + v_{q_G}}{2\, w} = \lambda_d \tag{4.57}$$

Therefore it becomes possible to obtain d-axis flux without the resistive voltage drop by driving the motor in motoring and generating modes and average the q-axis voltages. Other resistive voltage drops arising from inverter are also eliminated this way. A similar approach can be followed to obtain q-axis flux by starting from $\frac{\overrightarrow{V_M} - \overrightarrow{V_G}}{2}$. From temperature point of view, Equation (4.57) is valid when it is constant, in other words when the two R_S values in the motoring and generating mode is equal. Without doubt, there might be some change in the temperature if these tests are conducted right after each other. A way to mitigate this is to drive the motor in motoring-generating-motoring sequence and first average the voltages between two motoring modes and then average between the generating and the already averaged motoring voltages. This way any temperature increase would be removed. Another approach would be to leave a certain unoperated time between the motoring and genearing modes to prevent increasing temperature. In case of a machine with PMs, with the changing temperature PM flux will change, therefore it is critical to maintain a certain temperature.

Another practise to follow in this methodology is to appropriately determine the time spent on each motoring and generating mode to obtain steady state

values. It is recommended to average all the quantities of interest over at least a mechanical period duration. This way it would be possible to eliminate not only inverter related disturbances but also possible mechanical ones [86].

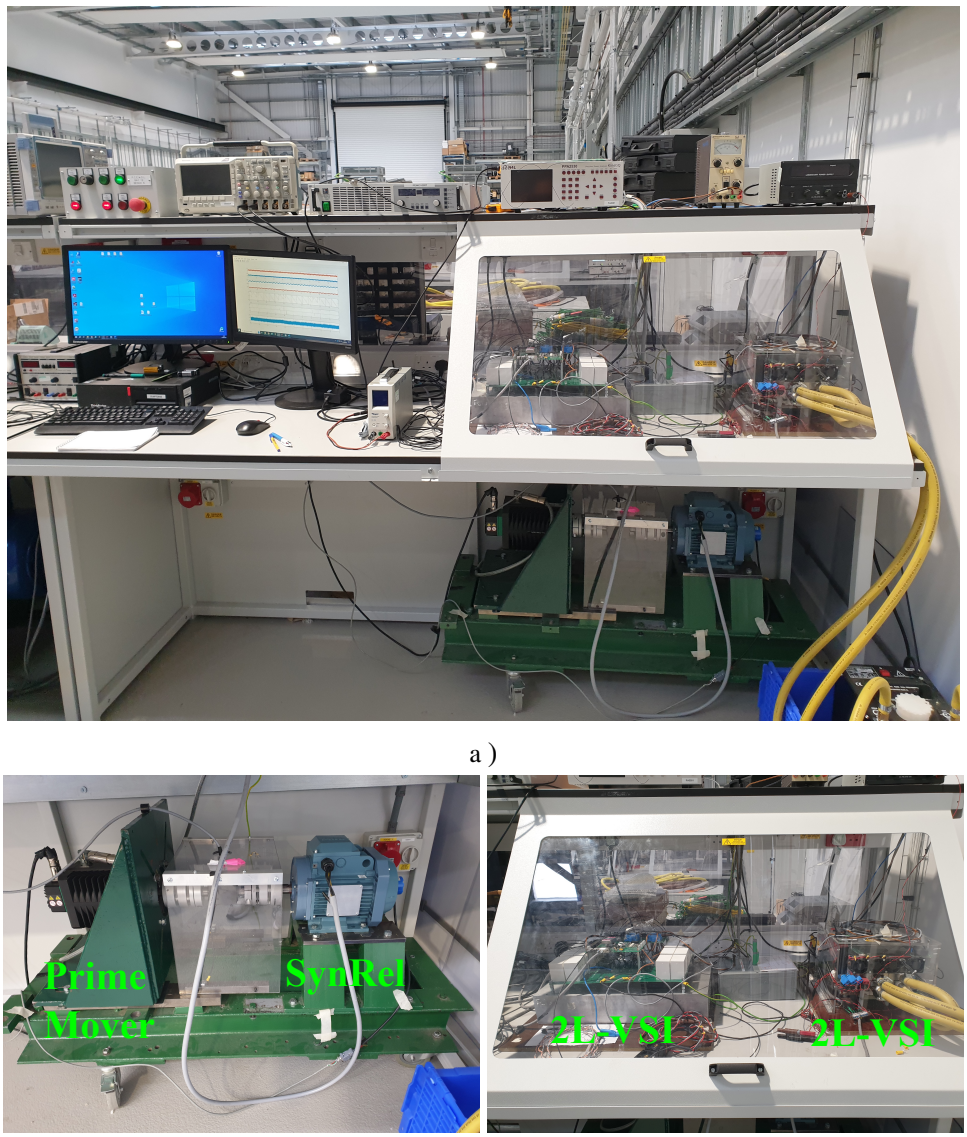
The speed w where the test is conducted should be selected based on two critical points. The first point is to select a speed high enough to obtain a high enough voltage to be accurately measured. The other point is to select a low enough speed so that the effect of iron losses can be neglected and flux vectors obtained using two conjugate current pairs remain conjugate [86].

For the identificaiton of the SynRel machine, dq current plane is divided into 0.5A steps up to 5.5 A_{peak} in both axes. In order identify fluxes without the disturbing effect of the speed, tests are done at one third of the rated speed at 500 RPM.

4.5.2 Test Setup

A test bench is specifically setup in purpose of obtaining the electromagnetic characteristics of the SynRel machine. Overall and detailed visuals of the bench components are shown in Figure 4.25. In Figure 4.25 b) prime mover and the SynRel is shown. Prime mover is a permanent magnet synchronous machine (PMSM) and during the tests it is used to maintain a constant speed. Both prime mover and the SynRel machine has position feedback sensors attached to end of their shafts. For the SynRel machine it is a TAMAGAWA absolute encoder. PMSM and the SynRel are coupled through a torquemeter.

On the drive side there are two inverters, each dedicated for a machine. Inverters are two-level voltage source inverters and they are purposedly share the same DC-link fed by a DC power supply to enable re-circulation of the power. To control the machines the uCube control platform which is previously developed in Power Electronics, Machines and Control Research Group at the University of Nottingham is employed [35]. The current and voltage signals are read in the uCube through an analog to digital converter. The same control platform is used to control both the PMSM and the SynRel.



a)

b)

c)

Figure 4.25: Test setup used to measure characteristics of the SynRel motor: a) overal test setup, b) SynRel and prime mover, c) control platform and inverter.

4.5.3 Results

4.5.3.1 Comparison Between FEA and MEC

SynRel machine is analyzed using FEM and MEC in the dq current plane up to 5.5 A_{peak}, with 0.5 A steps. Each point of analyses has been conducted for a period corresponding to one sixth of the electrical period, and a total of 30 mechanical steps.

Since the machine consists of 4 poles and 36 slots only a quarter of the machine can be analyzed based on the periodicity conditions without losing any accuracy. For this reason, number of tangential CEs in the MEC has been set to 90

to have an overall good resolution of the machine geometry. Number of radial CEs in different parts of the machine have also been selected to have a good description and are given in Table 4.5. Particularly, due to the existence of round stator slots, number of CEs in the stator teeth region had to increased. Rotor discretization in terms of radial CEs are also relatively high due to the number of barriers and radial structural rib. The geometry of the machine and the CEs are drawn all together and shown in Figure 4.26. Total number of CEs adds up to be 6750.

Table 4.5: Discretization properties of the SynRel machine under test.

Stator and Airgap	
Part	Number of Radial CEs
Stator yoke	5
Stator teeth	25
Stator tooth tip	2
Airgap	3
Rotor	
Tangential ribs	2
Rotor	40
Number of Tangential CEs = 90	

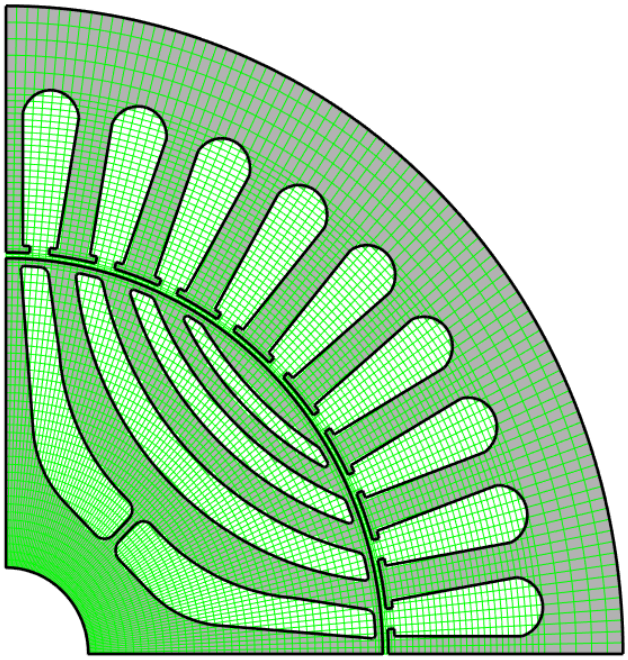


Figure 4.26: Discretization of the SynRel machine to be tested.

The results are compared in terms of fluxes, average torque and torque ripple and are shown in Figure 4.27. Comparison between the results yields a good match in general for all the compared quantities. When the q-axis fluxes are compared, it is seen that when $i_d = 0$ and $i_q \neq 0$ there is almost a perfect match. How-

ever, with the increasing i_d there seems to be a slight mismatch between the values. There are two possible reasons for this discrepancy which can be explained by the not perfect geometry discretization achieved by MEC and the way flux paths (in radial and tangential directions) occur in the MEC. This mismatch is not reflected to torque contours as from the figure it is clear that results are in good harmony. Torque ripple values, though not matching perfectly, are close to each other both in terms of contour shapes and values.

In terms of computation time for a single operating point where both i_d and i_q is equal to 4 A, the time required to complete FEA is 49s whereas using MEC a time of 6.5s can be achieved.

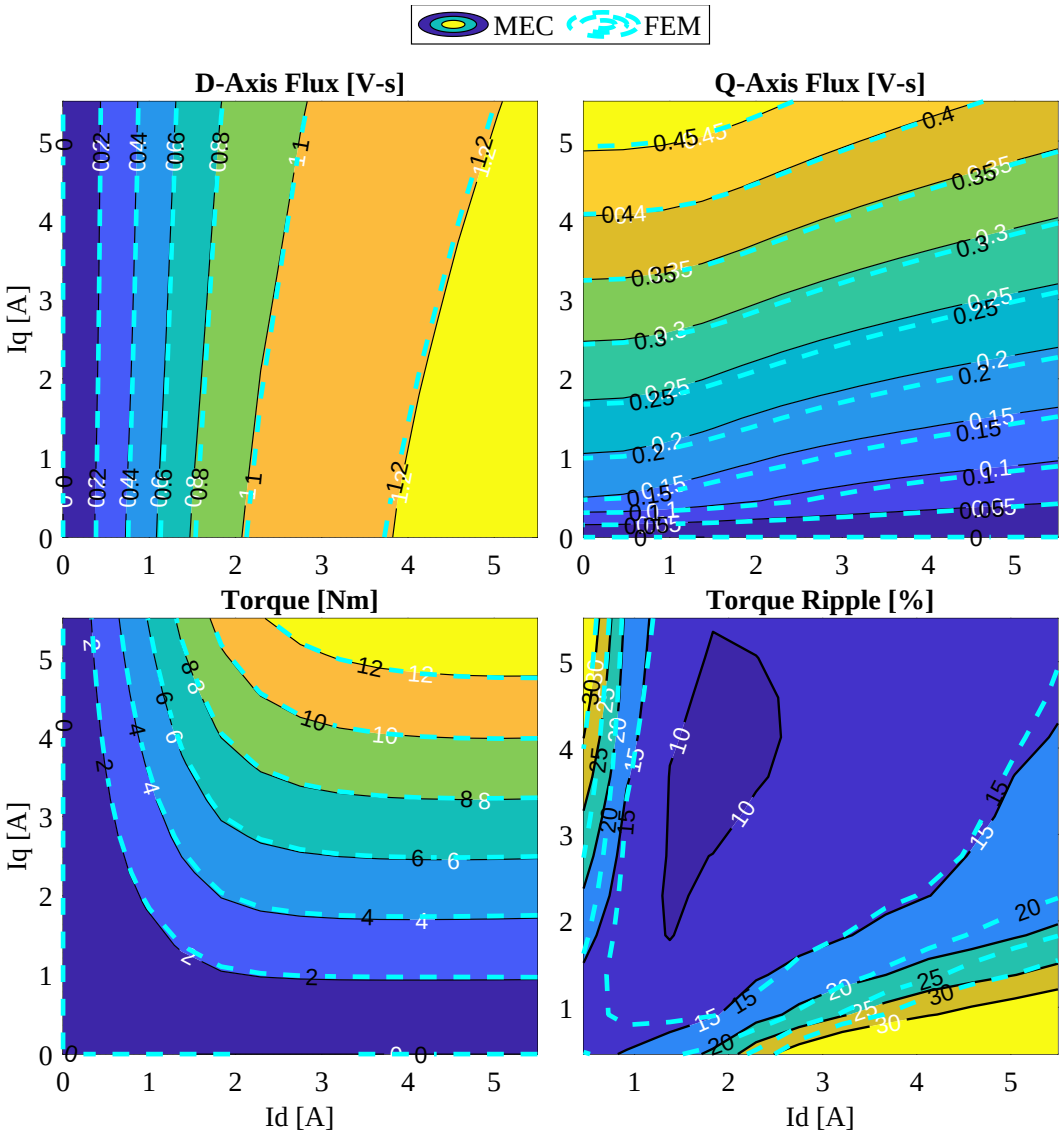


Figure 4.27: Comparison of results obtained by means of FEA and MEC analysis: a) *d*-axis flux, b) *q*-axis flux, c) torque, d) torque ripple.

4.5.3.2 Comparison Between Test and Analysis Results

Test results and the results obtained with FEA and MEC are put together and shown in Figure 4.28. As a general trend a close match is obtained in terms of d-axis fluxes and torque contours. Speaking of flux in the q-axis, it seems that the test results are lower than both of the analysis results. The q-axis flux being lower also creates some mismatch in the torque due to lower anisotrophy predicted with the analysis.

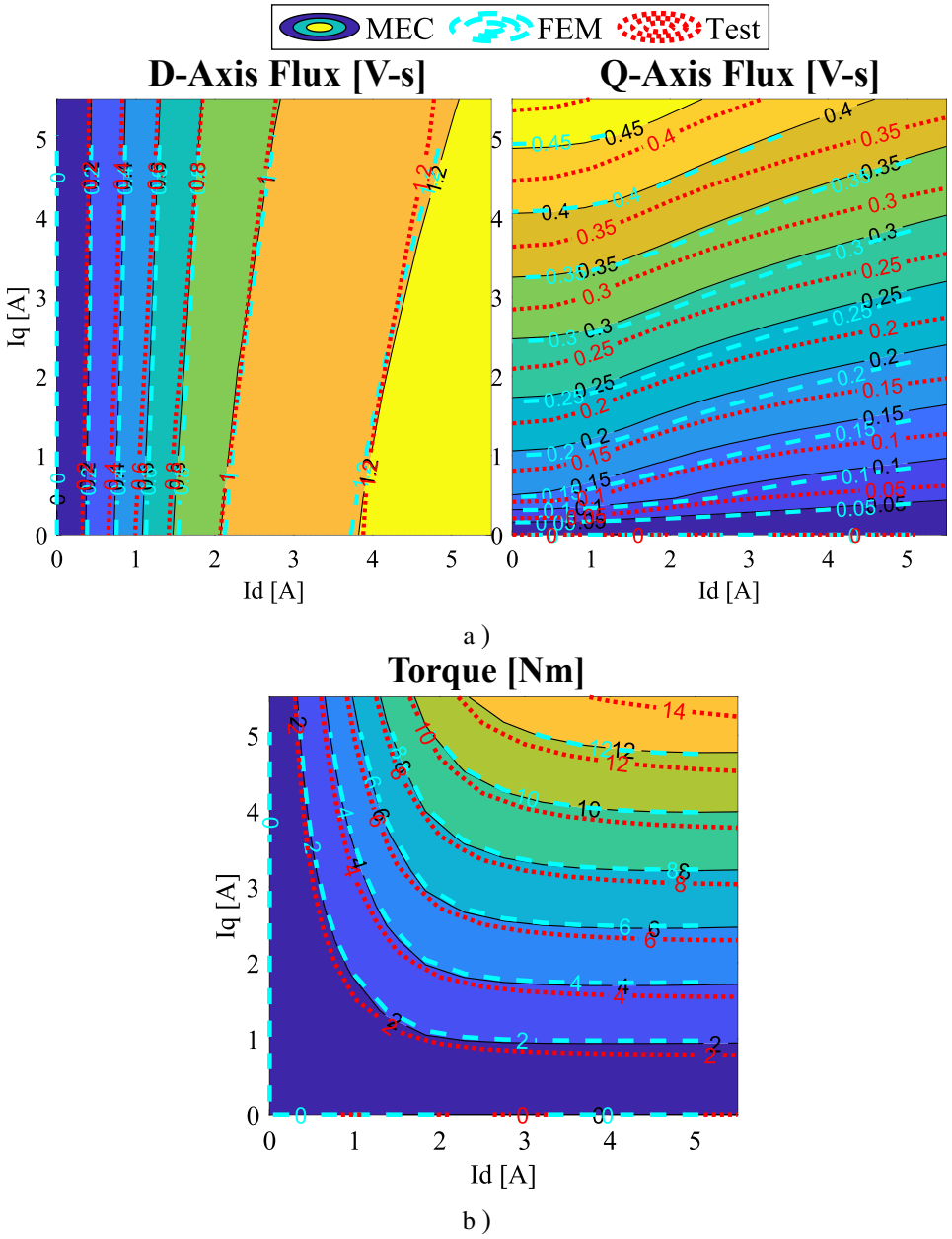


Figure 4.28: Comparison of test versus analysis results: a) d-axis flux, b) q-axis flux, c) torque.

When comparing the results, the effect of manufacturing needs to be taken

into account as even small changes in the geometry or any alteration of the magnetic properties during manufacturing can lead to different outcomes. Keeping in mind all these information and the overall close match of torque results both MEC and FEA analysis yielded a good prediction of real machine performance.

4.6 Conclusion

In this part of the thesis, a highly detailed version of magnetic equivalent circuits, which is capable of performing as accurate as state-of-the-art finite element method with much lower computation times is presented.

The description of the MEC began with investigation of literature view to identify the general methodologies, advantages and disadvantages to enlighten aims and objectives. To that extend it has been revealed that a general purpose MEC suited for different machine topologies and geometries, taking into account of nonlinear behaviour of the iron material are not yet available or limited in usage. Therefore the objective has been defined as providing a comprehensive approach to build a MEC of such.

MEC with these properties then started to be developed. First, geometry discretization using cell elements incorporating bi-directional reluctance elements, offering a great flexibility over standardized, fixed flux path networks have been described. This is then followed by one of the vital aspects of the electromagnetic simulations, i.e boundary conditions, have been addressed and discussed. After that, definition of target geometry in terms of material matrices are established. With this step, it is not only enabled to have a simple definition of virtually any geometry but also the movement or rotation.

Magnetic field excitations occuring due to current carrying conductors and permanent magnets are set up using a unique loop definition systematic. Later, solution technique of the MEC is described based on Newton-Raphson method. All the matrix assemblies and matrix operations used to solve for magnetic field distribution are presented in detail. Moreover, maximum available periodicity, even and odd periodic conditions, are mentioned and their applications are given. Calculation of electromagnetic quantities such as flux linkage and torque are derived based on the flux densities. After a brief discussion on implementation of the model solution is overviewed.

MEC is then used for analyzing three different synchronous machine types. A surface permanent magnet, a synchronous reluctance and a permanent magnet assisted synchronous reluctance machine have been analyzed first in a single operating point where performances and computation times are compared to those obtained

via finite element analysis. In order to further study the capabilities of the MEC, these analysis are extended into dq current plane where a number of grid points are analyzed. The importance of these is twofold, one is to verify performance of the MEC in different saturation conditions and the other is to cover almost all points in a torque-speed plane. Comparison of the results against FEA are done and discussions are provided to elaborate on the discrepancies. It is found out that apart from the torque ripple, flux-linkages and torque are well predicted in a fraction of computation time compared to FEA. Furthermore, a small scale sensitivity analysis is conducted to identify effect of discretization in different parts of the geometry.

Finally, an off-the-shelf synchronous reluctance motor is tested. These test results aimed to obtain magnetic properties of the motor with respect to current. Same points that are used to conduct the tests are also used in FEA and MEC, and all results are compared. According to the results, it is safe to say that, MEC was able predict a performance well enough both against FEA and experimental identification.

4.6.1 Possible Future Work and Improvements

Although good results are obtained with the implemented MEC, there are some aspects that can be improved in the future. These can be summarized as below:

1. Overall code performance can be increased to achieve even less computation time. This includes well organized structure but can be extended to include nonlinear iteration as well. Specifically, other methods of nonlinear iteration can be used and assessed against Newton-Raphson method.

2. Discretization and quality assesment of the discretization can be achieved using a more automotized procedure. This would enable unsupervised geometry definition to be used in even broader range of machine topologies and geometries.

3. Discretization of the geometry can be made to focus on specific areas by disturbing the uniform structure of CE distribution. This way for example, a better resolution in the airgap can be achieved by not over increasing the

number of total CEs which would be the case in a uniform mesh of CEs. Possibly, better torqe ripple and even close match of other quantities can be achieved.

Chapter 5

Conclusion

In this final chapter, a brief summary is given and the main contributions of the work is discussed.

5.1 Conclusive Summary

In this work general design aspects of SynRel machines are investigated. It is known that design of electric machines are actually high-level optimization problems which include non-linearity caused by the materials and performance requirements that often contradicts with each other. Nonetheless, recent advancements in electric drives and wide-spread use of electric machines leads to more and challenging performance requirements.

In the beginning, SynRel machine design is inspected through a state-of-the-art geometry for its rotor. Automatizing the whole analysis procedure numerous optimizations are performed. The effect of objectives and constraints during the design stage are identified. After that a new flux barrier profile is suggested based on the existing fluid shape barriers and splines. With this new barrier shape it is possible to expand the geometric limits of the classical barrier shape which can lead to possible improvements. Both barrier structures are optimized and compared for the same targets where improvements in terms of electromagnetic performances such as average torque, power factor and iron losses are obtained through better utilization of design space. In the following, PM assistance is considered as it is one of the ways to enhance characteristics of a SynRel machine. First the introduction of PMs to the existing SynRel geometry is shown than a PMaSynRel motor is designed

by means of multi-objective optimization. One of the designs is then selected and a prototype machine is manufactured. Tests are conducted over a range of operation points and compared with analysis results.

In the second technical chapter, design of SynRel machine using TO is examined. One of the mostly used methods, DM, is used to design rotor of a SynRel motor. Unlike the geometrical optimization where the optimization variables are geometric parameters, in DM based TO they are the material properties of cell elements. Therefore only parameters that has an effect on the optimization are identified as specific optimization settings of DM. All of these settings, namely discretization, initial density, penalization factor and objective functions are deeply examined. It is found that these have varying effects with respect to the target problem. Some key observations are as follows:

- Design space discretization is important as it defines the resolution of the model. The aim for the mesh has to be good enough so that TO is not limited but on the other hand it has to have limited number of elements in order not to increase computation time. For the focus of SynRel rotor, a medium mesh provided good results where in the case of detailed mesh scenarios only a slight improvement is achieved.

- Effect of initial material properties of the design space and material interpolation are connected together as the penalizaton coefficient alters the density values. Based on the results, best cases are obtained when n=1 and 2. This corresponds to the fact that resultant material interpolation should not be too steep or too flat. For the initial density it is seen that starting close to 0.5 generally produced good results.

- One of the most important settings is reveled to be inclusion of torque ripple objective as in this case, structures similar to the conventional reluctance machines are obtained.

- Applying TO to an already optimized rotor produced some slightly better results which shows that improvement is always possible.

The fourth chapter is dedicated to the implementation of a fast and accurate analysis tool. For this purpose, a generic MEC able to analyze different

machine topologies without the need for changing the reluctance locations or any underlying equations are built. Its building steps are comprehensively explained to show how geometry can be defined and non-linearity can be included. Once it is implemented it has been used to analyze a SynRel, an SPM and a PMaSynRel machine over a wide range of saturation conditions. Comparison against FEM yielded very good characteristics not only in terms of performance but also the computation time. Investigated cases showed that MEC can be 12 to 20 times faster than FEM with negligible mismatch. To also compare it with a real case, an off-the-shelf SynRel machine is tested and good accuracy is obtained.

5.2 Main Contributions

Main contributions of the work can be summarized with respect to each technical chapter as below:

- Chapter 2: Synchronous Reluctance Machines Design and Parametrization of Machine Geometry
  - Most important contribution of this chapter is the proposed novel flux barrier shape. With the aim of expanding geometric limits compared to a conventional shape, better characteristics are obtained which would not possible to achieve with existing barrier profile.
- Chapter 3: Topology Optimization for Synchronous Reluctance Machine Design
  - For this chapter the contribution is mostly for identification and future work for applying TO for a design method. To achieve this, the method is analyzed through its settings and to reveal possible design cases.
  - Another key point is the possible usage of TO for an already optimized design. Considering the time requirement with TO is quite low compared to a conventional optimization using it at the final design stage can be insightfull.
- Chapter 4: Magnetic Equivalent Circuit Modelling

- With the MEC, the novelty is the exploitation of the full periodicity conditions while considering non-linearity and doing this in a generic way so that without changing any formulation it can be used for different geometries.
- Another contribution is that, accuracy and speed of the MEC is proved to be very good when different machine topologies and saturation conditions are considered.
- Although not directly used in the context of this thesis, possible use of this tool in the early design stage or as an assisting tool to FEM by our research group or external parties would be a benefit, therefore this can count as a yet to become accomplishment.

Bibliography

[1] J. K. Kostko, "Polyphase reaction synchronous motors," *Journal of the American Institute of Electrical Engineers*, vol. 42, no. 11, pp. 1162–1168, 1923. DOI: 10.1109/JoAIEE.1923.6591529.

[2] J. F. H. Douglas, "The theory of anisotropic field structures in synchronous machines [includes discussion]," *Transactions of the American Institute of Electrical Engineers. Part III: Power Apparatus and Systems*, vol. 75, no. 3, pp. 84–86, 1956. DOI: 10.1109/AIEEPAS.1956.4499275.

[3] A. Anderson, "Axially laminated anisotropic rotors for reluctance motors," English, *Proceedings of the Institution of Electrical Engineers*, vol. 113, 2058–2060(2), 12 Dec. 1966, ISSN: 0020-3270. [Online]. Available: https://digital-library.theiet.org/content/journals/10.1049/piee.1966.0358.

[4] V. B. Honsinger, "The inductances ld and lq of reluctance machines," *IEEE Transactions on Power Apparatus and Systems*, vol. PAS-90, no. 1, pp. 298–304, 1971. DOI: 10.1109/TPAS.1971.293005.

[5] D. Staton, T. Miller, and S. Wood, "Optimisation of the synchronous reluctance motor geometry," in *1991 Fifth International Conference on Electrical Machines and Drives (Conf. Publ. No. 341)*, 1991, pp. 156–160.

[6] A. Vagati, G. Franceschini, I. Marongiu, and G. Troglia, "Design criteria of high performance synchronous reluctance motors," in *Conference Record of the 1992 IEEE Industry Applications Society Annual Meeting*, 1992, 66–73 vol.1. DOI: 10.1109/IAS.1992.244463.

[7] T. Matsuo and T. Lipo, "Rotor design optimization of synchronous reluctance machine," *IEEE Transactions on Energy Conversion*, vol. 9, no. 2, pp. 359–365, 1994. DOI: 10.1109/60.300136.

[8] A. Vagati, M. Pastorelli, G. Francheschini, and S. Petrache, "Design of low-torque-ripple synchronous reluctance motors," *IEEE Transactions on Industry Applications*, vol. 34, no. 4, pp. 758–765, 1998. DOI: 10.1109/28.703969.

[9] M. Kamper, F. Van der Merwe, and S. Williamson, "Direct finite element design optimisation of the cageless reluctance synchronous machine," *IEEE Transactions on Energy Conversion*, vol. 11, no. 3, pp. 547–555, 1996. DOI: 10.1109/60.537006.

[10] J. H. Lee, J. C. Kim, and D. S. Hyun, "Effect analysis of magnet on ld and lq inductance of permanent magnet assisted synchronous reluctance motor using finite element method," *IEEE Transactions on Magnetics*, vol. 35, no. 3, pp. 1199–1202, 1999. DOI: 10.1109/20.767164.

[11] S. Morimoto, M. Sanada, and Y. Takeda, "Performance of pm-assisted synchronous reluctance motor for high-efficiency and wide constant-power operation," *IEEE Transactions on Industry Applications*, vol. 37, no. 5, pp. 1234–1240, 2001. DOI: 10.1109/28.952497.

[12] P. Niazi, H. Toliyat, D.-H. Cheong, and J.-C. Kim, "A low-cost and efficient permanent magnet assisted synchronous reluctance motor drive," in *IEEE International Conference on Electric Machines and Drives, 2005.*, 2005, pp. 659–666. DOI: 10.1109/IEMDC.2005.195794.

[13] N. Bianchi, S. Bolognani, D. Bon, and M. D. Pre, "Rotor flux-barrier design for torque ripple reduction in synchronous reluctance motors," in *Conference Record of the 2006 IEEE Industry Applications Conference Forty-First IAS Annual Meeting*, vol. 3, 2006, pp. 1193–1200. DOI: 10.1109/IAS.2006.256683.

[14] R. Rajabi Moghaddam, "Synchronous reluctance machine (synrm) in variable speed drives (vsd) applications," QC 20110518, Ph.D. dissertation, KTH, Electrical Machines and Power Electronics, 2011, pp. xviii, 260, ISBN: 978-91-7415-972-1.

[15] G. Pellegrino, F. Cupertino, and C. Gerada, "Barriers shapes and minimum set of rotor parameters in the automated design of synchronous reluctance machines," in *2013 International Electric Machines Drives Conference*, 2013, pp. 1204–1210. DOI: 10.1109/IEMDC.2013.6556286.

[16] F. Cupertino, G. Pellegrino, and C. Gerada, "Design of synchronous reluctance motors with multiobjective optimization algorithms," *IEEE Transactions on Industry Applications*, vol. 50, no. 6, pp. 3617–3627, 2014. DOI: 10.1109/TIA.2014.2312540.

[17] M. Degano, E. Carraro, and N. Bianchi, "Selection criteria and robust optimization of a traction pm-assisted synchronous reluctance motor," *IEEE Transactions on Industry Applications*, vol. 51, no. 6, pp. 4383–4391, 2015. DOI: 10.1109/TIA.2015.2443091.

[18] M. Di Nardo, M. Degano, M. Galea, *et al.*, "End barrier shape optimizations and sensitivity analysis of synchrnous reluctance machines," in *IECON 2015 - 41st Annual Conference of the IEEE Industrial Electronics Society*, 2015, pp. 002 914–002 919. DOI: 10.1109/IECON.2015.7392545.

[19] G. Pellegrino, F. Cupertino, and C. Gerada, "Automatic design of synchronous reluctance motors focusing on barrier shape optimization," *IEEE Transactions on Industry Applications*, vol. 51, no. 2, pp. 1465–1474, 2015. DOI: 10.1109/TIA.2014.2345953.

[20] M. D. Nardo, G. L. Calzo, M. Galea, and C. Gerada, "Design optimization of a high-speed synchronous reluctance machine," *IEEE Transactions on Industry Applications*, vol. 54, no. 1, pp. 233–243, 2018. DOI: 10.1109/TIA.2017.2758759.

[21] R.-R. Moghaddam and F. Gyllensten, "Novel high-performance synrm design method: An easy approach for a complicated rotor topology," *IEEE Transactions on Industrial Electronics*, vol. 61, no. 9, pp. 5058–5065, 2014. DOI: 10.1109/TIE.2013.2271601.

[22] M. Gamba, G. Pellegrino, and F. Cupertino, "Optimal number of rotor parameters for the automatic design of synchronous reluctance machines," in *2014 International Conference on Electrical Machines (ICEM)*, 2014, pp. 1334–1340. DOI: 10.1109/ICELMACH.2014.6960355.

[23] G. Pellegrino and F. Cupertino, "Fea-based multi-objective optimization of ipm motor design including rotor losses," in *2010 IEEE Energy Conversion Congress and Exposition*, 2010, pp. 3659–3666. DOI: 10.1109/ECCE.2010.5618310.

[24] M. Degano, M. Murataliyev, W. Shuo, *et al.*, "Optimised design of permanent magnet assisted synchronous reluctance machines for household appliances," *IEEE Transactions on Energy Conversion*, vol. 36, no. 4, pp. 3084–3095, 2021. DOI: 10.1109/TEC.2021.3076675.

[25] P. Alotto, M. Barcaro, N. Bianchi, and M. Guarnieri, "Optimization of interior pm motors with machaon rotor flux barriers," *IEEE Transactions on Magnetics*, vol. 47, no. 5, pp. 958–961, 2011. DOI: 10.1109/TMAG.2010.2073450.

[26] E. Howard, M. J. Kamper, and S. Gerber, "Asymmetric flux barrier and skew design optimization of reluctance synchronous machines," *IEEE Transactions on Industry Applications*, vol. 51, no. 5, pp. 3751–3760, 2015. DOI: 10.1109/TIA.2015.2429649.

[27] C. Liu, K. Wang, S. Wang, Y. Wang, and J. Zhu, "Torque ripple reduction of synchronous reluctance machine by using asymmetrical barriers and hybrid magnetic core," *CES Transactions on Electrical Machines and Systems*, vol. 5, no. 1, pp. 13–20, 2021. DOI: 10.30941/CESTEMS.2021.00003.

[28] R. M. R. Kumar, G. Vakil, D. Gerada, *et al.*, "Enhancing the torque density of conventional pm-synrel machine with hybrid flux barrier," in *IECON 2019 - 45th Annual Conference of the IEEE Industrial Electronics Society*, vol. 1, 2019, pp. 4347–4352. DOI: 10.1109/IECON.2019.8926624.

[29] M. Barcaro, G. Meneghetti, and N. Bianchi, "Structural analysis of the interior pm rotor considering both static and fatigue loading," *IEEE Transactions on Industry Applications*, vol. 50, no. 1, pp. 253–260, 2014. DOI: 10.1109/TIA.2013.2268048.

[30] G. Gallicchio, M. D. Nardo, M. Palmieri, *et al.*, "High speed permanent magnet assisted synchronous reluctance machines – part i: A general design approach," *IEEE Transactions on Energy Conversion*, vol. 37, no. 4, pp. 2556–2566, 2022. DOI: 10.1109/TEC.2022.3176382.

[31] A. Fratta, G. Troglia, A. Vagati, and F. Villata, "Evaluation of torque ripple in high performance synchronous reluctance machines," in *Conference Record of the 1993 IEEE Industry Applications Conference Twenty-Eighth IAS Annual Meeting*, 1993, 163–170 vol.1. DOI: 10.1109/IAS.1993.298919.

[32] Z. Zhu and D. Howe, "Influence of design parameters on cogging torque in permanent magnet machines," *IEEE Transactions on Energy Conversion*, vol. 15, no. 4, pp. 407–412, 2000. DOI: 10.1109/60.900501.

[33] X. Bomela and M. Kamper, "Effect of stator chording and rotor skewing on performance of reluctance synchronous machine," *IEEE Transactions on Industry Applications*, vol. 38, no. 1, pp. 91–100, 2002. DOI: 10.1109/28.980362.

[34] P. Lazari, J. Wang, and B. Sen, "3-d effects of rotor step-skews in permanent magnet-assisted synchronous reluctance machines," *IEEE Transactions on Magnetics*, vol. 51, no. 11, pp. 1–4, 2015. DOI: 10.1109/TMAG.2015.2446511.

[35] A. Galassini, G. Lo Calzo, A. Formentini, C. Gerada, P. Zanchetta, and A. Costabeber, "Ucube: Control platform for power electronics," in *2017 IEEE Workshop on Electrical Machines Design, Control and Diagnosis (WEMDCD)*, 2017, pp. 216–221. DOI: 10.1109/WEMDCD.2017.7947749.

[36] D. Staton, T. Miller, and S. Wood, "Maximising the saliency ratio of the synchronous reluctance motor," *Electric Power Applications, IEE Proceedings B*, vol. 140, no. 4, pp. 249–259, Jul. 1993, ISSN: 0143-7038. DOI: 10.1049/ip-b.1993.0031.

[37] T. Lipo, A. Vagati, I. A. Society, and I. A. S. I. D. Committee, *Synchronous Reluctance Motors and Drives: A New Alternative ; Presented Oct. 2, 1994 at the IAS Annual Meeting, Denver CO* (Tutorial course). Inst. of Electrical and Electronics Engineers, 1994. [Online]. Available: https://books.google.it/books?id=KlfyPgAACAAJ.

[38] R. R. Moghaddam, F. Magnussen, and C. Sadarangani, "Theoretical and experimental reevaluation of synchronous reluctance machine," *Industrial Electronics, IEEE Transactions on*, vol. 57, no. 1, pp. 6–13, 2010.

[39] M. P. Bendsøe and N. Kikuchi, "Generating optimal topologies in structural design using a homogenization method," *Computer Methods in Applied Mechanics and Engineering*, vol. 71, no. 2, pp. 197–224, 1988, ISSN: 0045-7825. DOI: https://doi.org/10.1016/0045-7825(88)90086-2. [Online]. Available: https://www.sciencedirect.com/science/article/pii/0045782588900862.

[40] D. Dyck and D. Lowther, "Automated design of magnetic devices by optimizing material distribution," *IEEE Transactions on Magnetics*, vol. 32, no. 3, pp. 1188–1193, 1996. DOI: 10.1109/20.497456.

[41] I. Hahn, "Heuristic structural optimization of the permanent magnets used in a surface mounted permanent-magnet synchronous machine," *IEEE Transactions on Magnetics*, vol. 48, no. 1, pp. 118–127, 2012. DOI: 10.1109/TMAG.2011.2167980.

[42] T.-H. Lee, J.-H. Lee, K.-P. Yi, and D.-K. Lim, "Optimal design of a synchronous reluctance motor using a genetic topology algorithm," *Processes*, vol. 9, no. 10, 2021, ISSN: 2227-9717. DOI: 10.3390/pr9101778. [Online]. Available: https://www.mdpi.com/2227-9717/9/10/1778.

[43] T. Sato, K. Watanabe, and H. Igarashi, "Multimaterial topology optimization of electric machines based on normalized gaussian network," *IEEE Transactions on Magnetics*, vol. 51, no. 3, pp. 1–4, 2015. DOI: 10.1109/TMAG.2014.2359972.

[44] H. Sasaki and H. Igarashi, "Topology optimization using basis functions for improvement of rotating machine performances," *IEEE Transactions on Magnetics*, vol. 54, no. 3, pp. 1–4, 2018. DOI: 10.1109/TMAG.2017.2759784.

[45] I. Lolova, J. Barta, G. Bramerdorfer, and S. Silber, "Topology optimization of line-start synchronous reluctance machine," in *2020 19th International Conference on Mechatronics - Mechatronika (ME)*, 2020, pp. 1–7. DOI: 10.1109/ME49197.2020.9286643.

[46] J. Barta, L. Knebl, G. Bramerdorfer, I. Lolova, S. Silber, and O. Vitek, "Topology optimization of rotor bars geometry and arrangement for a line-start permanent magnet synchronous machine," *IEEE Access*, vol. 9, pp. 115 192–115 204, 2021. DOI: 10.1109/ACCESS.2021.3104642.

[47] G. Allaire, "A review of adjoint methods for sensitivity analysis, uncertainty quantification and optimization in numerical codes," *Ingénieurs de l'Automobile*, vol. 836, pp. 33–36, Jul. 2015. [Online]. Available: https://hal.archives-ouvertes.fr/hal-01242950.

[48] S. Wang, S. Park, and J. Kang, "Multi-domain topology optimization of electromagnetic systems," *COMPEL - The international journal for computation and mathematics in electrical and electronic engineering*, vol. 23, no. 4, pp. 1036–1044, 2004. DOI: https://doi.org/10.1108/03321640410553463. [Online]. Available: https://www.emerald.com/insight/content/doi/10.1108/03321640410553463/full/html.

[49] J. Lee and N. Seo J.H. Kikuchi, "Optimal design of an electromagnetic coupler to maximize force to a specific direction," *IEEE Transactions on Magnetics*, vol. 44, no. 7, pp. 1737–1742, 2008. DOI: 10.1109/TMAG.2008.922183.

[50] B. S. B. Mohamodhosen, "Topology optimisation of electromagnetic devices," Ph.D. dissertation, Ecole Centrale de Lille, 2017.

[51] Y. Okamoto and N. Takahashi, "Investigation of topology optimization of magnetic circuit using density method," *Electrical Engineering in Japan*, vol. 155, no. 2, pp. 53–63, 2006. DOI: https://doi.org/10.1002/eej.20259.

[52] J. Lee, J. H. Seo, and N. Kikuchi, "Topology optimization of switched reluctance motors for the desired torque profile," *Structural and Multidisciplinary Optimization*, vol. 42, no. 5, pp. 783–796, 2010. DOI: 10.1007/s00158-010-0547-1.

[53] C. Lee and I. G. Jang, "Topology optimization of multiple-barrier synchronous reluctance motors with initial random hollow circles," *Structural and Multidisciplinary Optimization*, vol. 64, no. 4, pp. 1–12, 2021. DOI: 10.1007/s00158-021-02976-2.

[54] F. Guo, M. Salameh, M. Krishnamurthy, and I. P. Brown, "Multimaterial magneto-structural topology optimization of wound field synchronous machine rotors," *IEEE Transactions on Industry Applications*, vol. 56, no. 4, pp. 3656–3667, 2020. DOI: 10.1109/TIA.2020.2989682.

[55] F. Guo and I. P. Brown, "Simultaneous magnetic and structural topology optimization of synchronous reluctance machine rotors," *IEEE Transactions on Magnetics*, vol. 56, no. 10, pp. 1–12, 2020. DOI: 10.1109/TMAG.2020.3014289.

[56] J. S. Choi and J. Yoo, "Structural optimization of ferromagnetic materials based on the magnetic reluctivity for magnetic field problems," *Computer Methods in Applied Mechanics and Engineering*, vol. 197, no. 49, pp. 4193–4206, 2008, ISSN: 0045-7825. DOI: https://doi.org/10.1016/j.cma.2008.04.019. [Online]. Available: https://www.sciencedirect.com/science/article/pii/S0045782508001771.

[57] E. Lwithwaite, "Magnetic equivalent circuits for electrical machines," English, *Proceedings of the Institution of Electrical Engineers*, vol. 114, 1805–1809(4), 11 Nov. 1967, ISSN: 0020-3270. [Online]. Available: https://digital-library.theiet.org/content/journals/10.1049/piee.1967.0344.

[58] C. Carpenter, "Magnetic equivalent circuits," English, *Proceedings of the Institution of Electrical Engineers*, vol. 115, 1503–1511(8), 10 Sep. 1968, ISSN: 0020-3270. [Online]. Available: https://digital-library.theiet.org/content/journals/10.1049/piee.1968.0265.

[59] G. Slemon, "Equivalent circuits for transformers and machines including non-linear effects," English, *Proceedings of the IEE - Part IV: Institution Monographs*, vol. 100, 129–143(14), 5 Sep. 1953, ISSN: 0369-8912. [Online]. Available: https://digital-library.theiet.org/content/journals/10.1049/pi-4.1953.0015.

[60] V. Ostovic, "A method for evaluation of transient and steady state performance in saturated squirrel cage induction machines," *IEEE Transactions on Energy Conversion*, vol. EC-1, no. 3, pp. 190–197, 1986. DOI: 10.1109/TEC.1986.4765754.

[61] V. Ostovic, "A simplified approach to magnetic equivalent-circuit modeling of induction machines," *IEEE Transactions on Industry Applications*, vol. 24, no. 2, pp. 308–316, 1988. DOI: 10.1109/28.2871.

[62] G. Slemon, "An equivalent circuit approach to analysis of synchronous machines with saliency and saturation," *IEEE Transactions on Energy Conversion*, vol. 5, no. 3, pp. 538–545, 1990. DOI: 10.1109/60.105279.

[63] M. Jenkins, D. Howe, and T. Birch, "An improved design procedure for hybrid stepper motors," *IEEE Transactions on Magnetics*, vol. 26, no. 5, pp. 2535–2537, 1990. DOI: 10.1109/20.104789.

[64] J. Hur, S.-B. Yoon, D.-Y. Hwang, and D.-S. Hyun, "Analysis of pmlsm using three dimensional equivalent magnetic circuit network method," *IEEE Transactions on Magnetics*, vol. 33, no. 5, pp. 4143–4145, 1997. DOI: 10.1109/20.619690.

[65] C. Rasmussen and E. Ritchie, "A magnetic equivalent circuit approach for predicting pm motor performance," in *IAS '97. Conference Record of the 1997 IEEE Industry Applications Conference Thirty-Second IAS Annual Meeting*, vol. 1, 1997, 10–17 vol.1. DOI: 10.1109/IAS.1997.643001.

[66] M. Moallem and G. Dawson, "An improved magnetic equivalent circuit method for predicting the characteristics of highly saturated electromagnetic devices," *IEEE Transactions on Magnetics*, vol. 34, no. 5, pp. 3632–3635, 1998. DOI: 10.1109/20.717858.

[67] E. Lovelace, T. Jahns, and J. Lang, "A saturating lumped-parameter model for an interior pm synchronous machine," *IEEE Transactions on Industry Applications*, vol. 38, no. 3, pp. 645–650, 2002. DOI: 10.1109/TIA.2002.1003413.

[68] Y.-D. Chun, J. Lee, and S. Wakao, "Overhang effect analysis of brushless dc motor by 3-d equivalent magnetic circuit network method," *IEEE Transactions on Magnetics*, vol. 39, no. 3, pp. 1610–1613, 2003. DOI: 10.1109/TMAG.2003.810179.

[69] Y. Chun, S. Wakao, T. Kim, K. Jang, and J. Lee, "Multiobjective design optimization of brushless permanent magnet motor using 3d equivalent magnetic circuit network method," *IEEE Transactions on Applied Superconductivity*, vol. 14, no. 2, pp. 1910–1913, 2004. DOI: 10.1109/TASC.2004.830928.

[70] Y. Kano, T. Kosaka, and N. Matsui, "Simple nonlinear magnetic analysis for interior permanent magnet synchronous motors," in *Second International Conference on Power Electronics, Machines and Drives (PEMD 2004).*, vol. 2, 2004, 781–786 Vol.2. DOI: 10.1049/cp:20040388.

[71] Y. Kano, T. Kosaka, and N. Matsui, "Simple nonlinear magnetic analysis for permanent-magnet motors," *IEEE Transactions on Industry Applications*, vol. 41, no. 5, pp. 1205–1214, 2005. DOI: 10.1109/TIA.2005.853376.

[72] Z. Zhu, Y. Pang, D. Howe, S. Iwasaki, R. Deodhar, and A. Pride, "Analysis of electromagnetic performance of flux-switching permanent-magnet machines by nonlinear adaptive lumped parameter magnetic circuit model," *IEEE Transactions on Magnetics*, vol. 41, no. 11, pp. 4277–4287, 2005. DOI: 10.1109/TMAG.2005.854441.

[73] S. Vaez-Zadeh and A. H. Isfahani, "Enhanced modeling of linear permanent-magnet synchronous motors," *IEEE Transactions on Magnetics*, vol. 43, no. 1, pp. 33–39, 2007. DOI: 10.1109/TMAG.2006.886970.

[74] S. D. Sudhoff, B. T. Kuhn, K. A. Corzine, and B. T. Branecky, "Magnetic equivalent circuit modeling of induction motors," *IEEE Transactions on Energy Conversion*, vol. 22, no. 2, pp. 259–270, 2007. DOI: 10.1109/TEC.2006.875471.

[75] Y. Kano, K. Tonogi, T. Kosaka, and N. Matsui, "Optimization of axial-flux pm machines for improved torque density by simple non-linear magnetic analysis," in *2007 IEEE International Electric Machines Drives Conference*, vol. 1, 2007, pp. 27–33. DOI: 10.1109/IEMDC.2007.383547.

[76] S.-H. Han, T. M. Jahns, and W. L. Soong, "A magnetic circuit model for an ipm synchronous machine incorporating moving airgap and cross-coupled saturation effects," in *2007 IEEE International Electric Machines & Drives Conference*, vol. 1, 2007, pp. 21–26. DOI: 10.1109/IEMDC.2007.383546.

[77] C. Bruzzese, D. Zito, and A. Tessarolo, "Finite reluctance approach: A systematic method for the construction of magnetic network-based dynamic models of electrical machines," in *2014 AEIT Annual Conference - From Research to Industry: The Need for a More Effective Technology Transfer (AEIT)*, 2014, pp. 1–6. DOI: 10.1109/AEIT.2014.7002054.

[78] A. Hemeida, A. Lehikoinen, P. Rasilo, *et al.*, "A simple and efficient quasi-3d magnetic equivalent circuit for surface axial flux permanent magnet synchronous machines," *IEEE Transactions on Industrial Electronics*, vol. 66, no. 11, pp. 8318–8333, 2019. DOI: 10.1109/TIE.2018.2884212.

[79] S. Yang, Y. Amara, W. Hua, and G. Barakat, "Development of a generic framework for lumped parameter modeling," *Open Physics*, vol. 18, no. 1, pp. 365–373, 2020. DOI: doi:10.1515/phys-2020-0168. [Online]. Available: https://doi.org/10.1515/phys-2020-0168.

[80] G. Watthewaduge, E. Sayed, A. Emadi, and B. Bilgin, "Reluctance mesh-based modeling of switched reluctance machines," in *2021 IEEE Transportation Electrification Conference Expo (ITEC)*, 2021, pp. 407–412. DOI: 10.1109/ITEC51675.2021.9490134.

[81] G. Watthewaduge and B. Bilgin, "Radial force density calculation of switched reluctance machines using reluctance mesh-based magnetic equivalent circuit," *IEEE Open Journal of the Industrial Electronics Society*, vol. 3, pp. 37–49, 2022. DOI: 10.1109/OJIES.2021.3138610.

[82] A. M. Silva, C. H. Antunes, A. M. S. Mendes, and F. J. T. E. Ferreira, "Generalized reluctance network framework for fast electromagnetic analysis of radial-flux machines," *IEEE Transactions on Energy Conversion*, vol. 38, no. 1, pp. 310–320, 2023. DOI: 10.1109/TEC.2022.3206897.

[83] H. W. Derbas, J. M. Williams, A. C. Koenig, and S. D. Pekarek, "A comparison of nodal- and mesh-based magnetic equivalent circuit models," *IEEE Transactions on Energy Conversion*, vol. 24, no. 2, pp. 388–396, 2009. DOI: 10.1109/TEC.2008.2002037.

[84] "Permanent magnet machines," in *Introduction to AC Machine Design*. John Wiley & Sons, Ltd, 2017, ch. 8, pp. 359–400, ISBN: 9781119352181. DOI: https://doi.org/10.1002/9781119352181.ch8. eprint: https://onlinelibrary.wiley.com/doi/pdf/10.1002/9781119352181.ch8. [Online]. Available: https://onlinelibrary.wiley.com/doi/abs/10.1002/9781119352181.ch8.

[85] M. Popescu, "Prediction of the electromagnetic torque in synchronous machines through maxwell stress harmonic filter (hft) method," *Electrical Engineering*, vol. 89, pp. 1162–1168, 2006. DOI: 10.1007/s00202-005-0323-1.

[86] E. Armando, R. I. Bojoi, P. Guglielmi, G. Pellegrino, and M. Pastorelli, "Experimental identification of the magnetic model of synchronous machines," *IEEE Transactions on Industry Applications*, vol. 49, no. 5, pp. 2116–2125, 2013. DOI: 10.1109/TIA.2013.2258876.